AD_____

Award Number: DAMD17-98-1-8147

TITLE: Breast Cancer Screening Using Photonic Technology

PRINCIPAL INVESTIGATOR: Robert R. Alfano, Ph.D.

CONTRACTING ORGANIZATION: The City University of New York
New York, New York 10031-9198

REPORT DATE: September 2001

TYPE OF REPORT: Annual

PREPARED FOR: U.S. Army Medical Research and Materiel Command
Fort Detrick, Maryland 21702-5012

DISTRIBUTION STATEMENT: Approved for Public Release;
Distribution Unlimited

The views, opinions and/or findings contained in this report are those of the author(s) and should not be construed as an official Department of the Army position, policy or decision unless so designated by other documentation.

20020306 095

Copies Furnished to DTIC
Reproduced From
Bound Original

REPORT DOCUMENTATION PAGE

Form Approved
OMB No. 074-0188

Public reporting burden for this collection of information is estimated to average 1 hour per response, including the time for reviewing instructions, searching existing data sources, gathering and maintaining the data needed, and completing and reviewing this collection of information. Send comments regarding this burden estimate or any other aspect of this collection of information, including suggestions for reducing this burden to Washington Headquarters Services, Directorate for Information Operations and Reports, 1215 Jefferson Davis Highway, Suite 1204, Arlington, VA 22202-4302, and to the Office of Management and Budget, Paperwork Reduction Project (0704-0188), Washington, DC 20503

1. AGENCY USE ONLY (Leave blank)	2. REPORT DATE	3. REPORT TYPE AND DATES COVERED
	September 2001	Annual (15 Aug 00 - 14 Aug 01)

4. TITLE AND SUBTITLE
Breast Cancer Screening Using Photonic Technology

5. FUNDING NUMBERS
DAMD17-98-1-8147

6. AUTHOR(S)
Robert R. Alfano, Ph.D.

7. PERFORMING ORGANIZATION NAME(S) AND ADDRESS(ES)

The City University of New York
New York, New York 10031-9198

E-Mail: **alfano@scisun.sci.ccny.cuny.edu**

8. PERFORMING ORGANIZATION REPORT NUMBER

9. SPONSORING / MONITORING AGENCY NAME(S) AND ADDRESS(ES)

U.S. Army Medical Research and Materiel Command
Fort Detrick, Maryland 21702-5012

10. SPONSORING / MONITORING AGENCY REPORT NUMBER

11. SUPPLEMENTARY NOTES
Report contains color

12a. DISTRIBUTION / AVAILABILITY STATEMENT
Approved for Public Release; Distribution Unlimited

12b. DISTRIBUTION CODE

13. ABSTRACT *(Maximum 200 Words)*

The research carried out during the current reporting period involved: (a) time-sliced and spectroscopic two-dimensional (2-D) near-infrared transillumination imaging of normal and cancerous *in vitro* human breast tissue specimens; (b) correlating the results of optical measurements with NMR measurements; (c) derivation of analytical solutions of the polarized photon transport equation that provides a more accurate analytical basis for developing three-dimensional (3-*D*) inverse image reconstruction techniques; and (d) development of forward models and 3-D inverse image reconstruction methods. Images recorded with earlier temporal slices of transmitted light were found to highlight cancerous tissues while those recorded with later slices accentuated normal fibrous tissues. Initial spectroscopic imaging experiments show that the ratio, *R* of light intensity transmitted through the cancerous tissue to that through the corresponding normal tissue show a wavelength dependent variation that has the potential to be used as a useful parameter for cancer identification. Analytical solutions of the polarized photon transport equation are more complete and enable description of polarized light imaging. Faster and more noise-resistant 3-D image reconstruction schemes are being pursued.

14. SUBJECT TERMS
Breast Cancer, optical mammography, time-resolved imaging, inverse image reconstruction, spectroscopic imaging, transillumination, NMR

15. NUMBER OF PAGES
63

16. PRICE CODE

17. SECURITY CLASSIFICATION OF REPORT	18. SECURITY CLASSIFICATION OF THIS PAGE	19. SECURITY CLASSIFICATION OF ABSTRACT	20. LIMITATION OF ABSTRACT
Unclassified	Unclassified	Unclassified	Unlimited

(3) TABLE OF CONTENTS

		Page
1. Front Cover		**1**
2. SF 298		**2**
3. Table of Contents		**3**
4. Introduction		**4**
5. Body		**4**
5.1 Time-sliced and Spectroscopic *in vitro* Imaging of Human Breast Tissues		**4**
5.2 Correlation with NMR Results		**5**
5.3 Analytical Solution of Photon Transport Equation		**5**
5.4 Development of Inverse Image Reconstruction Methods		**7**
6. Key Research Accomplishments		**7**
7. Reportable Outcomes		**7**
8. Conclusions		**8**
9. References		**8**
10. Appendices		
Appendix 1*	Reprint: "Temporally and spectrally resolved ..."	A1-1
Appendix 2	Reprint: "Analytical solution of the polarized photon ..."	A2-1
Appendix 3	Preprint: "Cumulant approximation of the radiative ..."	A3-1
Appendix 4*	Reprint: "Time-resolved Fourier optical ... tomography"	A4-1

* Preprints were submitted with last Annual Report. As the reprints became available, those are made part of this report.

(4) INTRODUCTION

The "**Breast Cancer Screening Using Photonic Technology**" research project is devoted to developing techniques for obtaining direct two-dimensional (2-*D*), and tomographic three-dimensional (3-*D*) images of cancerous lesions of human breast that make using noninvasive near-infrared (NIR) light. The imaging method involves illuminating the specimen with ultrashort NIR pulses of laser light and construction of images using two approaches. The direct or the **shadowgram** method utilizes the image bearing component of the forward-transmitted light, while the **inverse reconstruction method** makes use of the measured transmitted, forward-scattered or backscattered light intensity profiles, known or estimated optical properties of the sample, a model for light propagation through turbid media and a sophisticated computer algorithm to construct images of the interior structure of the specimen.

Significant advances in developing both of these approaches were made during the current reporting period. Correlating the results with that obtained from available methods assesses efficacy of the methods so developed. We have initiated correlating the results of optical measurements with that obtained from nuclear magnetic resonance (NMR) on the same samples.

(5) BODY

The tasks performed and the progress made during the current reporting period may be broadly grouped as follows:

5.1 Time-sliced and spectroscopic *in vitro* imaging of human breast tissues,
5.2 Correlation with NMR results,
5.3 Analytical solutions of photon transport equation, and
5.4 Development of the inverse image reconstruction method.

We will briefly outline our accomplishments in each of these areas, and refer to appended publications (Appendices 1-4) for detailed description where applicable.

5.1 Time-sliced and Spectroscopic *in vitro* Imaging of Human Breast Tissues

We pursued the time-sliced and spectroscopic direct 2-*D* imaging of *in vitro* normal and cancerous human breast tissues (**TO 5-7, Tasks 12-15**) using the experimental arrangements developed and improved during the earlier reporting periods. The time-sliced imaging arrangement uses ~150 fs, 1 kHz, 800 nm pulses from a Ti:sapphire laser and amplifier system for sample illumination and an ultrafast gated intensified camera system (UGICS) for recording 2-*D* images using different temporal slices of the transmitted light pulse.

We now routinely use UGICS for recording time-sliced images after a comparison (**TO 3, Task 7**) of the UGICS and optical Kerr gate (OKG) revealed that the UGICS is better suited for the task. OKG provides gate width limited by the response time of the Kerr medium or the pulse width and could attain time resolution of a few picoseconds, compared to the ~80 ps gate width provided by the UGICS. The UGICS is easier to operate, does not need the demanding overlap of the gating and signal beams as required in an OKG, and the 80-ps gate-width is reasonable compromise for the present application.

The spectroscopic imaging arrangement uses the 1210-1300 nm output of a modelocked Cr^{4+}:forsterite laser for sample illumination, a Fourier gate for rejecting multiple scattered light, and an InGaAs near-infrared area camera for recording 2-*D* images, as detailed in the two earlier annual reports.

Measurements were extended to more breast tissue specimens with infiltrating ductal carcinoma, and infiltrating lobular carcinoma from patients of different ages. Samples were

obtained from our collaborators at the Memorial Sloan Kettering Cancer Center and National Disease Research Interchange under an IRB approval at the City College of New York.

The results of time-sliced 2-*D* imaging experiments are consistent with our earlier results[1,2] that images recorded with light in the earlier time slices highlight the cancerous tissues, while those obtained with light in the later time slices highlight the normal tissues. Time-sliced imaging can thus separate out normal and cancerous tissues in excised specimens. Some of these results are also presented in *Appendix 1.* A sequence of these 2-*D* images can be used for 3-*D* image reconstruction.

We are pursuing multi-wavelength differential imaging on normal and cancerous breast tissues (**TO 5-7, Task 15**) to verify and build statistics on our observation of wavelength-dependent difference in light transmission through the cancerous and normal tissues that was first reported in the last Annual Report. The pattern repeats in a majority of the samples we investigated. We are working on defining a wavelength-dependent parameter whose values would be indicative of the state of tissue as normal or cancerous.

5.2 Correlation with NMR Results

One of the objectives of the project was to correlate the results of optical measurements with those obtained from other commonly used methods (**TO 5-7, Task 17**), such as, pathology, x-ray, and NMR. We routinely correlate our optical measurements on excised breast tissue samples with pathological evaluation, which is not suitable for *in vivo* measurements. NMR can provide an *in vivo* assessment. So we have initiated measurements on the same excised breast tissue specimens using both optical and NMR techniques to investigate how the results correlate. NMR measurements were carried out at the Memorial Sloan Kettering Cancer Center by our collaborator Dr. Jason Koutcher. Figures 1 (a)-1(f) present a photograph of the sample, a NMR image, time-sliced optical images at delay times of 100 ps, and 300 ps, as well as, corresponding spatial intensity distributions. The 100–ps image highlights the cancerous tissue, which is in good qualitative correlation with the NMR results displayed in Fig. 1(b). We will pursue these measurements further on other samples to obtain quantitative correlation.

5.3 Analytical Solutions of Photon Transport Equation

Development of inverse image reconstruction methods requires a theoretical model that provides an accurate description of photon transport through highly scattering turbid media. We have built on the earlier successes[3,4] of our theoretical endeavor (**TO 4, Task 10; TO 8, task 18**), and extended those in two very important ways. First, we have developed an analytical solution of the polarized photon transport equation in an infinite uniform medium using Cumulant Expansion (*Appendix 2*) that can take into account the vector nature of electromagnetic radiation and can handle the polarization property of light.[5] This is a highly significant advance over our Cumulant Solution of Elastic Scalar Boltzmann Transport Equation in an infinite uniform isotropic medium,[3,4] which in itself was a major advance over the commonly used diffusion approximation that fails to adequately account for ballistic and snake photons.[6]

Second, our Cumulant Solution[3,4] of the scalar equation has been extended to semi-infinite and slab geometries (*Appendix 3*).[7] This extension makes the solution more suited for practical application which always involve finite geometries.

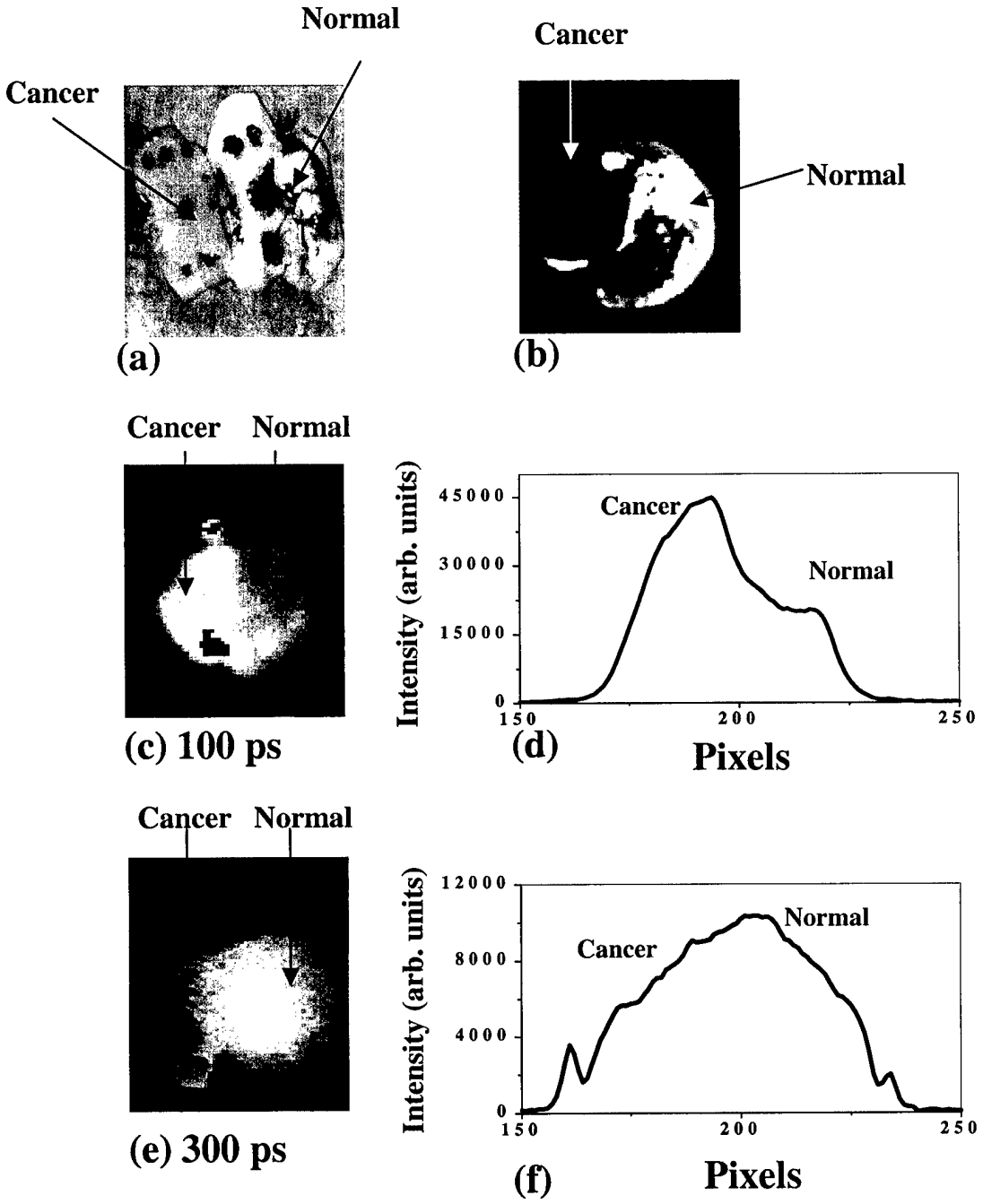

Fig. 1(a) Photograph of the specimen showing the normal fibrous and cancerous (invasive ductal carcinoma) tissues in the specimen. The pink dots represent orientation markings made on the sample for histology following optical and NMR measurements. (b) A T_1 weighted NMR image of the specimen showing the normal and cancerous parts. (c) A time-sliced optical image recorded for a delay time of 100 ps, and the corresponding spatial intensity distribution (d) integrated over the horizontal region denoted by the dashed box. Cancerous region is highlighted in this early-light image. (e) Another time-sliced optical image recorded for a delay time of 300 ps, and the corresponding spatial intensity distribution (f) integrated over the same horizontal region as in (c). Transmitted intensity is higher in the later-light image. The zero time is taken to be the time of arrival of light through the glass cell containing clear water instead of the tissue.

5.4 Development of Inverse Image Reconstruction Methods

We have completed the development of a time-resolved Fourier optical diffuse tomography approach[8] for inverse image reconstruction (**TO 4, Tasks 8, 9; TO 8, Task 18**) that we presented in the last Annual Report and attach here as *Appendix 4*. The approach allows use of both transmitted and backscattered photons from the scattering medium to obtain 3-D images of embedded absorbing and scattering inhomogeneities. It introduces the concept of propagation of spatial Fourier component of the scattered wave field inside the scattering medium, and then develops a new optical diffuse imaging methodology based on that theory. A test run using simulated data was able to reconstruct images of four inhomogeneities located up to 2 cm below the surface of a human tissue-like semi-infinite scattering medium using backscattered photons. We are pursuing testing of this and other methods developed in this project for inverse reconstruction of objects using experimental data. An important issue is a choice of reference medium (**TO 4, Task 10**) and we have used Intralipid suspension of different concentration, and suspension of TiO_2 particles of different size in water. We are also searching for matching reference materials for breast tissue.

We are building forward model and inversion algorithms based on our cumulant solutions of the scalar radiative transport equation. Models using the first two cumulants has been built and tested using simulated data. The model describes long-time behavior well. Higher-order cumulants will be needed to account for early-time behaviors, and is being actively pursued.

(6) KEY RESEARCH ACCOMPLISHMENTS

- Verified earlier inferences that time-sliced 2-*D* transillumination images recorded with earlier temporal slices of transmitted light highlight cancerous tissues while those recorded with later slices accentuated normal fibrous tissues by extending measurements to more breast tissue specimens.
- Initial results show good qualitative correlation between results of time-sliced and NMR imaging methods.
- Carried out spectroscopic imaging experiments on more breast tissue specimens and trying to verify if the ratio *R* of light intensity transmitted through the cancerous tissue to that through the corresponding normal tissue as a function of wavelength could be used as a useful parameter for cancer identification.
- Developed analytical solutions of the polarized photon transport equation that enable description of the polarization properties of light transmitting through a highly-scattering medium.
- Extended Cumulant Solution of scalar transport equation to semi-infinite and slab geometries making it more suited for practical application that involves finite boundaries.
- Developed a forward model and computer algorithm for inverse image reconstruction scheme that can use both forward transmitted and backscattered light to provides fast, noise-resistant 3-D images of scattering and absorptive inhomogeneities at various depths inside a scattering medium.

(7) REPORTABLE OUTCOMES

Articles

1. S. K. Gayen, M. Alrubaiee, M. E. Zevallos and R. R. Alfano, "Temporally and spectrally resolved optical imaging of normal and cancerous human breast tissues," in the *Proceedings*

of the Inter-Institute Workshop on In Vivo Optical Imaging at the NIH, Amir Gandjbakhche, ed. (Optical Society of America, Washington, DC, 2000), pp. 142-147.
2. W. Cai, M. Lax, R. R. Alfano, "Analytical solution of the polarized photon transport equation in an infinite uniform medium using cumulant expansion," Phys. Rev. E **63**, 016606-1(2001).
3. M. Xu, M. Lax, R. R. Alfano, "Time-resolved Fourier optical diffuse tomography," J. Opt. Soc. Am. A **18**, 1535 (2001).
4. A. Carpenter, W. Cai, M. Lax, R. R. Alfano, "Cumulant approximation of the radiative transfer equation for photon density in semi-infinite and slab geometries," J. Opt. Soc. Am. A (submitted).

(8) CONCLUSIONS

The work carried out during this reporting period builds on and affirms some of our earlier inferences and leads to some new conclusions. *First,* time-sliced 2-D transillumination images recorded with earlier temporal slices of transmitted light highlighted cancerous tissues while those recorded with later slices accentuated normal fibrous tissues. *Second,* results of time-sliced measurement are in good agreement with NMR results on same samples. *Third,* wavelength dependence of a ratio, *R* of light intensity transmitted through the cancerous tissue shows the potential to be used as a useful parameter for cancer identification. *Fourth,* analytical solutions of the polarized photon transport equation using Cumulant Expansion that we obtained enables description of polarization characteristics of light emerging from a scattering medium and will be useful for reconstruction of polarization gated images. *Fifth,* the theoretical formalism and computer algorithm for inverse image reconstruction scheme using both forward and backscattered light shows (with simulated data) the potential to provide fast 3-*D* images of scattering and absorbing objects at various depths inside a scattering medium.

We plan to build on these developments and pursue *in vivo* breast imaging on volunteers following testing of the techniques on model breast structures made from excised tissues, and have submitted a proposal to USAMRMC seeking support for the work.

"So What Section"

The implication of the first conclusion is that time-sliced imaging offers the possibility of highlighting cancerous lesions in human breast. The second conclusion points to the complementary nature of optical and NMR imaging, and the possibility of using them together for better specificity. The third conclusion indicates the diagnostic potential of optical imaging based upon multi-spectral measurements. X-ray mammography, most often used method, cannot diagnose cancer. The fourth and fifth conclusions together present the possibility of developing robust 3-*D* inverse image reconstruction formalisms, that in addition to being applicable for optical mammography, will be useful for imaging tumors in other body organs, such as, prostate and thyroid glands, as well as, objects inside other types of scattering media, such as, cloud, fog, smoke, and murky water.

(9) REFERENCES

1. S. K. Gayen, M. Alrubaiee, M. E. Zevallos and R. R. Alfano, "Temporally and spectrally resolved optical imaging of normal and cancerous human breast tissues," in the *Proceedings*

of the Inter-Institute Workshop on In Vivo Optical Imaging at the NIH, Edited by A. Gandjbakhche, Optical Society of America (to be published), p. 142.
2. S. K. Gayen and R. R. Alfano, "Sensing lesions in tissues with light," Opt. Express **4**, 475 (1999).
3. W. Cai, M. Lax, and R. R. Alfano, "Analytical solution of the elastic Boltzmann transport equation in an infinite uniform medium using cumulant expansion," J. Phys. Chem. B **104**, 3996 (2000).
4. W. Cai, M. Lax, and R. R. Alfano, "Cumulant solution of the elastic Boltzmann transport equation in an infinite uniform medium," Phys. Rev. E **61**, 3871 (2000).
5. W. Cai, M. Lax, and R. R. Alfano, "Analytical solution of the polarized photon transport equation in an infinite uniform medium using cumulant expansion," Phys. Rev. E **63**, 016606-1 (2001).
6. S. R. Arridge and J. C. Hebden, "Optical imaging in medicine: II. Modeling and reconstruction," Phys. Med. Biol. **42**, 841 (1997).
7. A. V. Carpenter, W. Cai, M. Lax, and R. R. Alfano, "Cumulant approximation of the radiative transfer equation for photon density in semi-infinite and slab geometries," J. Opt. Soc. Am. A (submitted).
8. M. Xu, M. Lax, and R. R. Alfano, "Time-resolved Fourier optical diffuse tomography," J. Opt. Soc. Am. A **18**, 1535 (2001).

(10) APPENDICES

Temporally and spectrally resolved optical imaging of normal and cancerous human breast tissues

S. K. Gayen, M. Alrubaiee, M. E. Zevallos* and R. R. Alfano
Institute for Ultrafast Spectroscopy and Lasers, New York State Center for Photonic Materials and Applications, Departments of Physics and Electrical Engineering, The City College of the City University of New York 138th Street at Convent Avenue, New York, NY 10031
gayen@scisun.sci.ccny.cuny.edu, alfano@scisun.sci.ccny.cuny.edu

Abstract: Time-sliced and spectroscopic imaging approaches were used to obtain two-dimensional (2-D) transillumination images of a composite *in vitro* human breast tissue sample comprising cancerous and normal fibrous tissues, adipose tissues, and a lymph node. Time-sliced imaging approach used 800-nm, approximately 130-fs duration, 1 kHz repetition-rate pulses from a Ti:sapphire laser system to illuminate the sample, and a gated imaging system that provided a variable-position, ~80 ps-duration electronic gate to record time-sliced 2-D images. Images recorded with earlier temporal slices (approximately, first 100 ps) of the transmitted light highlighted the lymph node and cancerous tissues, while the later slices (later than 300 ps) accentuated the adipose and normal tissues. Spectroscopic imaging arrangement made use of 1225 - 1300 nm light from a chromium-doped forsterite laser for sample illumination, a Fourier space gate and a polarization gate to sort out a fraction of the image-bearing photons, and an InGaAs area camera for recording 2-D images. Marked enhancement of image contrast between the adipose tissue and other tissues in the specimen was observed when the wavelength of imaging light was near resonant with the 1203-nm optical absorption resonance of the adipose tissue. Wavelength-dependent differences in relative light transmission through the normal and cancerous tissues were observed.

OCIS codes: (170.3880) Medical and biological imaging; (170.6920) time-resolved imaging; (290.7050) scattering, turbid media; (170.6510) spectroscopy, tissue diagnostics; (170.3660) light propagation in tissues; (999.999) Optical mammography; (999.999) near-infrared absorption spectroscopy of tissues; (999.999) spectroscopic imaging; (999.999) time-sliced imaging.

Introduction

Optical mammography, imaging of the interior structure of human breast with light, is an active area of optical biomedical imaging research.[1-4] Development of optical breast imaging modalities is of interest for several reasons. Optical imaging methods are noninvasive as no ionizing radiation is involved. Use of different wavelengths of light has the potential to provide diagnostic information. In contrast with x-ray mammography, light-based methods are as apt to image dense breast of a younger patient as that of an older patient. What is even more important, inverse image reconstruction methods using time-resolved or frequency-domain optical measurements may provide three-dimensional (3-D) tomographic breast images.[5-7] The ability to generate ultrashort pulses and colors are two major attributes of light that may be exploited to develop an imaging modality with diagnostic ability.

In this article, we present the results of time-sliced[7] and spectroscopic[8] 2-D transillumination imaging measurements on excised human female breast tissue specimens comprising normal and cancerous tissues. Time-sliced imaging makes use of different temporal slices of the transmitted light to form 2-D images following the illumination of the sample with ultrashort near-infrared (NIR) pulses of light. The thrust of the spectroscopic imaging experiment is to examine if a spectroscopic difference

Proceedings of Inter-Institute Workshop on In Vivo Optical Imaging at the NIH
Amir H. Gandjbakhche (ed.)
© 2000 Optical Society of America

may be used to enhance image contrast, distinguish between different types of tissues in a specimen, and obtain diagnostic information.

Methods and Materials

The time-sliced imaging arrangement used 800-nm, approximately 130-fs duration, 1 kHz repetition-rate pulses from a Ti:sapphire laser and amplifier system[9] for sample illumination, and an ultrafast gated intensified camera system (UGICS) for recording two-dimensional images using picosecond-duration slices of light transmitted through the sample. The UGICS comprised a compact time-gated image intensifier unit fiber-optically coupled to a charge-coupled device (CCD) camera. It provided a minimum gate width of approximately 80 ps whose temporal position could be varied in 25-ps steps over a 20-ns range. The average beam power used in the experiment was approximately 200 mW. The beam was expanded by a beam expander, and a 3-cm diameter central part of it was selected out using an aperture to illuminate the sample. The time-sliced image was recorded by the CCD camera and displayed on a computer.

The experimental arrangement for near-infrared (NIR) spectroscopic imaging made use of 1210-1300 nm continuous-wave mode-locked output of a Cr^{4+}:forsterite laser to illuminate the sample. A Fourier space gate[10] in conjunction with a polarization gate[11] selected out a fraction of the less-scattered image-bearing photons from the strong background of the image-blurring diffuse photons. A 50 mm focal-length camera lens placed on the optical axis at a distance of 50 mm from the aperture in the Fourier gate collected and collimated the low-spatial-frequency light filtered by the aperture and directed it to the 128x128 pixels sensing element of an InGaAs NIR area camera. The average optical power of the incident beam was maintained at approximately 35 mW for all the wavelengths used in the imaging experiment using appropriate neutral density filters. The laser beam was linearly polarized along the horizontal direction.

The composite excised breast tissue sample used in the experiments reported in this article was assembled from tissues obtained following the modified radical mastectomy of a 30-year-old patient. It comprised a lymph node (LN) with surrounding tissues, a piece of adipose (A) tissue, and a piece with normal (N) and cancerous (C) fibrous tissue. Each of the pieces was approximately 5 mm thick, and was pressed into a 5-mm thick quartz cell to ensure uniform sample thickness and good optical contact between the adjacent pieces. According to an accompanying surgical pathology report, the cancer was a poorly differentiated carcinoma, grade III with sarcomatoid features. Figure 1(a) shows a photograph of the exit face of the composite sample wherein the locations of different types of tissues are tentatively outlined and labeled. The tissues were made available to us by National Disease Research Interchange under an IRB approval from the City College of New York.

Results

Time-sliced Imaging

Time-sliced transillumination images of the sample for gate positions of 100 ps and 350 ps are displayed in Figs. 1(b) and 1(c), respectively. The zero position was taken to be the time of arrival of the light pulse through a 5-mm thick quartz cell filled with water. The spatial intensity profiles of the images in Fig. 1(b) and Fig. 1(c) integrated over two 6-pixel wide horizontal areas around the white dashed lines

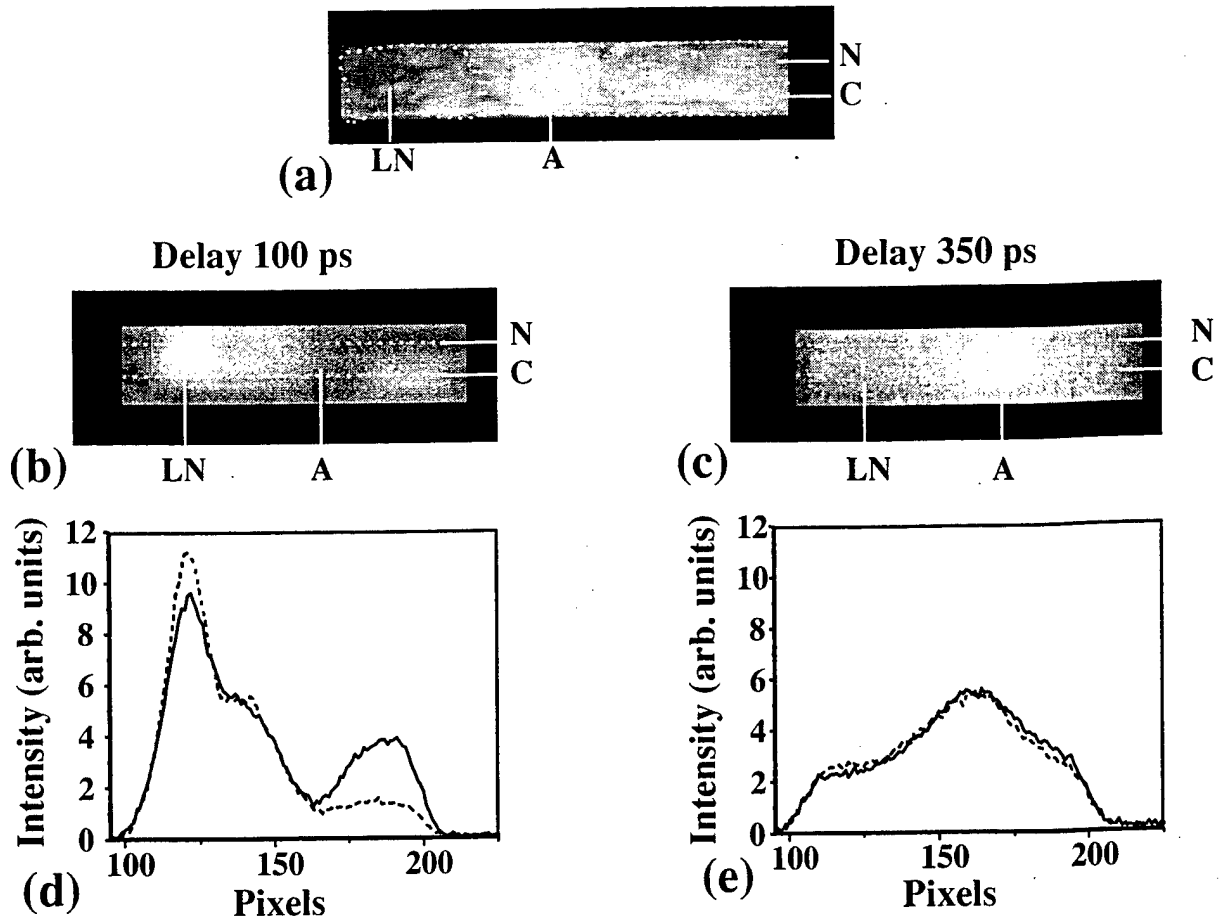

Fig. 1.(a) A photograph of the exit face (the side that faces the camera in the experimental arrangements) of the composite breast tissue sample. LN, lymph node; A, adipose tissue; N, normal fibrous tissue; C, cancerous tissue. Time-sliced transillumination images of the sample for gate delays of (b) 100 ps, and (c) 350 ps. Spatial profile of the integrated intensity distribution along a horizontal area of 6 pixel vertical width around the dashed white line that passes through the normal fibrous tissue (dashed line), or the cancerous tissue (solid line) for a gate delay of (d) 100 ps, and (e) 350 ps.

are presented in Figs. 1(d) and 1(e), respectively. The two areas were chosen such that one included the normal fibrous tissue in the upper right part of the sample while the other included the cancerous tissue in the lower right part to enable close comparison. The time-sliced 100-ps gated image clearly highlights the lymph node, adipose, normal fibrous, and cancerous tissue regions. The contrast is the highest between the lymph node that appears the brightest and the adipose tissue that appears dark in the image. The spatial intensity distributions of the 100-ps image, displayed in Fig. 1(d), show the highest peak in intensity values in the lymph-node region and a marked trough in the adipose tissue region indicating much higher light transmission through the lymph node and much lower transmission through the adipose tissue region at early time. More interesting is the contrast between the cancerous and normal tissues in the 100-ps image. As seen in the right side of the image and the spatial intensity profiles of Fig. 1(d), light transmission through the cancerous tissue is significantly higher than that through the normal tissue.

A markedly different situation is observed in the 350-ps gated image of Fig. 1(c) and the corresponding spatial intensity profiles of Fig. 1(e). The adipose tissue region appears the brightest, and the spatial intensity profile peaks in the adipose tissue region indicating much higher light transmission through the adipose tissue compared to transmission through other tissues in the sample at this later

time. What is even more noteworthy, the difference in light transmission through the normal and cancerous regions that appeared so prominent in the profiles of Fig. 1(d) is not appreciable at this late time. It is reflected by the close overlapping of the two profiles in the regions of the normal and cancerous tissues in the profiles of Fig. 1(e). At intermediate times (not shown in figures) relative light transmission through the lymph node and cancerous tissues decreased while that through adipose and normal fibrous tissues increased with time. Summarizing the time-dependent transit of light, we find that the light transits fastest through the lymph node, followed by that through cancerous fibrous tissue, normal fibrous tissue, and the adipose tissue. Lower scattering or/and higher absorption of light by a particular type of tissue may make its temporal profile peak at an earlier time. Since there is no known absorption of 800-nm light by breast tissues, we attribute the observed time-dependent differences in the relative light transmission to the differences in the light scattering characteristics of these tissues. Our results suggest that lymph node scatters the least, followed by cancerous tissue, normal fibrous tissue, and the adipose tissue.

These results demonstrate that time-sliced imaging can highlight different types of tissues in a sample. What is even more important, it can highlight normal fibrous tissues from poorly differentiated carcinoma (grade III) with sarcomatoid features. It should be noted that more pronounced difference in light scattering characteristics between normal fibrous tissues and infiltrating ductal carcinoma was observed[12] than that observed in this study between normal fibrous tissues and poorly differentiated carcinoma (grade III) with sarcomatoid features. While both types of tumors scatter less than normal fibrous tissue, ductal carcinoma tumor is even less scattering than the poorly differentiated carcinoma (grade III) with sarcomatoid features. Experiments with different types of tumors at different stages of development are needed to generate quantitative data on light scattering characteristics of tumors.

Spectroscopic Imaging

A spectroscopic difference between different types of tissues in a specimen is expected to provide some distinguishable signature in a transillumination image. In order to test if this signature may be realized in practice, we obtained images of the sample with 1225-nm light that is near-resonant with the adipose tissue optical absorption resonance around 1203 nm,[13] as well as, with light of wavelengths away from the resonance. Figures 2(a) and 2(b) show a 'near-resonant image' recorded with 1225-nm light, and a typical 'nonresonant image' recorded with 1300-nm light, respectively. Figures 2(c) and 2(d) display the corresponding spatial intensity profiles. The solid line in each of these figures shows the profile integrated over a 6-pixel wide area around the long dashed line that runs the entire length of the corresponding image and includes the cancerous tissue region in the lower right part of the image. The dashed curve superimposed on the solid curve shows the profile integrated over a 6-pixel wide normal fibrous tissue area around the upper smaller dashed line in the corresponding image. The solid and the dashed curves in the right side of the profiles thus enable comparison of light transport characteristics through normal and cancerous tissues in the specimen.

The salient features of the spectroscopic images and corresponding profiles are: (a) the adipose tissues appear much darker (less light transmission) than other tissues in the near-resonant 1225-nm image as compared to that in the off-resonance 1300-nm image; (b) cancerous tissues appear brighter (higher light transmission) than the normal tissues in both the images; (c) while the overall light transmission through the normal region remains approximately at the same level, that through the cancerous region is significantly higher at 1225 nm than at 1300 nm; (d) transmission through the lymph node exhibits a wavelength-dependent variation as well, being higher at 1300 nm than at 1225 nm. The

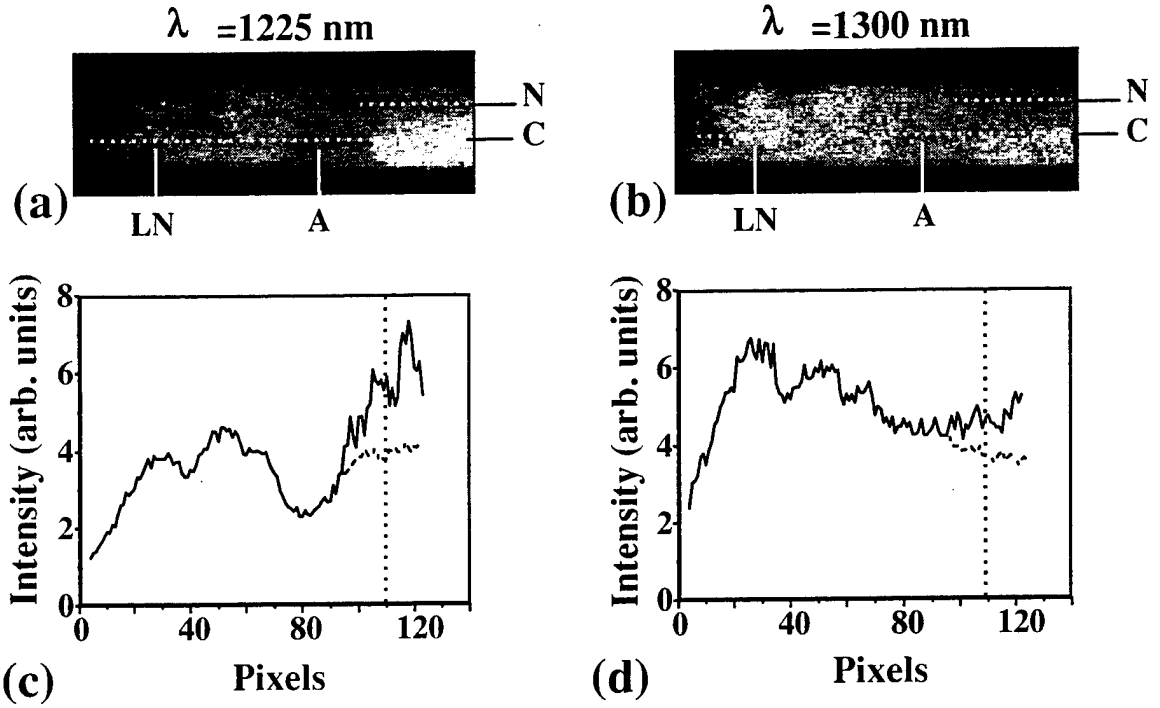

Figure 2. Spectroscopic 2-D transillumination image of the breast tissue sample described in the text for light of wavelength (a) 1225 nm, and (b) 1300 nm. Corresponding spatial profiles are shown in (c) and (d), respectively. Spatial profiles are the integrated intensity distribution along a 6-pixel wide horizontal area around the white dashed line covering the entire length of the sample including the cancerous tissue region (solid line in the profiles) and that around the small dashed line denoting the normal tissue region (broken line in the profiles).

change in image contrast was the maximum for the adipose tissue as the wavelength of imaging light was changed from 1225 to 1300 nm. Adipose tissue region appeared as a much deeper trough in the spatial intensity profile of the 1225-nm image compared to that for the 1300-nm image. For a more quantitative description of the observed behavior, we monitored the image contrast, $C(\lambda) = (I_F - I_A)/(I_F + I_A)$, where $I_A(\lambda)$ is the optimal intensity value at wavelength λ on the spatial profile of the image at the adipose tissue location, and $I_F(\lambda)$ is the corresponding intensity in the immediate fibrous tissue region. Value of contrast at 1225 nm is 0.27 and 0.10 at 1300 nm. As the laser output was tuned away from 1225 nm to off-resonance wavelengths, the contrast between the adipose and fibrous regions in the images decreased from that maximum value of 0.27 towards 0.10. These results clearly demonstrate that an appreciable spectroscopic difference may significantly enhance the contrast between different types of breast tissues in a transillumination image, and is consistent with our previous results with adipose and fibrous human breast tissues.[8]

Even more promising and interesting is the wavelength-dependent difference in light transmission through the cancerous and normal tissues. As a measure of this difference we may monitor the ratio, R of light intensity transmitted through the cancerous tissue to that through the corresponding normal tissue. Taking the averaged intensity values[14] around the middle of the normal and cancerous tissues (Pixel # 110 marked by vertical dashed line in figures 2(c) and 2(d)), we obtain the value of R to be 1.5 for 1225 nm and 1.2 for 1300 nm, a significant difference. We observed similar wavelength-dependent variation in R for ductal carcinoma and normal breast tissue samples as well. More measurements involving normal tissues and tissues with different types and stages of cancer are needed to examine if R can be a parameter whose values would be indicative of cancer.

In summary, the spectroscopic and time-sliced imaging approaches show tissue selectivity. A combined spectroscopic and time-sliced imaging approach along with inverse image reconstruction method has the potential to provide more information even than the x-ray techniques.

Acknowledgments

We acknowledge J. Evans for technical help. The work is supported in part by the New York State Science and Technology Foundation, NASA IRA Program, USAMMRC, and DOE.

*Currently with IBM Microelectronics Division, Hopewell Junction, New York.

References and Notes

1. M. Cutler, "Transillumination as an aid in the diagnosis of breast lesion," Surg. Gynecol. Obstet. **48**, 721-730 (1929).
2. E. Gratton, W. W. Mantulin, M. J. vande Ven, J. B. Fishkin, M. B. Maris, and B. Chance, "A novel approach to laser tomography," Bioimaging, **1**, pp. 40-46, 1993.
3. G. J. Muller, R. R. Alfano, S. R. Arridge, J. Beuthan, E. Gratton, M. Kaschke, B. R. Masters, S. Svanberg and P. van der Zeect (editors), *Medical Optical Tomography: Functional Imaging and Monitoring*, Vol. IS 11, SPIE Institute Series, (SPIE, Bellingham, Washington, 1993).
4. L. Wang, P.P. Ho, G. Liu, G. Zhang, and R.R. Alfano, "Ballistic 2-D imaging through scattering walls using an ultrafast optical Kerr Gate", Science **253**, pp. 769-771, 1991.
5. For a recent review of the inverse reconstruction methods, see S. R. Arridge and J. C. Hebden, "Optical imaging in medicine: II. modeling and reconstruction," Phys. Med. Biol. **42**, 841-853 (1997).
6. M. A. O'Leary, D. A. Boas, B. Chance and A. G. Yodh, "Experimental images of heterogeneous turbid media by frequency-domain diffusing-photon tomography," Opt. Lett. **20**, 426-428 (1995).
7. W. Cai, S. K. Gayen, M. Xu, M. Zevallos, M. Alrubaiee, M. Lax and R. R. Alfano, "Optical tomographic image reconstruction from ultrafast time-sliced transmission measurements," Appl. Opt. **38**, 4237-4246 (1999).
8. S. K. Gayen, M. E. Zevallos, M. Alrubaiee, and R. R. Alfano, "Near-infrared laser spectroscopic imaging: a step towards diagnostic optical imaging of human tissues," Laser Life Sci. **8**, 187-198 (1999).
9. Q. Fu, F. Seier, S. K. Gayen and R. R. Alfano, "High-average-power kilohertz-repetition-rate sub-100-fs Ti:sapphire amplifier system," Opt. Lett. **22**, 712-714 (1997).
10. J. J. Dolne, K. M. Yoo, F. Liu and R. R. Alfano, "IR Fourier space gate and absorption imaging through random media," Laser Life Sci. **6**, 131-141 (1994).
11. S. G. Demos and R. R. Alfano, "Temporal gating in highly scattering media by the degree of optical polarization," Opt. Lett. **21**, 161-163 (1996).
12. S. K. Gayen and R. R. Alfano, "Sensing lesions in tissues with light," Opt. Express **4**, 475-480 (1999).
13. F. A. Marks, "Optical determination of the hemoglobin oxygenation state of breast biopsies and human breast cancer xenografts in nude mice," in *Proceedings of Physiological Monitoring and Early Detection Diagnostic Methods*, Thomas S. Mang and Abraham Katzir (eds.), SPIE **1641**, Bellingham, Washington, pp. 227-237, 1992.
14. A 5-point smoothed average of intensity values around Pixel #110 was used to reduce the effect of noise in determining the ratio.

PHYSICAL REVIEW E, VOLUME 63, 016606

Analytical solution of the polarized photon transport equation in an infinite uniform medium using cumulant expansion

W. Cai, M. Lax, and R. R. Alfano

Institute for Ultrafast Spectroscopy and Lasers, New York State Center of Advanced Technology for Ultrafast Photonic Materials and Applications, Department of Physics, The City College and Graduate Center of City University of New York, New York, New York 10031

(Received 27 March 2000; published 20 December 2000)

An analytical solution for time-dependent polarized photon transport equation in an infinite uniform isotropic medium is studied using a circular representation of the polarized light and expansion in the generalized spherical functions. We extend our cumulant approach for solving the scalar (unpolarized) photon transport equation to the vector (polarized) case. As before, an exact angular distribution is obtained and a cumulant expansion is derived for the polarized photon distribution function. By a cutoff at the second cumulant order, a Gaussian analytical approximate expression of the polarized photon spatial distribution is obtained as a function of the direction of light and time, whose average center position and half-width are always exact. The central limit theorem claims that this spatial distribution approaches accuracy in detail when the number of collisions or time becomes large. The analytical expression of cumulants up to an arbitrary high order is also derived, which can be used for calculating a more accurate polarized photon distribution through a numerical Fourier transform. Contrary to what occurs in other approximation techniques, truncation of the cumulant expansion at order n is exact at that order and cumulants up to and including order n remain unchanged when higher orders are added, at least as applied in our photon transport equation.

DOI: 10.1103/PhysRevE.63.016606 PACS number(s): 42.25.Fx, 42.25.Ja, 42.25.Dd, 42.68.Ay

I. INTRODUCTION

Study of the polarized photon transport has lasted for many years since the polarized photon transport equation (PPTE) was formulated by Gans [1] and by Chandrasekhar [2]. Recently, polarization analysis of light migrating in a multiple-scattering medium has been applied to broad fields, such as diagnostics of biological tissues [3–5], atmosphere monitoring [6], and communications. One goal is to develop optical tomography with polarization analysis to enhance ability in image reconstruction of objects inside scattering media. Because of the depolarization effect in a highly scattering medium, scattered photons maintaining polarization are those near ballistic and snake like, which suffer less multiple scattering. Therefore, a tomographic approach using polarized photons will automatically exclude multiple-scattered diffusive photons which blur images. In order to build a proper forward model for tomography using a polarization analysis, a theoretical study of the propagation of polarized light in scattering media becomes practically important.

In polarized photon transport, the intensity of polarized light scattered from a scatterer along a certain direction is determined by many scattering processes at different scattering planes consisting in a ray scattered from the scatterer and rays incident to the scatterer from different directions. In order to properly describe this process, Kuščer and Ribarič [7] employed a circular representation of the polarized components of light and an expansion by generalized spherical functions [8] (or rotation matrices in angular momentum theory [9,10]). The phase matrix, hence, can be analytically expressed by the angular parameters of the incident and scattered rays in fixed coordinates. Based on this formalism, Herman and Lenoble [11] studied the asymptotic behavior of the polarized radiation field at great depths. Domke [12] constructed a system of singular eigenfunctions of the PPTE, for which an integral equation and then a recurrence relation were derived. However, to our knowledge, an explicit analytical expression of the solution of the PPTE has not been obtained. Numerical methods, mainly, Monte Carlo simulations, are the main tools in recent theoretical investigations of light polarization in multiple-scattering media [5,13].

In this paper we derive an analytical solution of the time-dependent PPTE in an infinite uniform medium. Based on our results, inverse image reconstruction of objects inside a scattering medium using polarized light can be developed. The 4×4 phase matrix is assumed to depend only on the scattering angle Θ in the scattering plane: $\mathbf{P}(\mathbf{s},\mathbf{s}_0)=\mathbf{P}(\mathbf{s}\cdot\mathbf{s}_0)=\mathbf{P}(\cos\Theta)$. Under this assumption an arbitrary phase matrix can be handled. By use of the circular representation of polarized light and an expansion in the generalized spherical function [7,9], we extend our approach in solving the scalar (unpolarized) photon transport equation [14,15] using a cumulant expansion to the vector (polarized) case. Terminating at second order, an approximate Gaussian polarized photon spatial distribution is obtained for a given light direction $\mathbf{s}$ as a function of time t. Our solution for the distribution in angle is exact, as are the first and second cumulants in space at any angle and time, which guarantees the correct central position and the correct half-width of the spatial distribution. After many scattering events have taken place, the central limit theorem claims that the spatial Gaussian distribution calculated will become accurate in detail, since all cumulants higher than the second approach small values relative to the appropriate power of the second cumulant. At early times, the spatial distribution is narrow: hence, a distribution function, the mean position and half-width of which are exact, may provide an adequate description of a

 ©2000 The American Physical Society

polarized beam in the presence of noise and finite instrument resolution. An analytical expression of cumulants up to an arbitrary high order is also derived. Using these higher-order cumulants, through a numerical Fourier transform, a more accurate solution of the PPTE can be calculated.

The paper is organized as follows. Section II provides the preliminary formula of the PPTE, the circular representation of polarized light and the generalized spherical function, which have been published in previous literature. In Sec. III, an exact solution of the angular distribution of the polarized light is derived and an expression in the cumulant expansion of the polarized photon distribution is presented. In Sec. IV, by terminating the cumulant expansion at second order a Gaussian approximate spatial distribution as a function of light direction s and time t is obtained, and the exact expressions of the first and second cumulants are derived. In Sec. V, an expression of cumulants up to an arbitrary high order is derived. A brief discussion and summary then follows in Sec. VI. In Appendix A, the expressions for coefficients $[B^l_{mn_0}]_i$ in Eq. (15) are presented. In Appendix B, analytical formulas for evaluating integrals in Eq. (42) are derived.

II. CIRCULAR REPRESENTATION AND GENERALIZED SPHERICAL FUNCTIONS

In this section, we summarize the description of polarized light propagation in a scattering medium discussed in the previous literature.

Considering a light beam traveling along a direction s, we choose a reference plane through the direction of propagation. Two complex components of the electric field **E**, such as $E_\parallel = a_1 \exp(i\delta_1)$, the component parallel to the reference plane, and $E_\perp = a_2 \exp(i\delta_2)$, the component perpendicular to the reference plane, can be used to describe a single coherent beam. Four real components were introduced by Stokes [16], each with the dimension of the square of a field or, more precisely, an intensity. The four Stokes parameters are collected into a four-element array $\mathbf{I}^{SP}=[I,Q,U,V]$ [17]. The component I is the total intensity:

$$I=\langle a_1^2\rangle+\langle a_2^2\rangle=\langle |E_\parallel|^2+|E_\perp|^2\rangle. \tag{1a}$$

The component Q describes a linear polarization:

$$Q=\langle a_1^2\rangle-\langle a_2^2\rangle=\langle |E_\parallel|^2-|E_\perp|^2\rangle. \tag{1b}$$

The component U describes a linear polarization 45° relative to the reference plane:

$$U=\langle 2a_1a_2\cos\delta\rangle=\langle |E(45°)|^2-|E(-45°)|^2\rangle, \tag{1c}$$

where

$$E(\pm 45°)\equiv 2^{-1/2}(E_\parallel \pm E_\perp).$$

The last component V is the difference between the intensities of right- and left-circularly polarized light:

$$V=\langle 2a_1a_2\sin\delta\rangle=\langle |E_R|^2-|E_L|^2\rangle, \tag{1d}$$

where the right- and left-circular components of field are

$$E_L^R\equiv 2^{-1/2}(E_\parallel \mp iE_\perp).$$

In Eq. (1), $\delta=\delta_1-\delta_2$; the angular brackets mean the average over many waves with independent phases in a light beam.

To give further physical meaning to the symbols, we note that the use of the Cauchy-Schwarz inequality leads to the inequality

$$I^2\geqslant Q^2+U^2+V^2. \tag{2}$$

For a coherent beam, which requires no averages in Eqs. 1(a)–1(d), the equality is automatically obeyed. The opposite extreme case is unpolarized light for which

$$Q=U=V=0,$$

and the total intensity I is totally incoherent. More generally, the difference between the left- and right-hand sides of the inequality, Eq. (2), constitutes the incoherent part of the total intensity.

The kinetic equation for a polarized photon distribution function $\mathbf{I}(\mathbf{r},\mathbf{s},t)$ as a function of time t, position **r**, and direction **s**, in an infinite uniform medium, from a point pulse polarized light source, $\mathbf{I}^{(0)}\delta(\mathbf{r}-\mathbf{r}_0)\delta(\mathbf{s}-\mathbf{s}_0)\delta(t-0)$, is given by [2]

$$\begin{aligned}\partial\mathbf{I}(\mathbf{r},\mathbf{s},t)/\partial t+c\mathbf{s}\cdot\nabla_{\mathbf{r}}\mathbf{I}(\mathbf{r},\mathbf{s},t)+\mu_a\mathbf{I}(\mathbf{r},\mathbf{s},t)\\ =\mu_s\int \mathbf{P}(\mathbf{s},\mathbf{s}')[\mathbf{I}(\mathbf{r},\mathbf{s}',t)-\mathbf{I}(\mathbf{r},\mathbf{s},t)]d\mathbf{s}'\\ +\mathbf{I}^{(0)}\delta(\mathbf{r}-\mathbf{r}_0)\delta(\mathbf{s}-\mathbf{s}_0)\delta(t-0).\end{aligned} \tag{3}$$

The quantities in the Stokes parameter (SP) representation will be marked by adding a superindex, for example, $\mathbf{I}^{SP}$. With a rotation of the reference plane through an angle $\alpha \geqslant 0$ (in the counterclockwise direction, when looking in the direction of propagation) around the light propagation direction, **I** varies as $\mathbf{I}'=\mathbf{L}(\alpha)\mathbf{I}$. In the SP representation, the relation is given by

$$\begin{bmatrix} I' \\ Q' \\ U' \\ V' \end{bmatrix} = \begin{bmatrix} 1 & 0 & 0 & 0 \\ 0 & \cos 2\alpha & \sin 2\alpha & 0 \\ 0 & -\sin 2\alpha & \cos 2\alpha & 0 \\ 0 & 0 & 0 & 1 \end{bmatrix} \begin{bmatrix} I \\ Q \\ U \\ V \end{bmatrix}. \tag{4}$$

Usually, a meridian plane containing the z axis and the light direction s is used as the reference plane for the description of the polarization state [2,9] as shown in Fig. 1. In Eq. (3), c is the light speed in the medium, μ_s is the scattering rate (per unit time), μ_a is the absorption rate, and $\mathbf{P}(\mathbf{s},\mathbf{s}')$ is a 4×4 phase matrix. The following form of the 4×4 phase matrix [9] is used:

$$\mathbf{P}(\mathbf{s},\mathbf{s}')=\mathbf{L}(\pi-\chi)\mathbf{P}(\cos\Theta)\mathbf{L}(-\chi'), \tag{5}$$

where Θ is the angle between light rays before and after scattering, and the matrices $\mathbf{L}(-\chi')$ and $\mathbf{L}(\pi-\chi)$ are those required to rotate meridian planes before and after scattering

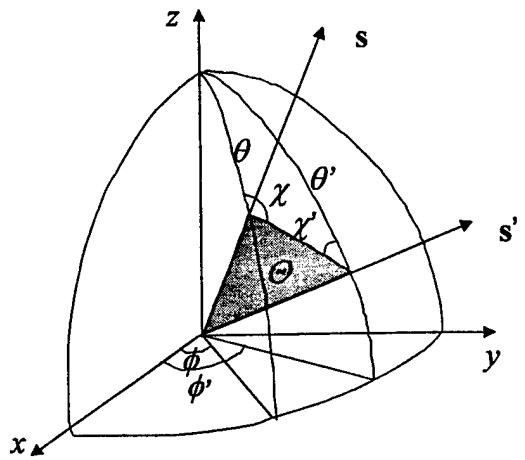

FIG. 1. Geometry of the scattering plane and the reference planes related to the incident ray, $\mathbf{s}'(\theta',\phi')$, and the scattered ray, $\mathbf{s}(\theta,\phi)$. The dark plane is the scattering plane. χ is the angle between the meridian plane (**s**,**z**) and the scattering plane. χ' is the angle between the meridian plane ($\mathbf{s}'$,**z**) and the scattering plane.

onto or from a local scattering plane, as shown in Fig. 1. The intrinsic property of scattering mechanism is described by the 4×4 scattering function $\mathbf{P}(\cos\Theta)$, which involves $\cos\Theta=\mathbf{s}\cdot\mathbf{s}'$.

It is convenient to use a representation of the polarized light in which $\mathbf{L}(\alpha)$ is diagonal, rather than Eq. (4). A circular parameter representation (CP) was first proposed by Kuščer and Ribarič [7]. Later, a more precise definition of the CP, which matches with the initial definition of polarized light in the SP representation by Chandrasekhar [2], was presented by Hovenier and van der Mee [9]. Hereafter we use the definition of the CP in Ref. [9], which is given by $\mathbf{I}^{\mathrm{CP}}=[I_2,I_0,I_{-0},I_{-2}]$, where $I_0=(I+V)/2$, $I_{-0}=(I-V)/2$, $I_2=(Q+iU)/2$, and $I_{-2}=(Q-iU)/2$, or $\mathbf{I}^{\mathrm{CP}}=\mathbf{T}\mathbf{I}^{\mathrm{SP}}$, with

$$\mathbf{T}=\frac{1}{2}\begin{bmatrix}0&1&i&0\\1&0&0&1\\1&0&0&-1\\0&1&-i&0\end{bmatrix}. \tag{6}$$

In the CP, a rotation of the reference plane through an angle α around the light direction causes I_m to be multiplied by $\exp(-im\alpha)$. Notice that I_0 and I_{-0} actually have the same rotational property. For the phase matrix, the transform $\mathbf{P}^{\mathrm{CP}}=\mathbf{T}\mathbf{P}^{\mathrm{SP}}\mathbf{T}^{-1}$ is given between two representations.

In the CP, it is convenient to expand the phase matrix $\mathbf{P}^{\mathrm{CP}}$ using generalized spherical functions (GSF's). The generalized spherical functions, which are related to irreducible representations of the rotation group on three nonzero Euler's angles, are defined as follows [8].

For $l\geqslant\sup(|m|,|n|)$ and $\mu=\cos\theta$,

$$P^l_{m,n}(\mu)=A^l_{m,n}(1-\mu)^{-(n-m)/2}(1+\mu)^{-(n+m)/2}\times\frac{d^{l-n}}{d\mu^{l-n}}[(1-\mu)^{l-m}(1+\mu)^{l+m}], \tag{7}$$

with

$$A^l_{m,n}=\frac{(-1)^{l-m}(i)^{n-m}}{2^l(l-m)!}\left[\frac{(l-m)!(l+n)!}{(l+m)!(l-n)!}\right]^{1/2}.$$

This function is directly related [9] to the rotation matrix $d^l_{mn}(\theta)$ in angular momentum theory [10] by $d^l_{mn}(\theta)=(i)^{n-m}P^l_{mn}(\cos\theta)$. Some symmetry properties of $P^l_{m,n}(\mu)$ are $P^l_{m,n}(\mu)=P^l_{n,m}(\mu)=P^l_{-m,-n}(\mu)$. The orthogonality relation for $P^l_{m,n}(\mu)$ is given by [8,9]

$$(-1)^{m+n}\int_{-1}^{1}P^l_{m,n}(\mu)P^{l'}_{m,n}(\mu)d\mu=\frac{2}{2l+1}\delta_{l,l'}. \tag{8}$$

The phase matrix in the CP can be expressed using the generalized spherical functions [7,9]. For notational simplicity, in the following the quantities without a superindex are understood to be in the CP. Denoting $\mathbf{s}=(\mu,\phi)$ and $\mathbf{s}'=(\mu',\phi')$, the addition theorem of GSF's [9] is given by (see Fig. 1)

$$\exp(im\chi)P^l_{m,n}(\cos\Theta)\exp(in\chi')=(-1)^{m+n}\sum_{s=-l}^{l}(-1)^sP^l_{m,s}(\mu)P^l_{s,n}(\mu')\times\exp[-is(\phi-\phi')]. \tag{9}$$

Using this addition theorem of GSF's, the variables χ, χ', and Θ in Eq. (5) can be eliminated, and the components of the phase matrix in the CP can be expressed using the angular parameters of the incident and scattered ray in fixed coordinates. If we expand elements of the CP phase matrix in the scattering plane, $P_{mn}(\cos\Theta)$, by GSF's,

$$P_{mn}(\cos\Theta)=\frac{1}{4\pi}\sum_l p^l_{mn}P^l_{m,n}(\cos\Theta),$$

then, using Eq. (9), the 4×4 phase matrix in fixed coordinates can be written as

$$P_{mn}(\mu,\phi;\mu',\phi')=\frac{1}{4\pi}\sum_l p^l_{mn}\sum_{s=-l}^{l}(-1)^sP^l_{m,s}(\mu)P^l_{s,n}(\mu')\times\exp[-is(\phi-\phi')], \tag{10}$$

with indices $m,n=2,0,-0,-2$ and $l\geqslant\sup(|m|,|n|)$.

The coefficients p^l_{mn} provide an intrinsic description of the scattering mechanism. In most useful cases, the coefficients p^l_{mn} have the properties [7,9] that (i) p^l_{mm} and p^l_{m-m} are real, (ii) $p^l_{mn}=p^l_{nm}=p^l_{-m-n}$, and (iii) $p^l_{20}=[p^l_{2-0}]^*$ (the asterisk means complex conjugate). Therefore, for each $l\geqslant2$, there are six independent real elements p^l_{00}, p^l_{22}, p^l_{0-0}, p^l_{2-2}, $\mathrm{Re}[p^l_{20}]$, $\mathrm{Im}[p^l_{20}]$. For $l=0$ or 1, only p^l_{00} and p^l_{0-0} are nonzero. These numerical coefficients were calculated using Mie theory for some examples by De Rooij and van der Stap [18]. These p^l_{mn}, together with μ_s and μ_a, are

parameters that describe the nature of the scattering process and are treated as known in our solution of the transport equation.

III. DERIVATION

Having the above knowledge, we analytically solve Eq. (3) in an infinite uniform isotropic medium. Using a procedure similar to that discussed in Refs. [14] and [15], we first study the dynamics of the photon distribution in the light direction space in the CP, $\mathbf{F}(\mathbf{s},\mathbf{s}_0,t)$, which is a vector of four components, on a spherical surface for s of radius 1. The kinetic equation for $\mathbf{F}(\mathbf{s},\mathbf{s}_0,t)$ can be obtained by integrating Eq. (3) over whole space r. The spatial independence of μ_s, μ_a, and $\mathbf{P}(\mathbf{s},\mathbf{s}')$ retains translation invariance. Thus the integral of Eq. (3) obeys

$$\partial\mathbf{F}(\mathbf{s},\mathbf{s}_0,t)/\partial t+\mu_a\mathbf{F}(\mathbf{s},\mathbf{s}_0,t) +\mu_s\left[\mathbf{F}(\mathbf{s},\mathbf{s}_0,t)-\int \mathbf{P}(\mathbf{s},\mathbf{s}')\mathbf{F}(\mathbf{s}',\mathbf{s}_0,t)ds'\right] =\mathbf{I}^{(0)}\delta(\mathbf{s}-\mathbf{s}_0)\delta(t-0). \tag{11}$$

Since the integral of the gradient term over all space vanishes, as shown in Ref. [14], if we expand $\mathbf{F}(\mathbf{s},\mathbf{s}_0,t)$ in GSF's, its l components should not be coupled to each other. The mth component of $\mathbf{F}(\mathbf{s},\mathbf{s}_0,t)$, with the initial polarization in unit n_0 state, can be expanded in GSF's in the following form:

$$F_{mn_0}(\mathbf{s},\mathbf{s}_0,t)=\sum_l F^l_{mn_0}(t)\sum_s (-1)^s P^l_{m,s}(\mu)P^l_{s,n_0}(\mu_0) \times\exp[-is(\phi-\phi_0)]\exp(-\mu_a t), \tag{12}$$

with m, $n_0=2,0,-0,-2$, $l\geqslant\sup(|m|,|n|)$. When $\mathbf{s}_0$ is set along the z direction and the initial reference plane is set as the x-o-z plane, Eq. (12) specializes to

$$F_{mn_0}(\mathbf{s},\hat{\mathbf{z}},t)=\sum_l F^l_{mn_0}(t)P^l_{m,n_0}(\mu)\exp(-in_0\phi)\exp(-\mu_a t). \tag{13}$$

Substituting Eq. (12) [or Eq. (13)] into Eq. (11), using the expression, Eq. (10), of the phase matrix, and the orthogonality relation of GSF's, Eq. (8), an analytically solvable equation for $F^l_{mn_0}(t)$ for each l is obtained:

$$dF^l_{mn_0}(t)/dt=\sum_n \Pi^l_{mn}F^l_{nn_0}(t), \tag{14a}$$

with $\Pi^l_{mn}=\mu_s[\delta_{m,n}-p^l_{mn}/(2l+1)]$. The initial condition $F_m(\mathbf{s},\mathbf{s}_0,t=0)=\delta_{m,n_0}\delta(\mathbf{s}-\mathbf{s}_0)$ and the orthogonality relation, Eq. (8), lead to

$$F^l_{mn_0}(t=0)=\delta_{m,n_0}(2l+1)/4\pi. \tag{14b}$$

The solution of Eq. (14) can be expanded in terms of eigenstates:

$$F^l_{mn_0}(t)=\frac{2l+1}{4\pi}\sum_i [B^l_{mn_0}]_i\exp(-\lambda^l_i t),\quad i=1,2,3,4, \tag{15}$$

with the eigenvalues given by

$$\lambda^l_i=(1/2)\Bigg\{(\Pi^l_{00}+\Pi^l_{22}\pm\Pi^l_{0-0}\pm\Pi^l_{2-2}) +\Bigg[(\Pi^l_{00}-\Pi^l_{22}\pm\Pi^l_{0-0}\mp\Pi^l_{2-2})^2 +16\begin{Bmatrix}+\mathrm{Re}(\Pi_{20})\\-\mathrm{Im}(\Pi_{20})\end{Bmatrix}^2\Bigg]^{1/2}\Bigg\}, \tag{16}$$

for $i=1,2$, and for $i=3,4$, the sign+before square brackets in Eq. (16) is replaced by $-$. The constant coefficients $[B^l_{mn_0}]_i$ can be analytically determined using standard linear algebra from the initial condition, Eq. (14b). A detailed expression for $[B^l_{mn_0}]_i$ is presented in Appendix A.

Equation (12) [or Eq. (13)], combined with Eqs. (15) and (16) and the coefficients $[B^l_{mn_0}]_i$ in Appendix A, provides an exact CP solution in the light direction space. In the SP representation, we have

$$\mathbf{F}^{\mathrm{SP}}(\mathbf{s},\mathbf{s}_0,t)=\mathbf{T}^{-1}\mathbf{F}(\mathbf{s},\mathbf{s}_0,t)\mathbf{T}. \tag{17}$$

It can be proved that all components of $\mathbf{F}^{\mathrm{SP}}(\mathbf{s},\mathbf{s}_0,t)$ are real numbers. The mth component $[m=I,Q,U,V]$ of the angular distribution function in the SP representation, with the initial polarized state $\mathbf{I}^{\mathrm{SP}(0)}$, is obtained by

$$F^{\mathrm{SP}}_m(\mathbf{s},\mathbf{s}_0,t)=[\mathbf{F}^{\mathrm{SP}}(\mathbf{s},\mathbf{s}_0,t)\mathbf{I}^{\mathrm{SP}(0)}]_m. \tag{18}$$

Equation (17) serves as the exact Green's function of polarized light propagation in the light direction space. Since in an infinite uniform medium this function is independent of the source position $\mathbf{r}_0$, requirements for a Green's function are satisfied: especially, the Chapman-Kolmogorov condition is obeyed: $\int ds'\,\mathbf{F}^{\mathrm{SP}}(\mathbf{s}'',\mathbf{s}',t-t')\mathbf{F}^{\mathrm{SP}}(\mathbf{s}',\mathbf{s},t'-t_0)=\mathbf{F}^{\mathrm{SP}}(\mathbf{s}'',\mathbf{s},t-t_0)$. In fact, in an infinite uniform medium, this propagator determines all time evolution of polarized light, including its spatial distribution, because displacement is an integration of velocity, $c\mathbf{s}(t)$, over time. The mth component $[m=I,Q,U,V]$ of the photon distribution function in the SP representation, $I^{\mathrm{SP}}_m(\mathbf{r},\mathbf{s},t)$, with the source located at $\mathbf{r}_0=0$, the initial direction $\mathbf{s}_0$, and the initial polarization $\mathbf{I}^{\mathrm{SP}(0)}$, is given by

$$I^{\mathrm{SP}}_m(\mathbf{r},\mathbf{s},t)=\left\langle \delta\left(\mathbf{r}-c\int_0^t\mathbf{s}(t')dt'\right)\delta(\mathbf{s}(t)-\mathbf{s})\right\rangle^{\mathrm{SP}}_m, \tag{19}$$

where $\langle\cdots\rangle^{\mathrm{SP}}_m$ means the mth component of the ensemble average in the light direction space in the SP representation. The first δ function ensures that the displacement $\mathbf{r}-0$ is given by a path integral. The second δ function assures the correct final value of the direction. Equation (19) is a formally exact solution, but cannot be evaluated directly. We make a Fourier transform for the first δ function in Eq. (19), then make a cumulant expansion [19], and obtain

$$I_m^{\mathrm{SP}}(\mathbf{r},\mathbf{s},t)=F_m^{\mathrm{SP}}(\mathbf{s},\mathbf{s}_0,t)\frac{1}{(2\pi)^3}\int d\mathbf{q}\exp\Bigg\{ i\mathbf{q}\cdot\mathbf{r}+\sum_{k=1}^{\infty}\frac{(-ic)^k}{k!}\sum_{j_k}\cdots\sum_{j_1} q_{j_k}\cdots q_{j_1}$$

$$\times\left[\left\langle\int_0^t dt_k\cdots\int_0^t dt_1\, T[s_{j_k}(t_k)\cdots s_{j_1}(t_1)]\right\rangle_c\right]_m^{\mathrm{SP}}\Bigg\}, \tag{20}$$

where T denotes time-ordered multiplication [20] and $F_m^{\mathrm{SP}}(\mathbf{s},\mathbf{s}_0,t)$ is given by Eq. (18). In Eq. (20) the index c denotes a cumulant, which is defined in textbooks of statistics [21] and statistical physics [19]. As for an arbitrary random variable A, we have $\langle A\rangle_c=\langle A\rangle$, $\langle A^2\rangle_c=\langle A^2\rangle-\langle A\rangle\langle A\rangle$, and a general expression relating $\langle A^i\rangle$ and $\langle A^i\rangle_c$, which is given by

$$\langle A^i\rangle=i!\sum_{i_1,i_2,\ldots}\frac{1}{i_1!}\left(\frac{\langle A\rangle}{1!}\right)^{i_1}\frac{1}{i_2!}\left(\frac{\langle A^2\rangle_c}{2!}\right)^{i_2}\cdots\frac{1}{i_n!}\left(\frac{\langle A^n\rangle_c}{n!}\right)^{i_n}\cdots\delta(i-i_1-2i_2-\cdots-ni_n-\cdots), \tag{21}$$

Hence, if $\langle A^i\rangle$, $i=1,2,\ldots,k$, have been calculated, $\langle A^i\rangle_c$, $i=1,2,\ldots,k$, can be recursively obtained and conversely [19]. The kth moment (the term without index c) which, according to the cumulant expansion theorem, is related to $\int d\mathbf{r}\, r_{j_k}\cdots r_{j_1}I_m^{\mathrm{SP}}(\mathbf{r},\mathbf{s},t)$. This moment can be evaluated using a standard time-dependent Green's function approach, which is given by

$$\left[\left\langle\int_0^t dt_k\cdots\int_0^t dt_1\, T[s_{j_k}(t_k)\cdots s_{j_1}(t_1)]\right\rangle\right]_m^{\mathrm{SP}}$$

$$=\frac{1}{F_m^{\mathrm{SP}}(\mathbf{s},\mathbf{s}_0,t)}\Bigg\{\Bigg[\int_0^t dt_k\int_0^{t_k}dt_{k-1}\cdots\int_0^{t_2}dt_1\int d\mathbf{s}^{(k)}\int d\mathbf{s}^{(k-1)}\cdots\int d\mathbf{s}^{(1)}\mathbf{F}^{\mathrm{SP}}(\mathbf{s},\mathbf{s}^{(k)},t-t_k)s_{j_k}^{(k)}$$

$$\times\mathbf{F}^{\mathrm{SP}}(\mathbf{s}^{(k)},\mathbf{s}^{(k-1)},t_k-t_{k-1})s_{j_{k-1}}^{(k-1)}\cdots\mathbf{F}^{\mathrm{SP}}(\mathbf{s}^{(2)},\mathbf{s}^{(1)},t_2-t_1)s_{j_1}^{(1)}\mathbf{F}^{\mathrm{SP}}(\mathbf{s}^{(1)},\mathbf{s}_0,t_1-0)\mathbf{I}^{\mathrm{SP}(0)}\Bigg]_m+(\mathrm{perm.})\Bigg\}, \tag{22}$$

where the abbreviation "perm" means all $k!-1$ terms obtained by permutation of $\{j_i\}$, $i=1,\ldots,k$, from the first term.

In Eq. (22), $\mathbf{F}^{\mathrm{SP}}(\mathbf{s}^{(i)},\mathbf{s}^{(i-1)},t_i-t_{i-1})$ is given by Eq. (17). Since Eq. (22) is obtained using a Green's function approach without making any approximation and Eq. (17) is an exact expression of the angular Green's function, Eq. (22) provides an exact formula for the kth moment. If we are able to exactly evaluate Eq. (22) up to kth order, through Eq. (21), we can obtain the exact cumulants of the distribution up to the kth order.

IV. GAUSSIAN APPROXIMATION OF THE DISTRIBUTION

Terminating Eq. (20) at second order of the cumulant and setting $\mathbf{s}$ in Cartesian coordinates, integration over $\mathbf{q}$ in Eq. (20) can be analytically performed, which leads to the following Gaussian approximation expression of the polarized photon distribution. When the initial $\mathbf{s}_0$ is set along $\mathbf{z}$, it is given by

$$I_m^{\mathrm{SP}}(\mathbf{r},\mathbf{s},t)=\frac{F_m^{\mathrm{SP}}(\mathbf{s},\hat{\mathbf{z}},t)}{(4\pi)^{3/2}}\frac{1}{[\det D_m^{\mathrm{SP}}]^{1/2}}\exp\Bigg[-\frac{1}{4}[(D_m^{\mathrm{SP}})^{-1}]_{\alpha\beta}$$

$$\times(r_\alpha-\langle R_\alpha\rangle_m^{\mathrm{SP}})(r_\beta-\langle R_\beta\rangle_m^{\mathrm{SP}})\Bigg], \tag{23}$$

with $m=I,Q,U,V$ and $\alpha,\beta=x,y,z$. In Eq. (23), $\langle R_\alpha\rangle_m^{\mathrm{SP}}$ represents the position of the average center of the distribution, and $[D_m^{\mathrm{SP}}]_{\alpha\beta}$ is related to the half-width of the spread of the distribution, which is given by

$$[D_m^{\mathrm{SP}}]_{\alpha\beta}=[\langle R_\alpha R_\beta\rangle_m^{\mathrm{SP}}-\langle R_\alpha\rangle_m^{\mathrm{SP}}\langle R_\beta\rangle_m^{\mathrm{SP}}]/2. \tag{24}$$

$\langle R_\alpha\rangle_m^{\mathrm{SP}}$ in Eq. (23) and $\langle R_\alpha R_\beta\rangle_m^{\mathrm{SP}}$ in Eq. (24) can be evaluated using, separately, the first order and the second order of Eq. (22):

$$\langle R_\alpha\rangle_m^{\mathrm{SP}}\equiv c\left\langle\int_0^t dt' s_\alpha(t')\right\rangle_m^{\mathrm{SP}}$$

$$=\frac{c}{F_m^{\mathrm{SP}}(\mathbf{s},\hat{\mathbf{z}},t)}\left[\int_0^t dt'\int d\mathbf{s}'\mathbf{F}^{\mathrm{SP}}(\mathbf{s},\mathbf{s}',t-t')s'_\alpha\right.$$

$$\left.\times\mathbf{F}^{\mathrm{SP}}(\mathbf{s}',\hat{\mathbf{z}},t')\mathbf{I}^{\mathrm{SP}(0)}\right]_m \tag{25}$$

and

$$\langle R_\alpha R_\beta\rangle_m^{\mathrm{SP}} \equiv c^2\left\langle \int_0^t dt' \int_0^t dt'' T[s_\alpha(t')s_\beta(t'')]\right\rangle_m^{\mathrm{SP}} = \frac{c^2}{F_m^{\mathrm{SP}}(\mathbf{s},\hat{\mathbf{z}},t)}$$
$$\times\left\{\left[\int_0^t dt' \int_0^{t'} dt'' \int ds' \int ds''\, \mathbf{F}^{\mathrm{SP}}(\mathbf{s},\mathbf{s}',t-t')s'_\alpha \mathbf{F}^{\mathrm{SP}}(\mathbf{s}',\mathbf{s}'',t'-t'')s''_\beta \mathbf{F}^{\mathrm{SP}}(\mathbf{s}'',\hat{\mathbf{z}},t'')\mathbf{I}^{\mathrm{SP}(0)}\right]_m + (\text{t.c.})\right\}, \quad (26)$$

where (t.c.) means that the second term is obtained by exchanging the indices α and β in the first term. As discussed at end of last section, Eqs. (25) and (26) provide exact expressions for evaluation of the first and the second moments.

In evaluation of Eqs. (25) and (26), it is convenient to use the components of s in a spherical harmonic basis:

$$\mathbf{s}=[s_1,s_0,s_{-1}]$$
$$=[-2^{-1/2}\sin\theta e^{+i\phi},\cos\theta,+2^{-1/2}\sin\theta e^{-i\phi}], \quad (27)$$

and first calculate the corresponding quantities in the CP. Hence we write Eq. (25) as

$$\langle R_\alpha\rangle_m^{\mathrm{SP}} = \frac{1}{F_m^{\mathrm{SP}}(\mathbf{s},\hat{\mathbf{z}},t)}\left[\sum_j U_{\alpha j}\mathbf{T}^{-1}\langle R_j\rangle \mathbf{T}\mathbf{I}^{\mathrm{SP}(0)}\right]_m, \quad (28)$$

with $\alpha=x,y,z$ and $j=1,0,-1$, the indices of the spherical harmonic basis. U is a matrix for the transform from a spherical harmonic basis to a Cartesian basis, $s_\alpha = U_{\alpha j}s_j$, given by

$$U=\begin{bmatrix} -2^{-1/2} & 0 & 2^{-1/2} \\ 2^{-1/2}i & 0 & 2^{-1/2}i \\ 0 & 1 & 0 \end{bmatrix}. \quad (29)$$

$\langle\mathbf{R}\rangle$ in Eq. (28) is defined in the CP as

$$\langle R_j\rangle_{mn_0} \equiv c\int_0^t dt' \int ds' \sum_n F_{mn}(\mathbf{s},\mathbf{s}',t-t')s'_j F_{mn_0}(\mathbf{s}',\hat{\mathbf{z}},t'), \quad (30)$$

where $F_{mn}(\mathbf{s}_2,\mathbf{s}_1,t_2-t_1)$ is the exact angular Green's function in the CP, Eq. (12). Similarly, Eq. (26) is written as

$$\langle R_\alpha R_\beta\rangle_m^{\mathrm{SP}} = \frac{1}{F_m^{\mathrm{SP}}(\mathbf{s},\hat{\mathbf{z}},t)}\left[\sum_{j_1}\sum_{j_2}(U_{\alpha j_1}U_{\beta j_2} + U_{\alpha j_2}U_{\beta j_1})\mathbf{T}^{-1}\langle \mathbf{R}_{j_2}\mathbf{R}_{j_1}\rangle \mathbf{T}\mathbf{I}^{\mathrm{SP}(0)}\right]_m, \quad (31)$$

where $\langle \mathbf{R}_{j_2}\mathbf{R}_{j_1}\rangle$ is defined in the CP as

$$\langle R_{j_2}R_{j_1}\rangle_{mn_0} \equiv c^2\int_0^t dt' \int_0^{t'} dt'' \int ds' \int ds''$$
$$\times\sum_{n_2} F_{mn_2}(\mathbf{s},\mathbf{s}',t-t')s'_{j_2}$$
$$\times\sum_{n_1} F_{n_2n_1}(\mathbf{s}',\mathbf{s}'',t'-t'')s''_{j_1}F_{n_1n_0}(\mathbf{s}'',\hat{\mathbf{z}},t''), \quad (32)$$

where j_1 and j_2 are spherical components, 1, 0, -1.

In the evaluation of Eqs. (30) and (32), a recurrence relation of GSP's is used, which is directly derived from angular momentum theory [10]. Defining $s_j=\mu_j e^{ij\phi}$, with $j=1,0,-1$, we have

$$\mu_j P^l_{m,n}(\cos\theta) = \gamma_j \sum_h \langle l,1,m,0|l+h,m\rangle$$
$$\times\langle l,1,n,\pm j|l+h,n\pm j\rangle P^{l+h}_{m,n\pm j}(\cos\theta),$$
$$j,h=+1,0,-1, \quad (33)$$

with $\gamma_{\mp 1}=\mp i$ and $\gamma_0=1$, and $\langle l_1,l_2,m_1,m_2|L,M\rangle$ are the Clebsch-Gordan coefficients in angular momentum theory [10], given by

$$\langle l-h,1,m,-j|l,m-j\rangle = \begin{bmatrix} \left[\frac{(l-m)(l-m+1)}{(2l-1)2l}\right]^{1/2} & \left[\frac{(l+m)(l-m+1)}{2l(l+1)}\right]^{1/2} & \left[\frac{(l+m)(l+m+1)}{(2l+2)(2l+3)}\right]^{1/2} \\ \left[\frac{(l-m)(l+m)}{(2l-1)l}\right]^{1/2} & \left[\frac{m^2}{l(l+1)}\right]^{1/2} & -\left[\frac{(l+m+1)(l-m+1)}{(l+1)(2l+3)}\right]^{1/2} \\ \left[\frac{(l+m)(l+m+1)}{(2l-1)2l}\right]^{1/2} & -\left[\frac{(l-m)(l+m+1)}{2l(l+1)}\right]^{1/2} & \left[\frac{(l-m)(l-m+1)}{(2l+2)(2l+3)}\right]^{1/2} \end{bmatrix}, \quad (34)$$

with the row index (from above) $j=1,0,-1$ and the column index (from left) $h=1,0,-1$. These recurrence relations of GSF's

were provided in Ref. [8] with some misprints. Substituting Eqs. (12) and (13) into Eq. (30), and using Eq. (33) and the orthogonality relation of GSF's, Eq. (8), integrations over $d\mathbf{s}'$ and dt' in Eq. (30) can be analytically performed. When the final direction $\mathbf{s}=(\theta,\phi)$, we have

$$\langle R_j\rangle_{mn_0}=c\sum_l P^l_{m,n_0-j}(\cos\theta)e^{-i(n_0-j)\phi}\gamma_j \times\sum_n\sum_h\frac{2(l-h)+1}{4\pi}D^{l,h}_{m,n,n_0}(t)\langle l-h,1,n,0|l,n\rangle\langle l-h,1,n_0,-j|l,n_0-j\rangle, \tag{35}$$

with $n=2,0,-0,-2$, $h=+1,0,-1$ and

$$D^{l,h}_{m,n,n_0}(t)=\sum_{ij}[B^l_{mn}]_i[B^{l-h}_{nn_0}]_j\left[\frac{\exp(-\lambda_j^{l-h}t)-\exp(-\lambda_i^l t)}{\lambda_i^l-\lambda_j^{l-h}}\right]\exp(-\mu_a t),\quad i,j=1,2,3,4. \tag{36}$$

Similarly, integrations in Eq. (32) can also be analytically performed. We have

$$\langle R_{j_2}R_{j_1}\rangle_{mn_0}=c^2\sum_l P^l_{m,n_0-j_2-j_1}(\cos\theta)e^{-i(n_0-j_2-j_1)\phi}\gamma_{j_2}\gamma_{j_1}\sum_{n_2}\sum_{n_1}\sum_{h_2}\sum_{h_1}\frac{2(l-h_2-h_1)+1}{4\pi} \times E^{l,h_2,h_1}_{m,n_2,n_1,n_0}(t)\langle l-h_2,1,n_2,0|l,n_2\rangle\langle l-h_2,1,n_0-j_1,-j_2|l,n_0-j_1-j_2\rangle \times\langle l-h_2-h_1,1,n_1,0|l-h_2,n_1\rangle\langle l-h_2-h_1,1,n_0,-j_1|l-h_2,n_0-j_1\rangle, \tag{37}$$

with n_1, $n_2=2,0,-0,-2$, $h_1,h_2=+1,0,-1$, and

$$E^{l,h_2,h_1}_{m,n_2,n_1,n_0}(t)=\sum_{ijf}[B^l_{mn_2}]_i[B^{l-h_2}_{n_2n_1}]_j[B^{l-h_2-h_1}_{n_1n_0}]_f \times\left[\frac{\exp(-\lambda_f^{l-h_2-h_1}t)-\exp(-\lambda_i^l t)}{(\lambda_j^{l-h_2}-\lambda_f^{l-h_2-h_1})(\lambda_i^l-\lambda_f^{l-h_2-h_1})}-\frac{\exp(-\lambda_j^{l-h_2}t)-\exp(-\lambda_i^l t)}{(\lambda_j^{l-h_2}-\lambda_f^{l-h_2-h_1})(\lambda_i^l-\lambda_j^{l-h_2})}\right]\exp(-\mu_a t). \tag{38}$$

Up to now, algebraic analytical expressions for the first cumulant (the average center of the distribution) and the second cumulant (the half-width of spread) have been derived. Equations (36) and (38) involve the related scattering parameters: μ_s and Π^l_{mn} [defined after Eq. (14)], through λ^l_i in Eq. (16) and $[B^l_{mn_0}]_i$ in Appendix A, and the absorption parameter, μ_a. Thus they determine the time evolution dynamics. The final light direction $\mathbf{s}$ appears as an argument of the generalized spherical harmonics in Eqs. (35) and (37). Substituting Eqs. (18), (35), and (37) into Eqs. (28), (31), and then Eq. (24), the first and second cumulants in the SP representation are obtained as functions of $\mathbf{s}$ and t. The distribution function of polarized light is then expressed by Eq. (23), with Eq. (28) for the average center position and Eq. (24) for the width of the spread. Equation (23) produces the mth Stokes component of polarized light at position $\mathbf{r}$, with light direction $\mathbf{s}$, as a function of time t, initialed by $\mathbf{r}_0=0$, $\mathbf{s}_0=\hat{\mathbf{z}}$, and polarized state $\mathbf{I}^{\mathrm{SP}(0)}$ in an infinite uniform medium.

It is easy to reduce the above solution to the scalar (unpolarized) case by considering only the I_0 component. Because $\langle l,1,0,0|l,0\rangle=0$ in Eq. (34), Eqs. (35) and (37) can be greatly simplified. Also, Eq. (15) is reduced to $(2l+1)\exp(-\Pi^l_{00}t)/4\pi$ in the scalar case. Notice that the associated Legendre function $P^{(m)}_l(\mu)=(i)^m[(l+m)!/(l-m)!]^{1/2}P^l_{0,m}(\mu)$; our formula reduces to that given in Ref. [14] in the scalar case.

V. DISTRIBUTION FUNCTION ACCURATE UP TO AN ARBITRARY HIGH-ORDER CUMULANT

In order to calculate the polarized photon distribution function with accuracy up to an arbitrary high order, it is more convenient to set all spatial and angular vectors in the spherical harmonics basis, similar to Eq. (27), and to evaluate Eq. (22) via the CP:

$$\left[\left\langle\int_0^t dt_k\cdots\int_0^t dt_1\,T[s_{j_k}(t_k)\cdots s_{j_1}(t_1)]\right\rangle\right]^{\mathrm{SP}}_m =\frac{1}{F^{\mathrm{SP}}_m(\mathbf{s},\mathbf{s}_0,t)}[\mathbf{T}^{-1}\mathbf{G}(j_k,\ldots,j_1,t)\mathbf{T}\mathbf{I}^{\mathrm{SP}(0)}]_m, \tag{39}$$

with $j_1,\ldots,j_k=1,0,-1$ and $\mathbf{G}(j_k,\ldots,j_1,t)$ given by

$$\mathbf{G}(j_k,\ldots,j_1,t)=\left\{\int_0^t dt_k\int_0^{t_k}dt_{k-1}\cdots\int_0^{t_2}dt_1\int d\mathbf{s}^{(k)}\int d\mathbf{s}^{(k-1)}\cdots\int d\mathbf{s}^{(1)}\right.$$
$$\left.\times\mathbf{F}(\mathbf{s},\mathbf{s}^{(k)},t-t_k)s_{j_k}^{(k)}\mathbf{F}(\mathbf{s}^{(k)},\mathbf{s}^{(k-1)},t_k-t_{k-1})s_{j_{k-1}}^{(k-1)}\cdots\mathbf{F}(\mathbf{s}^{(2)},\mathbf{s}^{(1)},t_2-t_1)s_{j_1}^{(1)}\mathbf{F}(\mathbf{s}^{(1)},\mathbf{s}_0,t_1-0)+\text{perm.}\right\},\tag{40}$$

where $F_{mn}(\mathbf{s}^{(i)},\mathbf{s}^{(i-1)},t_i-t_{i-1})$ is given by Eq. (12). Using the GSF recurrence relation, Eq. (33), and the orthogonality relation of GSF's, Eq. (8), the integrals over $d\mathbf{s}^{(k)}\cdots d\mathbf{s}^{(1)}$ in Eq. (40) can be analytically performed. We obtain, when the initial $\mathbf{s}_0$ is along $\mathbf{z}$ and the final $\mathbf{s}=(\theta,\phi)$, that

$$[G(j_k,\ldots,j_1,t)]_{mn_0}=\left\{\sum_l P^l_{m,n_0-\Sigma_{f=1}^k j_f}(\cos\theta)\exp\left[-i\left(n_0-\sum_{f=1}^k j_f\right)\phi\right]\left[\prod_{f=1}^k\gamma_{j_f}\right]\sum_{n_k}\cdots\sum_{n_1}\sum_{h_k}\cdots\sum_{h_1}\frac{2(l-\Sigma_{f=1}^k h_f)+1}{4\pi}\right.$$
$$\times H^{l,h_k,\ldots,h_1}_{mn_k,\ldots,n_1n_0}(t)\prod_{g=1}^k\left\langle l-\sum_{f=1}^g h_{k-f+1},1,n_{k-g+1},0\middle|l-\sum_{f=1}^{g-1}h_{k-f+1},n_{k-g+1}\right\rangle$$
$$\left.\times\left\langle l-\sum_{f=1}^g h_{k-f+1},1,n_0-\sum_{f=1}^{k-g}j_f,-j_{k-g+1}\middle|l-\sum_{f=1}^{g-1}h_{k-f+1},n_0-\sum_{f=1}^{k-g+1}j_f\right\rangle\right\}+\text{perm},\tag{41}$$

with $n_f=2,0,-0,-2$ and $h_f=1,0,-1$, $f=1,2,\ldots,k$, with

$$H^{l,h_k,\ldots,h_1}_{mn_k,\ldots,n_1n_0}(t)=\exp(-\mu_a t)\sum_{i_{k+1}=1}^4\cdots\sum_{i_1=1}^4[B^l_{mn_k}]_{i_{k+1}}[B^{l-h_k}_{n_kn_{k-1}}]_{i_k}\cdots[B^{l-\Sigma_{f=1}^k h_{k-f+1}}_{n_1n_0}]_{i_1}$$
$$\times\int_0^t dt_k\int_0^{t_k}dt_{k-1}\cdots\int_0^{t_2}dt_1\exp[-\lambda^l_{i_{k+1}}(t-t_k)]\exp[-\lambda^{l-h_k}_{i_k}(t_k-t_{k-1})]\cdots\exp[-\lambda^{l-\Sigma_{f=1}^k h_{k-f+1}}_{i_1}(t_1-0)].\tag{42}$$

Note that all ensemble averages have been performed. Equation (42) involves integrals of exponential functions, which can be analytically performed. An explicit expression for evaluating integrals in Eq. (42) is presented in the Appendix B. Equation (42) involves all related scattering and absorption parameters and determines the time evolution dynamics. The final direction of light, $\mathbf{s}$, appears as an argument of GSF's in Eq. (41). Substituting Eq. (42) into Eq. (41), through Eq. (39), which transfers to the SP representation and introduces the initial polarized condition, and using a standard cumulant procedure, the cumulants as functions of angle $\mathbf{s}$ and time t up to an arbitrary kth order in the SP representation can be recursively obtained. The final position $\mathbf{r}$ appears in Eq. (20), and its components can be expressed on a spherical harmonics basis, similar to Eq. (27). Then, performing a numerical three-dimensional inverse Fourier transform over $\mathbf{q}$, an approximate distribution function $I_m^{\mathrm{SP}}(\mathbf{r},\mathbf{s},t)$ in the SP representation, accurate up to kth cumulant, can be calculated.

VI. DISCUSSION

In Sec. III, we derived an explicit expression of the polarized photon distribution function, which guarantees the exact average central position (the first cumulant) and the exact width of spread (the second cumulant). Moreover, with an increase of collision events or time, the distribution approaches accuracy in detail since the higher cumulants become relatively small compared to the appropriate power of the second cumulant. If we examine the spatial displacement after each collision event as an independent random variable $\Delta\mathbf{r}_i$, the total displacement is $\Sigma\Delta\mathbf{r}_i$ $(i=1,\ldots,N)$, with N the number collision events, which can be estimated by t/μ_s. If we define $\mathbf{Y}=(N)^{-1/2}\Sigma\Delta\mathbf{r}_i$, the central limit theorem claims that if N is a large number, then $\langle\mathbf{Y}^n\rangle_c/\langle\mathbf{Y}^2\rangle_c\sim N^{1-n/2}$, $n\geq 3$. Therefore, the sum of N variables will have an essentially Gaussian distribution. At early times, the photon's spread is narrow: hence, in many applications the detailed shape is less important than the correct position and correct narrow width of the beam, because of the finite resolution of detection devices. In case a more accurate distribution at early times is needed, Sec. IV provides formulas for analytically calculating the higher cumulants up to an arbitrary kth order. Then, performing a numerical three-dimensional Fourier transform, the distribution function accurate up to the kth order cumulant approximation can be obtained.

In summary, we present an analytical solution of the time-dependent polarized radiative transport equation in an infinite uniform isotropic medium. The Green's function for the angular part is exact. Using a cumulant expansion, we can analytically calculate the spatial cumulants up to an arbitrary

high order. By terminating at the second order, we have derived an explicit expression of the polarized light distribution function. This expression is quantitatively accurate up to the second order cumulant approximation. Namely, the center position and the half-width are always exact and not modified when higher-order cumulants are added. The central limit theorem claims that after enough collision events, all cumulants higher than second approach small values, and the Gaussian spatial distribution calculated approaches accuracy in detail. Our results are given in terms of a distribution with coefficients that can be calculated algebraically, with moderate effort at the second cumulant level and additional effort to induce the third- and higher-order cumulants. This analytical solution provides a background distribution function for further study of optical tomography using polarized light.

ACKNOWLEDGMENTS

This work was supported in part by NASA, DOE, USAMRMC, and the New York State Science and Technology Foundation.

APPENDIX A

In this appendix we calculate $[B^l_{mn_0}]_i$ in Eq. (15). Substituting Eq. (15) into Eq. (14), we obtain a set of linear homogeneous equations

$$\sum_n [\Pi^l_{mn}-\lambda^l_i\delta_{m,n}][B^l_{nn_0}]_i=0, \tag{A1}$$

where eigenvalues λ^l_i $(i=1,2,3,4)$ are given by Eq. (16). These equations, however, are not linearly independent. Adding the initial condition, Eq. (14b), given by

$$\sum_i [B^l_{mn_0}]_i=\delta_{m,n_0}, \tag{A2}$$

the unique solution of $[B^l_{mn_0}]_i$ then can be obtained. For given n_0 and l, 16 components of $[B^l_{mn_0}]_i$ construct a column vector in the space of the direct product of $i\times m$. Combining Eqs. (A1) and (A2) in $i\times m$ space, we obtain the following matrix equation:

$$\mathbf{AB}=\mathbf{C}. \tag{A3}$$

A is a 16×16 matrix:

$$A_{i\times m,j\times n}=[\Pi^l_{mn}\delta_{i,j}-\lambda^l_i\delta_{i,j}\delta_{m,n}+\delta_{m,n}]. \tag{A4}$$

B and **C** are 16×1 column vectors: $B_{j\times n}=[B^l_{nn_0}]_j$ and $C_{i\times m}=\delta_{m,n_0}$. Here **A** and **C** are given, while **B** is unknown. Equation (A3) is a standard form of a group of 16 linear equations. The solution is given by

$$B_{i\times m}=\Delta_{i\times m}/\det(\mathbf{A}), \tag{A5}$$

with $\Delta_{i\times m}$ is obtained by replacing the $(i\times m)$th column in the determinant of **A** by the column vector **C**.

APPENDIX B

In this appendix, we derive an analytical expression for Eq. (42) to kth order. By defining

$$b_g\equiv\lambda^{[l-\Sigma_{f=1}^{k-g}h_{k-f+1}]}_{i_{g+1}}-\lambda^{[l-\Sigma_{f=1}^{k-g+1}h_{k-f+1}]}_{i_g},\quad g=1,\ldots,k, \tag{B1}$$

Eq. (42) can be written as

$$H^{l,h_k,\ldots,h_1}_{mn_k\ldots,n_1n_0}(t)=\exp(-\mu_a t)\sum_{i_{k+1}=1}^{4}\cdots\sum_{i_1=1}^{4}[B^l_{mn_k}]_{i_{k+1}}[B^{l-h_k}_{n_kn_{k-1}}]_{i_k}\cdots[B^{l-\Sigma_{f=1}^{k}h_{k-f+1}}_{n_1n_0}]_{i_1}\exp(-\lambda^l_{i_{k+1}}t)F^{(k)}(t), \tag{B2}$$

with

$$F^{(k)}(t)=\int_0^t dt_k\,e^{b_kt_k}\int_0^{t_k}dt_{k-1}\,e^{b_{k-1}t_{k-1}}\cdots\int_0^{t_2}dt_1\,e^{b_1t_1}. \tag{B3}$$

It is easy to directly calculate Eq. (B3) for a few low k orders:

$$F^{(1)}(t)=\frac{e^{b_1t}}{b_1}-\frac{1}{b_1}, \tag{B4a}$$

$$F^{(2)}(t)=\frac{e^{(b_1+b_2)t}}{b_1(b_1+b_2)}-\frac{e^{b_2t}}{b_1b_2}+\frac{1}{(b_1+b_2)b_2}, \tag{B4b}$$

$$F^{(3)}(t)=\frac{e^{(b_1+b_2+b_3)t}}{b_1(b_1+b_2)(b_1+b_2+b_3)}-\frac{e^{(b_2+b_3)t}}{b_1b_2(b_2+b_3)}+\frac{e^{b_3t}}{(b_1+b_2)b_2b_3}-\frac{1}{(b_1+b_2+b_3)(b_2+b_3)b_3}. \tag{B4c}$$

In each step of integration, the difficulty is in determining the constant term. In the following we prove that this term is

given by $(-1)^k/[b_k(b_k+b_{k-1})\cdots(b_k+b_{k-1}+\cdots+b_1)]$. Equation (B3) can be written as

$$F^{(k)}(t)=\int_0^t dt'\, e^{b_k t'} F^{k-1}(t'). \tag{B5}$$

Using integration by parts to Eq. (B5), we obtain

$$F^{(k)}(t)=\frac{1}{b_k}\left[e^{b_k t}F^{(k-1)}(t)-\int_0^t dt'\, e^{(b_k+b_{k-1})t'}F^{(k-2)}(t')\right]. \tag{B6}$$

Recursively applying Eq. (B6), we obtain

$$\begin{aligned}F^{(k)}(t)=&\frac{e^{b_k t}}{b_k}F^{(k-1)}(t)-\frac{e^{(b_k+b_{k-1})t}}{b_k(b_k+b_{k-1})}F^{(k-2)}(t)\\&+\cdots+(-1)^f\frac{e^{(b_k+b_{k-1}+\cdots+b_{k-f})t}}{b_k(b_k+b_{k-1})\cdots(b_k+b_{k-1}+\cdots+b_{k-f})}F^{k-f-1}(t)\\&+\cdots+(-1)^{k-1}\frac{e^{(b_k+b_{k-1}+\cdots+b_1)t}-1}{b_k(b_k+b_{k-1})\cdots(b_k+b_{k-1}+\cdots+b_1)}.\end{aligned} \tag{B7}$$

Equation (B7) provides a formula to recursively evaluate Eq. (40) up to kth order. Also, Eq. (B7) produces the above-mentioned constant term. An explicit expression of Eq. (42) can then be written as

$$\begin{aligned}H^{1,h_k,\ldots,h_1}_{mn_k,\ldots,n_1n_0}(t)=&\exp(-\mu_a t)\sum_{i_{k+1}=1}^{4}\cdots\sum_{i_1=1}^{4}[B^{l}_{mn_k}]_{i_{k+1}}[B^{l-h_k}_{n_kn_{k-1}}]_{i_k}\cdots[B^{l-\Sigma_{g=1}^{k}h_{k-g+1}}_{n_1n_0}]_{i_1}\\&\times\exp(-\lambda^{l}_{i_{k+1}}t)\sum_{g=0}^{k}\frac{(-1)^g\exp[\Sigma_{f=0}^{k-g}b_{k-f+1}t]}{\Pi_{j=1}^{k}L_j^{(g)}},\end{aligned} \tag{B8}$$

with $b_{k+1}\equiv 0$, and

$$L_j^{(g)}=\sum_{f=j}^{g}b_f,\quad j\leq g,\quad \text{or}\quad L_j^{(g)}=\sum_{f=g+1}^{j}b_f,\quad j>g, \tag{B9}$$

where b_g is defined in Eq. (B1).

[1] R. Gans, Ann. Phys. (Leipzig) **75**, 1 (1925).
[2] S. Chandrasekhar, *Radiative Transfer* (Clarendon, Oxford, 1950).
[3] S. G. Demos and R. R. Alfano, Appl. Opt. **36**, 150 (1997); Opt. Lett. **21**, 161 (1996).
[4] A. H. Hielscher, A. A. Eick, J. R. Mourant, and I. J. Bigio, Appl. Opt. **26**, 125 (1997).
[5] B. D. Cameron, M. J. Rakovic, M. Mehrubeoglu, G. Kattawar, S. Rastegar, L. V. Wang, and G. Cote, Opt. Lett. **23**, 485 (1998).
[6] S. R. Pal and A. I. Carswell, Appl. Opt. **24**, 3464 (1985).
[7] I. Kuščer and M. Ribarič, Opt. Acta **6**, 42 (1959).
[8] I. M. Gel'fand and Z. Ya. Sapiro, Am. Math. Soc. Trans. **2**, 207 (1956).
[9] J. W. Hovenier and C. V. M. van der Mee, Astron. Astrophys. **128**, 1 (1983).
[10] B. M. Brink and G. M. Satchler, *Angular Momentum* (Clarendon, Oxford, 1962).
[11] M. Herman and J. Lenoble, J. Quant. Spectrosc. Radiat. Transf. **8**, 355 (1968).
[12] H. Domke, J. Quant. Spectrosc. Radiat. Transf. **15**, 669 (1975); **15**, 681 (1975); **16**, 973 (1976).
[13] A. Ambirajan and D. C. Look, J. Quant. Spectrosc. Radiat. Transf. **58**, 171 (1997).
[14] W. Cai, M. Lax, and R. R. Alfano, Phys. Rev. E **61**, 3871 (2000).
[15] W. Cai, M. Lax, and R. R. Alfano, J. Phys. Chem. B **104**, 3996 (2000).
[16] G. C. Stokes, Trans. Cambridge Philos. Soc. **9**, 399 (1852).
[17] H. C. van de Hulst, *Light Scattering by Small Particles* (Wiley, New York, 1957), pp. 40–59.
[18] W. A. De Rooij and C. C. A. H. van der Stap, Astron. Astrophys. **131**, 237 (1984).
[19] S. H. Ma, *Statistical Mechanics* (World Scientific, Philadelphia, 1985).
[20] R. P. Feynman, Phys. Rev. **84**, 108 (1951); F. Dyson, *ibid.* **75**, 486 (1949).
[21] M. G. Kendall and A. Stuart, *The Advanced Theory of Statistics* 3rd ed. (Hafner, New York, 1969), Vol. I.

Appendix 3

Cumulant Approximation of the Radiative Transfer Equation for Photon Density in Semi – infinite and Slab Geometries

A. V. Carpenter, W. Cai, M. Lax, and R. R. Alfano

Institute for Ultrafast Spectroscopy and Lasers
New York State Center of Advanced Technology for Ultrafast Photonic Materials and Applications
and
Departments of Electrical Engineering and Physics
The City College of New York
and
The Graduate Center of the City University of New York
New York, NY 10031

Abstract

The cumulant analytical solution of the Boltzmann radiative transfer is extended for semi–infinite and slab geometries to provide a more accurate picture for the transition time from the ballistic to the diffusive regime. For the scattering structures, the method of adding image sources used in the conventional diffusion approximation for boundary-based media is modified and applied to the cumulant transport model. Numerical comparisons between the cumulant model and the standard and the center-moved diffusion models are presented. The cumulant model, which reduces to the center-moved diffusion model at later times, gives a better prediction of photon migration at early times than the other models. This work is useful for photon migration in several applications: human tissues, clouds, fog, and seawater. Our calculations were specifically aimed at clouds and optical wireless communications.

OCIS codes: (030.5620) radiative transfer, (290.1990) diffusion, (290.7050) turbid media, and (170.5280) photon migration, (010.1310) atmospspheric scattering.

Submitted to: *Journal of the Optical Society of America A*

IUSL # - 2001 -05

I. Introduction

Understanding time-dependent photon migration is important for numerous light-based applications in medical, military, space, and atmospheric fields.[1-4] When a light pulse enters a scattering medium, it divides into ballistic, snake-like, and diffusive components.[17] The ballistic component describes photons that travel virtually undistributed through the scattering medium. The snake-like photons endure only a few scattering events and have only slight deviations from a straight-line path through the media. The diffuse component, which dominants at later times, represents photons that have undergone multiple scattering events.

The Boltzmann radiative transfer equation describes the photon migration through a scattering medium. Due to its difficulty in obtaining a solution, scientists utilize approximations; in particular, the standard diffusion approximation is used to describe the transport of photons. This approximation is based on the assumption that photons are isotropically diffuse from a fixed source with a constant diffusion coefficient in a uniform medium. This is not the case as shown by Zevallos.[18] The diffusion approximation is valid only when the propagation distance is much greater than the transport mean free path, l_t, such as $L > 6l_t$, where L is the distance from the source to the detector.[5] The diffusion approximation cannot accurately determine the distribution of early-arriving photons or when the source-detector distance is small. One suggested model for bypassing the distance issue is to allow the photons to be diffused from an initial point located one transport mean length from the source position along the incident direction.[6] This is referred to as the center-moved diffusion approximation. While the center-moved approximation results are better than the standard approximation at later times, the migration of the early photons cannot correctly be described because photon movement before $1l_t$ is neglected. Other

models, such as the non-Euclidean diffusion model, have been introduced to bridge the gap between the nondiffusive and diffusive regime with limited success.[7]

Most recently, cumulant analytical expressions for the photon distribution function and the photon density as solutions to the Boltzmann radiative transfer equation have been derived by Cai and co-workers for an infinite uniform medium.[8, 9] In the infinite environment, the cumulant approximation displays an accurate picture of the photon propagation in the early time or nondiffusive regimes. For most practical applications, the photons propagate through a limited region as oppose to an infinite one. The effects of a boundary need to be considered.

In this paper, the cumulant analytical expressions are extended to describe photon migration in structures of semi-infinite and slab geometries. We focus on photons traveling in clouds with $l_t = 100m$. Previously, the standard and center-moved diffusion approximations have been used to study photon migration in the semi-infinite and slab media with various boundary conditions.[10, 11] The results from the cumulant transport approximation were compared with the outcome from the diffusion approximations. In contrast to the diffusion approximation, the cumulant expressions give a more accurate picture of the photon migration, including the ballistic and snake-like phases. The boundary effects are viewed through amplitude and decay pattern variations in the time-resolved profile as the distance from the source increases. At longer times, the cumulant results approach those of the center-moved diffusion approximation. Our work will be important for imaging and propagation of optical coded information through clouds in optical wireless systems.

II. Photon density in an infinite, uniform medium

This section describes the cumulant solution for an infinite uniform medium. The photon distribution function, $I(\vec{r},\vec{s},t)$, or the photon density function, $N(\vec{r},t)$, which is defined as $N(\vec{r},t)=\int d\vec{s}\, I(\vec{r},\vec{s},t)$, can be used to describe the temporal and spatial profiles of scattered photons inside a turbid medium. For an infinite uniform medium with a short pulse originating from a point source located at $\vec{r}=0$, the temporal profile of the photon density at position $\vec{r}$ from the source for the standard diffusion model (sDM) and the center-moved diffusion model (cmDM) is given by

$$N(\vec{r},t)=N_R(\vec{r},t)=\frac{1}{(4\pi Dct)^{3/2}}\exp\left[-\frac{(\vec{r}-l_m\vec{s}_o)^2}{4Dct}\right]\cdot\exp[-\mu_a t] \qquad (1)$$

with $l_m=0$ for sDM and $l_m=l_t$ for cmDM, where, $\vec{s}_o$ is the unit vector for the incident direction, D is the diffusion coefficient and is given by $<D=1/3[(1-g)\mu_s]>$, g is the anisotropy factor or mean cosine of the scattering angle, μ_a is the absorption rate $(n\sec^{-1})$, μ_s is the scattering rate $(n\sec^{-1})$, and c is the speed of light ($m/n\sec$).

The photon distribution function and the photon density in an infinite, uniform medium have been derived by Cai et al using an analytical solution of the radiative transport equation using cumulant expansion. [8, 9] A Gaussian distribution with the exact first-order cumulant, which provides the average center of the distribution, and the exact second-order cumulant, which provides the time-dependent diffusion coefficients, presents a more accurate picture of the photon migration, especially at early times.[19] Photon migration is viewed as a photon cloud spreading anisotropically from a moving center with a time-dependent diffusion coefficient.

Based on the cumulant expansion,[14, 15] the photon density, $N(\vec{r},t)$, in an infinite, uniform medium with the source located at $\vec{r}_s = 0$ and an incident direction along $\vec{s}_0 = \hat{z}$ is given by

$$N(\vec{r},t) = \frac{1}{(4\pi D_{zz}ct)^{1/2}} \frac{1}{4\pi D_{xx}ct} \exp\left[-\frac{(z-R_z)^2}{4D_{zz}ct}\right] \exp\left[-\frac{(x^2+y^2)}{4D_{xx}ct}\right] \exp(-\mu_a t) \quad (2)$$

where, the moving center of the photon, R_z, is given by

$$R_z = c\frac{1-\exp(-g_1 t)}{g_1} \quad . \quad (3)$$

The time-dependent diffusion coefficients are

$$D_{zz} = \frac{c}{3t}\left\{\frac{t}{g_1} + \frac{3g_1 - g_2}{g_1^{\,2}(g_1 - g_2)}[1-\exp(-g_1 t)] + \frac{2}{g_2(g_1 - g_2)}[1-\exp(-g_2 t)] - \frac{3}{2g_1^{\,2}}[1-\exp(-g_1 t)]^2\right\} \quad (4)$$

$$D_{xx} = D_{yy} = \frac{c}{3t}\left\{\frac{t}{g_1} + \frac{g_2}{g_1^{\,2}(g_1 - g_2)}[1-\exp(-g_1 t)] + \frac{1}{g_2(g_1 - g_2)}[1-\exp(-g_2 t)]\right\} \quad . \quad (5)$$

These equations are independent of absorption. They show time is real and time to build up the diffusion coefficient.

The coefficient g_l is defined as

$$g_l = \mu_s\left[1 - \frac{a_l}{(2l+1)}\right] \quad (6)$$

where, a_l is the Legendre coefficient of the phase function, $P(\cos\theta)$, which is given by $P(\cos\theta) = (1/4\pi)\sum_l a_l \mathrm{P}_l(\cos\theta)$ and $\cos\theta = \vec{s}\cdot\vec{s}_0$. Two special values for g_l are $g_0 = 0$, which

follows from the normalization of the phase function and $g_1 = c/l_t$, where the transport mean free path is defined as $l_t = c/\left|\mu_s\left(1-\overline{\cos\theta}\right)\right|$ with anisotropy factor $\overline{\cos\theta}$.

Our analysis focuses on clouds as the test media. Figure 1 shows the normalized moving center $\left(R_z/l_t\right)$ and normalized diffusion coefficients (D_{xx}/l_t and D_{zz}/l_t) for a cloud of water droplets with a refractive index of 1.33 uniformly distributed in air with the droplet's radius equal to the incident light's wavelength. From Mie's theory for light scattering, g_1 and g_2 are $\sim 0.16\,\mu_s$ and $\sim 0.27\,\mu_s$, respectively.

Near time $t = 0$, the diffusion coefficients $\left(D_{xx}, D_{zz}\right)$ are approximately equal to zero and the moving center is moving at the speed of light. This corresponds to the ballistic stage for the photon. As time increases, the moving center slows and the diffusion coefficient increases from zero. This region represents the snake-like phase of photon migration. In the diffusive regime, the moving center stops at $1l_t$, while the diffusion coefficients approach $l_t/3$.

The two diffusion models have the fixed values for R_z/l_t at all times ($R_z/l_t = 0$ for the sDM and $R_z/l_t = 1$ for the cmDM) and a fixed diffusion coefficient, $D = l_t/3$, as indicated in Figure 1. The results from our model approach the cmDM results at later times, while giving a more precise view at early times.

Based on the cumulant analytical expressions, we developed the cumulant transport model (cTM) for structures. We first examine the difference between the cTM and the diffusion models by computing the temporal profiles for the photon density for each model using the infinite geometry as a point of reference. For all three models, the scattering parameters are the same as that for Figure 1.

As displayed in Figure 2a, the photon density peak for an infinite medium occurs sooner for both the sDM and cmDM than for the cTM with a source-detector separation, $z_{sd_0} = 2l_t$. For the cmDM, the peak arrives much faster than the speed of light. This occurs because of the initial placement of the source one l_t inside the medium. The peak from the cTM is much stronger than that of the sDM due to the exact cumulants used in our model. Decreasing z_{sd_0} below $2l_t$ yields unrealistic peaks for both the sDM and cmDM. For the cTM, the long turn-on time for the photon density is consistent with the concept that no light arrives before the ballistic time. As z_{sd_0} is increased, as shown in Figure 2b with $z_{sd_0} = 7l_t$, the peaks from the cTM and cmDM become similar in intensity with the cTM still displaying a longer turn-on time than the cmDM. As shown in Figure 2c for $z_{sd_0} = 10l_t$, once we are outside of the limits for diffusion approximation $\left(z_{sd_0} > 7l_t\right)$, no discernible differences exist between the cTM and the cmDM.

III. Photon density in uniform, semi-infinite and slab media

In this section, we extend the cumulant solution for an infinite uniform medium to that in semi-infinite and slab uniform media with vacuum (or completely absorbing) boundaries. A previously used approximate approach for extending to a semi-infinite medium is to place an image source above the surface to offset the real source.[10, 11] This image source creates a boundary condition $N(\vec{r},t)\big|_B = 0$ at the extrapolated boundary **B :** at a distance, z_e outside the medium. The approximate value of z_e is given by[10]

$$z_e = \frac{2}{3}\left(\frac{1+r_e}{1-r_e}\right)l_t. \tag{7}$$

where, r_e is the effective reflection coefficient at the physical boundary. In our case for completely absorbing boundaries, $r_e = 0$. The value of z_e reduces to $2/3l_t$ $(\approx 0.7l_t)$. The extrapolation length can be adjusted to compensate for a mismatch in the index of refraction at the surface.

The photon density in a semi-infinite medium is given by

$$N(\vec{r},t) = N_R(\vec{r},t) - N_I(\vec{r},t). \tag{8}$$

The form of the photon density for the image term, $N_I(\vec{r},t)$, is the same as $N_R(\vec{r},t)$, except the location of the real source is replaced by the image source position.

In Figure 3a, an example of the fixed locations for the real source ($\vec{r}_s$) located at $(0, 0, 0)$ and image sources ($\vec{r}_i$) for the sDM and cmDM are given. In the case of the cTM, an image source is placed at $z_i = -2(1+\alpha)l_t$, as shown in Figure 3b. At early times, the distance from a point at the boundary **B :** to the center of $N_R(\vec{r},t)$ is not equal to the center of $N_I(\vec{r},t)$, so the boundary condition $N(\vec{r},t)\big|_B = 0$ at the extrapolated surface is not satisfied. This is not critical at early times because the photons move ballistically along in the forward direction and the diffusion coefficients are near zero. Hence, the photon density at the boundary and the boundary effect are negligible. After a short period, $t > 2l_t/c$, the center of $N_R(\vec{r},t)$ has relocated from $z = 0$ to $z = l_t$, as shown in Figure 1, and the center of $N_I(\vec{r},t)$ moves to $z_i = -(1+\alpha)l_t$. Then, the extrapolated boundary condition is satisfied.

The extrapolated boundary condition for a slab of thickness, L, assumed that $N(z,t) = 0$ at two extrapolated surfaces outside of the slab.[11, 12] This condition cannot be met with the

addition of a single image source. To satisfy the extrapolated boundary conditions $N(\vec{r},t)\big|_{B_1}=0$ and $N(\vec{r},t)\big|_{B_2}=0$ with $\mathbf{B_1}: z=-\alpha l_t$ and $\mathbf{B_2}: z=L+\alpha l_t$, an infinite series of images dipole sources are added. The solution now becomes

$$N(\vec{r},t)=N_R(\vec{r},t)+\left(\sum_{m=-\infty}^{\infty}N_{l^+}^{(m)}(\vec{r},t)-\sum_{m=-\infty}^{\infty}N_{l^-}^{(m)}(\vec{r},t)\right). \tag{9}$$

where, $N_{l^+}^{(m)}(\vec{r},t)$ and $N_{l^-}^{(m)}(\vec{r},t)$ represent the photon density for the positive and negative image terms, respectively. $N_{l^+}^{(m)}(\vec{r},t)$ and $N_{l^-}^{(m)}(\vec{r},t)$ are similar to $N_R(\vec{r},t)$, except the location of the real source is replaced by either a positive or negative image source located at $(0,0,z_i^m)$. The number of dipole sources that are necessary for an accurate calculation depends on the optical properties of the slab and the maximum allowed time for the measurement.

For the sDM and cmDM, the fixed locations for the image dipoles with $m=0$ and $m=1$ are given in Figure 4a. Using the sDM, the locations of the positive and negative image sources for $m<0$ and $m>1$ are $z_i^m=2m(L+2\alpha l_t)$ for positive sources and $z_i^m=2m(L+2\alpha l_t)-2\alpha l_t$ for negative sources. For the cmDM, the locations for infinite dipole sources are similar to those for the sDM. However, to determine the source position for the cmDM, one l_t must be added to the positive source location of the sDM, while one l_t must be deducted from its negative source location. For the cTM, in order compensate $N_R(\vec{r},t)$ by $\left(\sum_{m=-\infty}^{\infty}N_{l^+}^{(m)}(\vec{r},t)-\sum_{m=-\infty}^{\infty}N_{l^-}^{(m)}(\vec{r},t)\right)$, the locations of the positive and negative image sources now depend on whether they are located above or below the slab, as shown in Figure 4b. As with the semi-infinite geometry, the centers

of $N_R(\vec{r},t)$ and $N_{I^{+,-}}^{(m)}(\vec{r},t)$ for the slab do not offset each other during the early time. Thus, neither of the extrapolated boundary conditions, $N(\vec{r},t)\big|_{B_1}=0$ or $N(\vec{r},t)\big|_{B_2}=0$ are initially satisfied.

The initial positions are $z_i^m = 2m(L+2\alpha l_t)$ for positive sources and $z_i^m = 2m(L+2\alpha l_t)-2l_t(\alpha+1)$ for negative sources located above the slab ($m\le 0$). While for dipole pairs located below the upper physical surface of the slab ($m>0$), the starting locations are $z_i^m = 2m(L+2\alpha l_t)+2l_t$ for positive sources and $z_i^m = 2m(L+2\alpha l_t)-2l_t\alpha$ for negative sources. In both cases, the movement of the image dipole pairs during the early time is towards the two extrapolated boundaries $\mathbf{B_1}: z=-\alpha l_t$ and $\mathbf{B_2}: z=L+\alpha l_t$. After a short period, $t>2l_t/c$, the centers of $N_R(\vec{r},t)$ and $\sum_{m=-\infty}^{\infty} N_I^{(m)}(\vec{r},t)$ are the same are those of the cmDM for all m. The extrapolated boundary conditions are now achieved.

The results for a uniform semi-infinite and the slab media for $z_{sd_0}=7.0l_t$ are shown in Figures 5a and 5b, respectively. In all the slab geometries, the thickness, L, of each slab is equal to z_{sd_0}. For the semi-infinite and slab media, the early time results are the same as those for the infinite medium because the effects from the flat surfaces are negligible for $z_{sd_0}\le 2l_t$. For small source-detector separations within either geometries, the cmDM again fails to yield a real peak and the peak from the sDM is clearly too weak for any reasonable experimental measurements. For small z_{sd_0}, the physical boundary effects can only be viewed far into the diffusive regime. As z_{sd_0} increases, the cTM and the cmDM yield nearly the same amplitude. Because of the

anisotropic effects that are retained by the cTM, the photon density from the cTM is time-delayed from that of the cmDM.

The photon density generated by the cTM for all three geometries can be viewed for the nondiffusive $\left(z_{sd_0} = 2.0l_t\right)$ and diffusive $\left(z_{sd_0} = 7.0l_t\right)$ regimes in Figures 6a and 6b, respectively. The non-diffusive regime is the same for each geometric configuration. More importantly, the cTM shows a long turn-on time and does not give a fake peak even when z_{sd_0} is small. The general pulse shape is the same for each configuration, however, the exponential decay does vary depending on the media. The slab exhibits a faster exponential decay, while both the semi-infinite and slab media have broader peak with a slower decay. As z_{sd_0} is increased, the damping effect from reflections at the surfaces is evident. From a semi-infinite medium to a slab medium, the effective diffusion coefficient is reduced as the number of physical boundaries increases.[13] Relevant non-diffusive information about photon migration is present during the early times for all three geometric configurations. Our model, unlike the other diffusion models, does not neglect or distort the non-diffusive regime for either the semi-infinite or slab media even when the z_{sd_0} is small.

We used the extrapolated boundary condition with a non-reflecting physical boundary $\left(r_e = 0\right)$ at $z = 0$. A cloud layer satisfied the physical boundary condition with water droplets located inside air as the scatters. Our solution can easily be modified to include reflecting boundaries $\left(r_e \neq 0\right)$ by changing the location of the extrapolated boundaries. Using a modified α created by multiplying the original α (for $r_e = 0$) by a factor $\left(1 + r_e\right)/\left(1 - r_e\right)$, we can determine the new position of each image source. Paasschens and 't Hooft have another

formula for reflecting boundaries with $r_e \neq 0$ which adds both a mirror point source and a mirror line source to satisfy the extrapolated boundary condition.[16] In the case of $r_e = 0$, their result is in agreement with our results. Using our method, corresponding mirror sources can also be defined for the cumulant approximation.

In conclusion, we are able to track the transport of photons from the near ballistic to the final diffusive stage for both semi-infinite and slab geometries using the cTM. Unlike the sDM and cmDM, we can obtain an accurate picture for the photon migration for $L < 7l_t$, as well as for $L > 7l_t$. For $t >> l_t/c$, the results from the cTM match those obtained using the cmDM. The effects of the physical boundaries can be viewed by the variations in the amplitude and the long-tail decay for $z_{sd_0} \geq 7l_t$. When z_{sd_0} is small, the cTM provides a time-resolved profile that can be reasonably compared with experimental measurements for photon pulse propagation in clouds and seawater.

This work is supported in part by Lockheed Martin, USAMRMC (Award DAMD17-98-1-8147) DARPA, NYSTAR, and NASA IRA.

References

1. B. Chance and R. R. Alfano, eds., *Optical Tomography, Photon Migration, and Spectroscopy of Tissue and Model Media, Theory, Human Studies, and Instrumentation*, Proc. SPIE **2389**, 1995.
2. G. Mitic, J. Kolzer, J. Otto, E. Plies, G. Solkner, and W. Zinth, "Time-gated transillumination of biological tissues and tissue-like phantoms", Appl. Opt. **33**, 6699-6710, 1994.
3. Y. Gu and K. N. Liou, "Interaction of radiation, microphysics, and turbulence in the evolution of cirrus clouds", J. of Atom. Sci. **57**, 2463-2479, 2000.
4. S. Ito and K. Furutsu, "Theory of light pulse propagation through thick clouds", J. Opt. Soc. Am. **70**, 366-374, 1980.
5. K. M. Yoo, Feng Liu, and R. R. Alfano, "When does the diffusion approximation fail to describe photon transport in random media?", Phys. Rev. Lett. **64**, 2647-2650, 1990.
6. A. Ishimaru, *Wave propagation and scattering in random media*, Academic Press, New York, 1978.
7. M. E. Zavallos, A. Y. Polischuck, B. B. Das, Feng Liu, and R. R. Alfano, "Time-resolved photon scattering measurements from scattering media fitted to non-Euclidean and conventional diffusion models", Phy. Rev. E **57**, 7244-7253, 1998.
8. W. Cai, M. Lax, and R. R. Alfano, "Cumulant solution of the elastic Boltzmann transport equation in an infinite uniform medium", Phys. Rev. E **61**, 3871-3876, 2000.
9. W. Cai, M. Lax, and R. R. Alfano, "Analytical solution of the elastic Boltzmann transport equation in an infinite uniform medium using cumulant expansion", J. Phys. Chem. B **104**, 3996-4000, 2000.
10. R. Haskell, L. Svaasand, T. Tsay, T. Feng, M. McAdams, and B. Tromberg, "Boundary conditions for the diffusion equation in radiative transfer", J. Opt. Soc. Am. A **11**, 2626-2741, 1994.
11. M. Patterson, B. Chance, and B. C. Wilson, "Time resolved reflectance and transmittance for the non-invasive measurement of tissue optical properties", App. Opt. **28**, 2331-2336, 1989.

12. D. Contini, F. Martelli, and G. Zaccanti, "Photon migration through a turbid slab described by a model based on diffusion approximation. I. Theory", App. Opt. **36**, 4587-4599, 1997.

13. A. Lagendijk, R. Vreeker, and P. De Vries, "Influence of internal reflection on diffusive transport in strongly scattering media", Phys. Lett. A **136**, 81, 1989.

14. S. Ma, *Statistical Mechanics* (World Scientific, Pennsylvania, 1985).

15. L. Mandel and E. Wolf, *Optical Coherence and Quantum Optics*, (Cambridge University Press, Massachusetts, 1995).

16. J. C. J. Paasschens and G. W. 't Hooft, "Influence of boundaries on the imaging of objects in turbid media", J. Opt. Soc. Am. A **15**, 1797 – 1812, 1996.

17. Alfano Science reference

18. M. E. Zevallos, A. Ya Polishchuk, F. Liu, B. B. Das, and R. R. Alfano, "Time-resolved scattering measurements from scattering media fitted to non-Euclidean and conventional diffusion model", Phys. Rev. E **53**, 5523 , 1996.

19. The concept of "cumulant" can be explained using a 1D case: There is a random variable x, with a probability distribution function $P(x)$. Instead of using $P(x)$ to describe the distribution, we define the nth moment of x, $\langle x^n \rangle = \int x^n P(x) dx$, and corresponding the nth cumulant $\langle x^n \rangle_c$ can be derived from moments. The first cumulant $\langle x \rangle_c$ gives the central position of x, The second cumulant $\langle x^2 \rangle_c$ gives the half-width of the distribution. The higher cumulants are related to detailed shape of the distribution. $\langle x^3 \rangle_c$ describes the skewness, or asymmetry of the distribution, and $\langle x^4 \rangle_c$ describes the "kurtosis" of the distribution, that is the extent to which it differs from the standard bell shape associated

with the normal distribution function, and so on. Therefore, the cumulants describe the distribution in an intrinsic way by subtracting off the effects of all lower order moments. Hence, when more higher order cumulants are included, a more detailed shape of the distribution is obtained.

List of Figures

Figure 1. The moving center of the photon density function R_z and the diffusion coefficients D_{zz} and $D_{xx}\left(=D_{yy}\right)$ as a function of time t. For $t >> l_t/c$, R_z stops at a new position located exactly l_t from the original position.

Figure 2. Photon density for an infinite medium with the distance between the source and detector, z_{sd_0}, is given by **(a)** $z_{sd_0} = 2.0l_t$; **(b)** $z_{sd_0} = 7.0l_t$; and **(c)** $z_{sd_0} = 10.0l_t$ using $l_t = 100m$, $n = 1.33$, and $\mu_a = 0$.

Figure 3. For semi-infinite geometry, locations of the real and image sources, z_s and z_i, respectively, for **(a)** the CMDM and SDM configurations and **(b)** the CTM configuration if the real source is located at $z = 0$. For the CTM configuration, the subscripts i and f associated with z_s and z_i represent the initial and final locations of each source. An extrapolated boundary, **B**, is located at a distance $z = \alpha l_t$ from the physical boundary of the semi-infinite medium.

Figure 4. For slab geometry, **(a)** the CMDM and SDM configurations and **(b)** the CTM configuration if the real source is located $z = 0$. Extrapolated boundaries, $\mathbf{B_1}$ and $\mathbf{B_2}$, are located at distances $z = \alpha l_t$ from the physical boundaries of slab. For the CTM configuration, the subscripts i and f associated with z_s and z_i represent the initial and final locations of each source.

Figure 5. For the SDM, CMDM, and CTM, the photon density for the **(a)** semi-infinite and **(b)** one-layer uniform slab media with $z_{sd_0} = 7.0l_t$ for $l_t = 100m$, $n = 1.33$, and $\mu_a = 0$. The thickness of the slab, L, is equal to z_{sd_0} for each uniform slab media. The results for $z_{sd_0} = 2.0l_t$ are the same as those for the infinite medium during early time.

List of Figures cont'd

Figure 6. Using the CTM, the photon density for the infinite, semi-infinite, and slab media using **(a)** $z_{sd_0} = 2.0l_t$ and **(b)** $z_{sd_0} = 7.0l_t$ for $l_t = 100m$, $n = 1.33$, and $\mu_a = 0$. The thickness of the slab, L, is equal to z_{sd_0} for each uniform slab media.

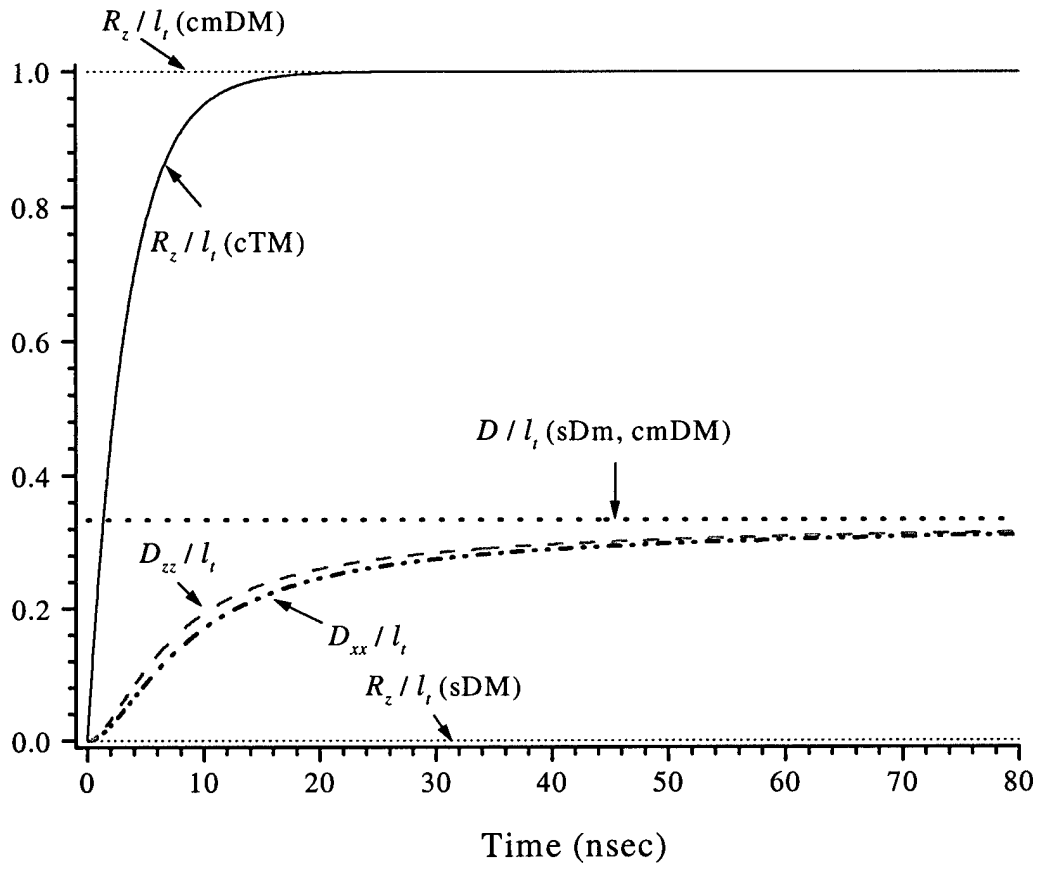
R_z / l_t (cmDM)
1.0
0.8
R_z / l_t (cTM)
0.6
D / l_t (sDm, cmDM)
0.4
D_{zz} / l_t
0.2
D_{xx} / l_t
R_z / l_t (sDM)
0.0
0
10
20
30
40
50
60
70
80
Time (nsec)

Figure 1

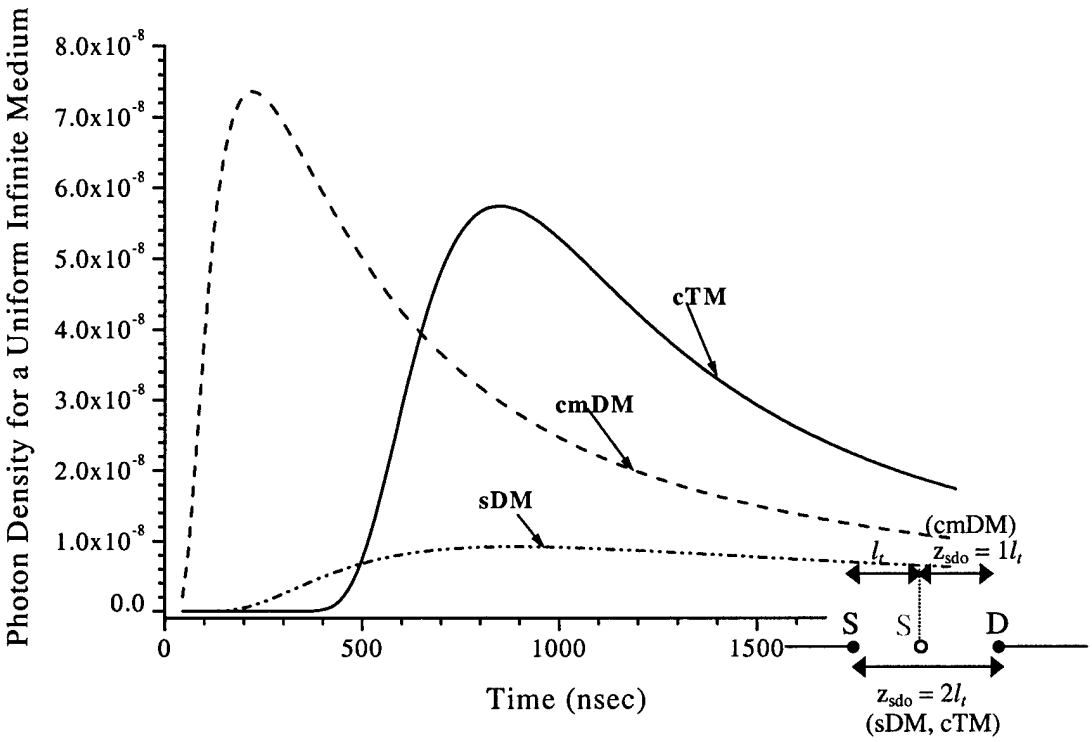
Photon Density for a Uniform Infinite Medium
8.0x10-8
7.0x10-8
6.0x10-8
5.0x10-8
4.0x10-8
3.0x10-8
2.0x10-8
1.0x10-8
0.0
0
500
1000
1500
Time (nsec)
cTM
cmDM
sDM
(cmDM)
l_t
$z_{sdo} = 1l_t$
S
S
D
$z_{sdo} = 2l_t$
(sDM, cTM)

(a)

Figure 2

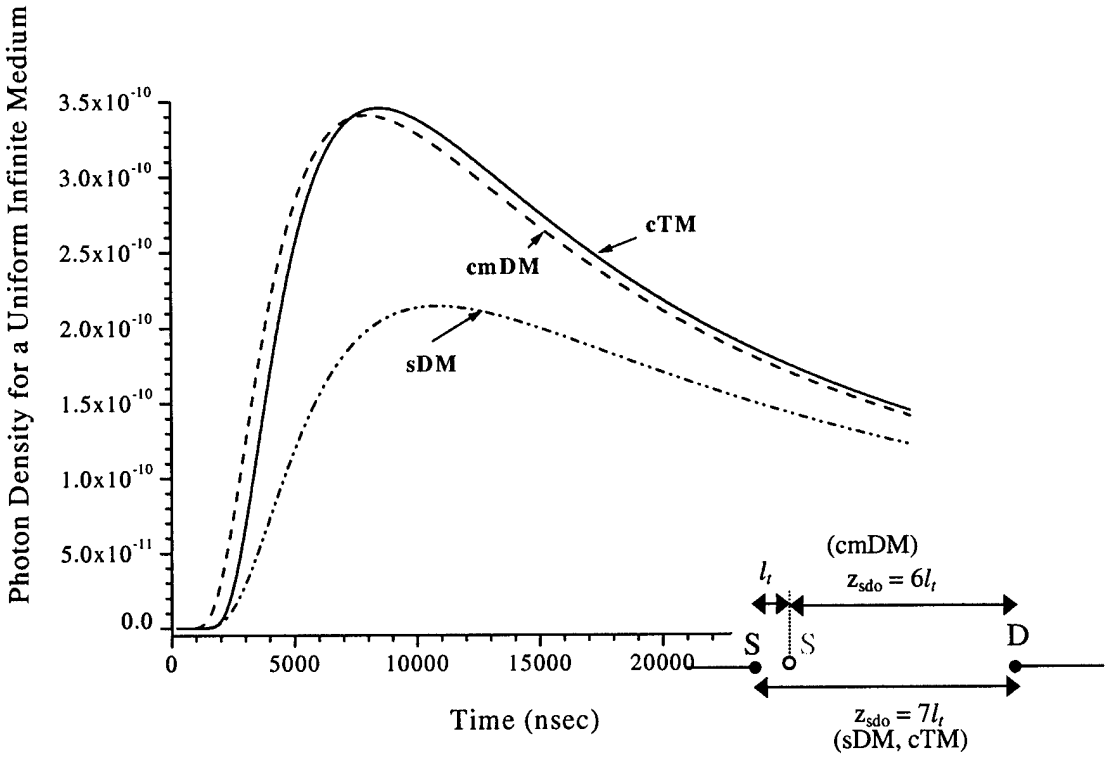
Photon Density for a Uniform Infinite Medium
3.5x10^-10
3.0x10^-10
2.5x10^-10
2.0x10^-10
1.5x10^-10
1.0x10^-10
5.0x10^-11
0.0
0
5000
10000
15000
20000
Time (nsec)
cTM
cmDM
sDM
(cmDM)
$z_{sdo} = 6l_t$
l_t
S
S
D
$z_{sdo} = 7l_t$
(sDM, cTM)

(b)

Figure 2

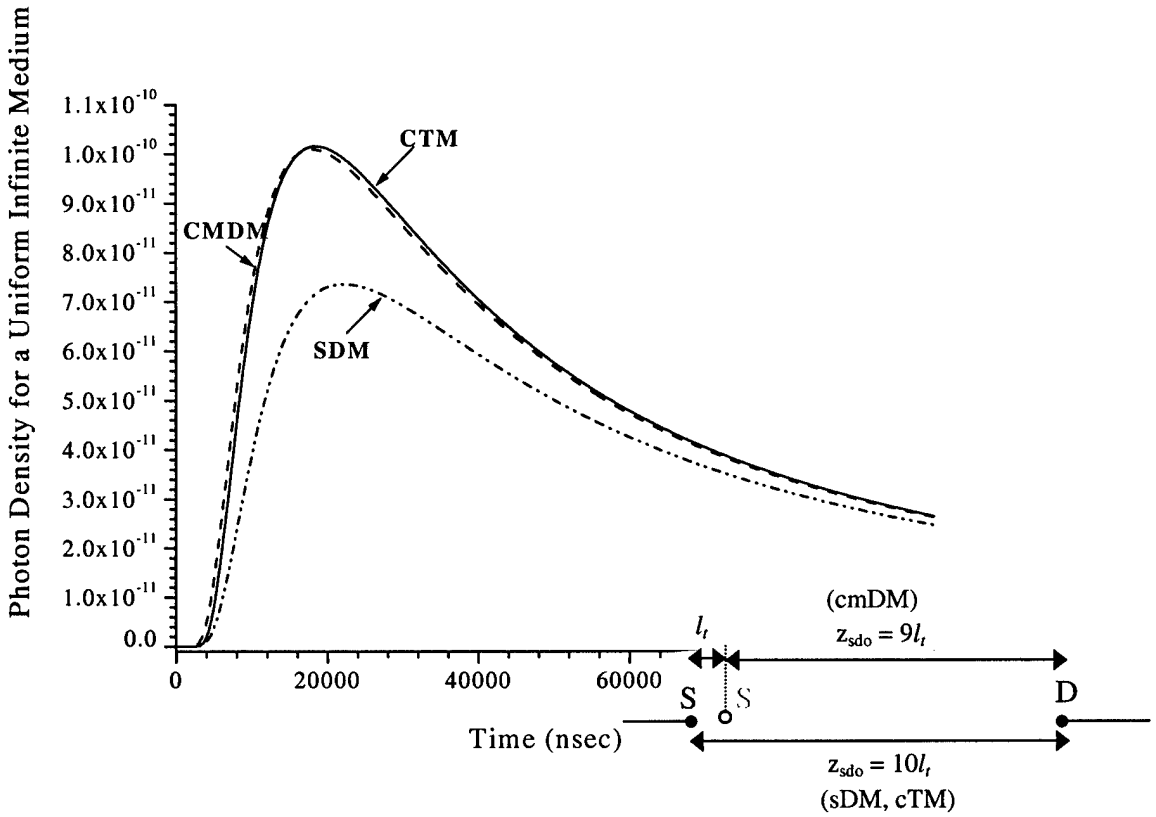
Photon Density for a Uniform Infinite Medium
1.1x10^-10
1.0x10^-10
9.0x10^-11
8.0x10^-11
7.0x10^-11
6.0x10^-11
5.0x10^-11
4.0x10^-11
3.0x10^-11
2.0x10^-11
1.0x10^-11
0.0
0
20000
40000
60000
Time (nsec)
CTM
CMDM
SDM
(cmDM)
$z_{sdo} = 9l_t$
l_t
S
S
D
$z_{sdo} = 10l_t$
(sDM, cTM)

(c)

Figure 2

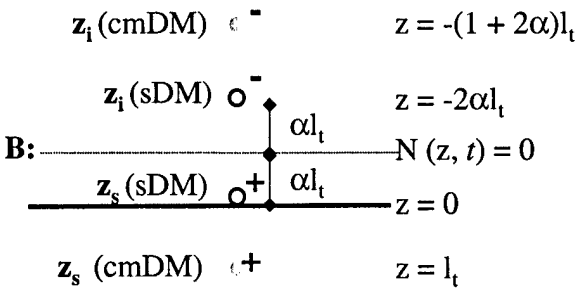
z_i (cmDM)
$z = -(1 + 2\alpha)l_t$
z_i (sDM)
$z = -2\alpha l_t$
αl_t
B:
$N(z, t) = 0$
z_s (sDM)
αl_t
$z = 0$
z_s (cmDM)
$z = l_t$

(a)

Figure 3

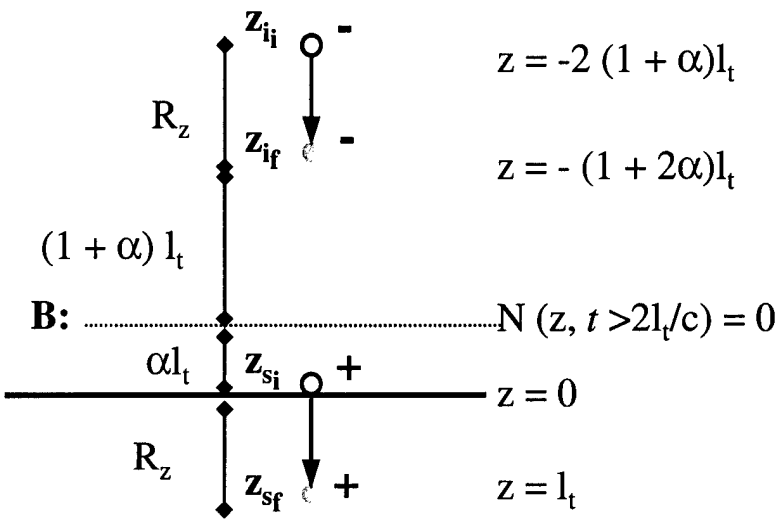
z_{i_i}
-
$z = -2\ (1 + \alpha) l_t$
R_z
z_{i_f}
-
$z = -\ (1 + 2\alpha) l_t$
$(1 + \alpha)\ l_t$
B:
$N\ (z,\ t > 2l_t/c) = 0$
αl_t
z_{s_i}
+
$z = 0$
R_z
z_{s_f}
+
$z = l_t$

(b)

Figure 3

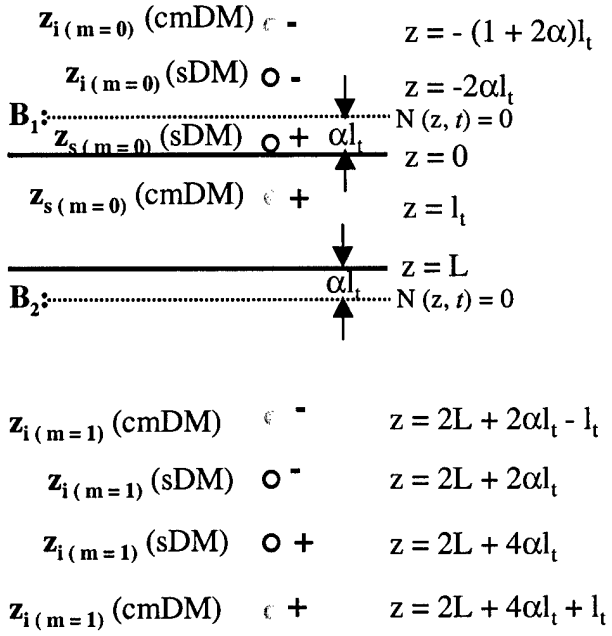
$z_{i\,(m=0)}$ (cmDM) - $z = -(1 + 2\alpha)l_t$
$z_{i\,(m=0)}$ (sDM) o - $z = -2\alpha l_t$
B_1: N (z, t) = 0
$z_{s\,(m=0)}$ (sDM) o + αl_t
$z = 0$
$z_{s\,(m=0)}$ (cmDM) + $z = l_t$
$z = L$
αl_t
B_2: N (z, t) = 0
$z_{i\,(m=1)}$ (cmDM) - $z = 2L + 2\alpha l_t - l_t$
$z_{i\,(m=1)}$ (sDM) o - $z = 2L + 2\alpha l_t$
$z_{i\,(m=1)}$ (sDM) o + $z = 2L + 4\alpha l_t$
$z_{i\,(m=1)}$ (cmDM) + $z = 2L + 4\alpha l_t + l_t$

(a)

Figure 4

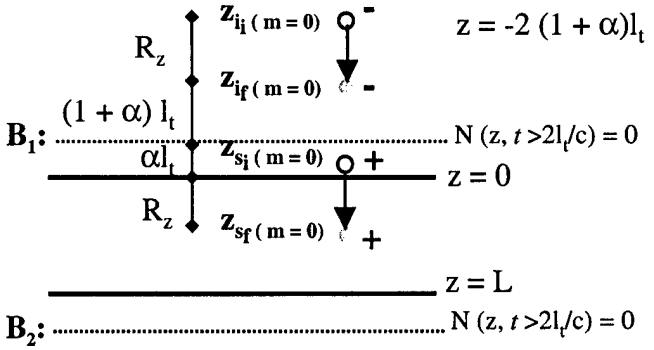
$z_{i_i\,(m=0)}$
$z = -2\,(1+\alpha)l_t$
R_z
$z_{i_f\,(m=0)}$
$(1+\alpha)\,l_t$
B_1:
$N\,(z, t>2l_t/c) = 0$
αl_t
$z_{s_i\,(m=0)}$
$z = 0$
R_z
$z_{s_f\,(m=0)}$
$z = L$
B_2:
$N\,(z, t>2l_t/c) = 0$

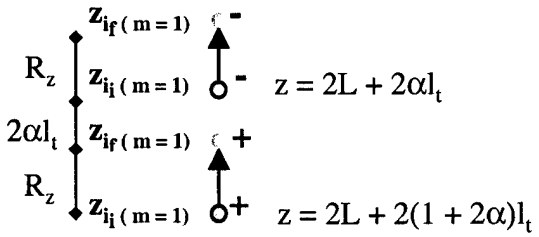
$z_{i_f\,(m=1)}$
R_z
$z_{i_i\,(m=1)}$
$z = 2L + 2\alpha l_t$
$2\alpha l_t$
$z_{i_f\,(m=1)}$
R_z
$z_{i_i\,(m=1)}$
$z = 2L + 2(1+2\alpha)l_t$

(b)

Figure 4

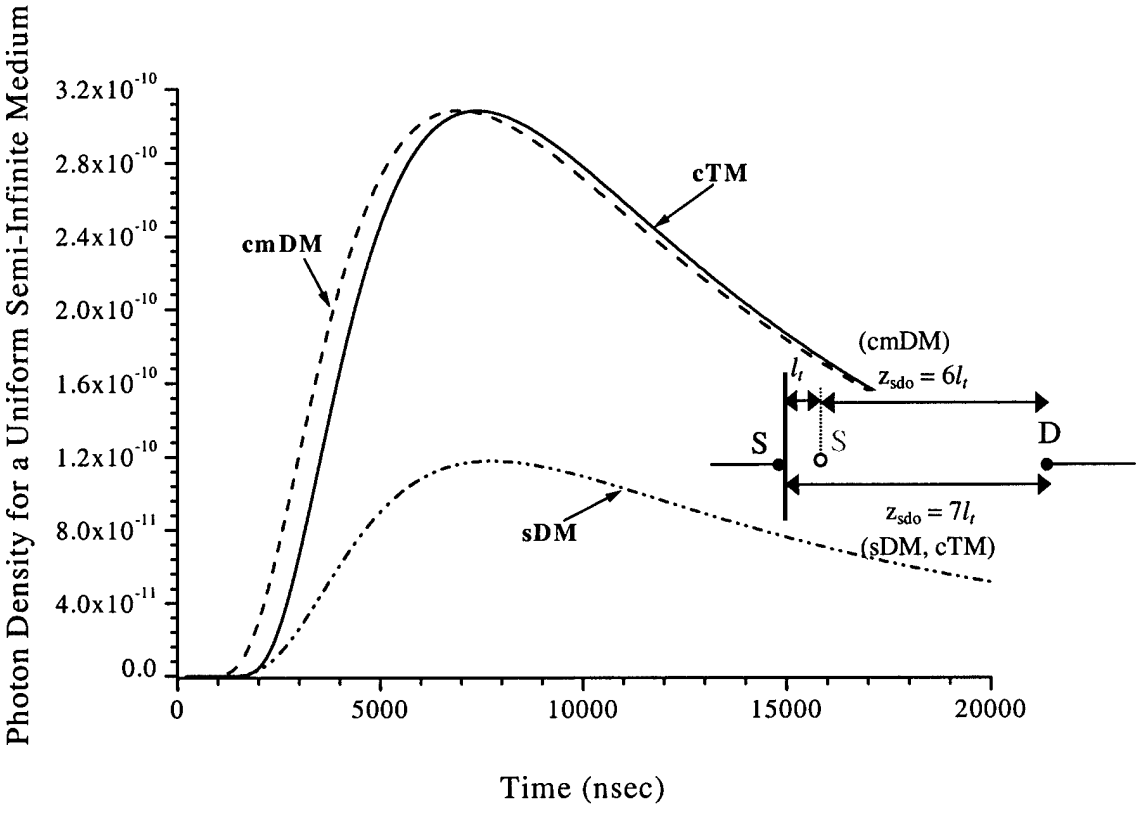
Photon Density for a Uniform Semi-Infinite Medium
3.2x10^-10
2.8x10^-10
2.4x10^-10
2.0x10^-10
1.6x10^-10
1.2x10^-10
8.0x10^-11
4.0x10^-11
0.0
0
5000
10000
15000
20000
Time (nsec)
cmDM
cTM
sDM
(cmDM)
z_sdo = 6l_t
l_t
S
S
D
z_sdo = 7l_t
(sDM, cTM)

(a)

Figure 5

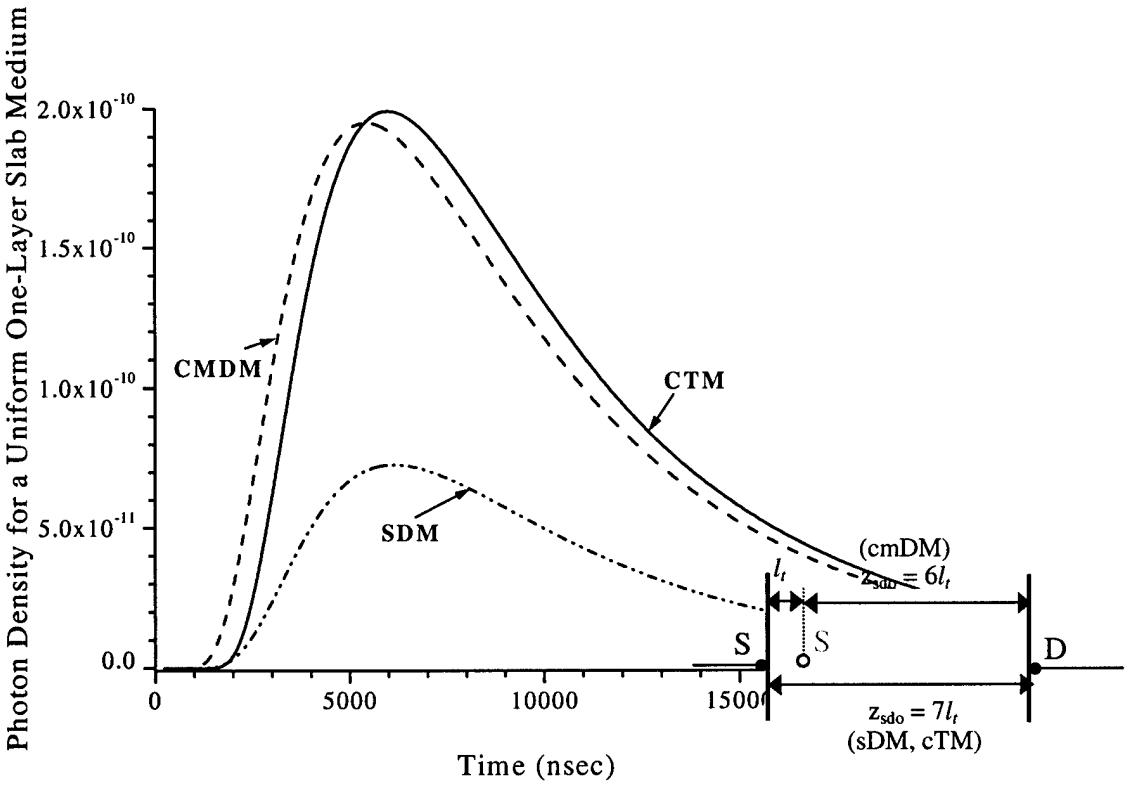
Photon Density for a Uniform One-Layer Slab Medium
2.0x10^-10
1.5x10^-10
1.0x10^-10
5.0x10^-11
0.0
0
5000
10000
15000
Time (nsec)
CMDM
CTM
SDM
(cmDM)
$z_{sdb} = 6l_t$
l_t
S
S
D
$z_{sdo} = 7l_t$
(sDM, cTM)

(b)

Figure 5

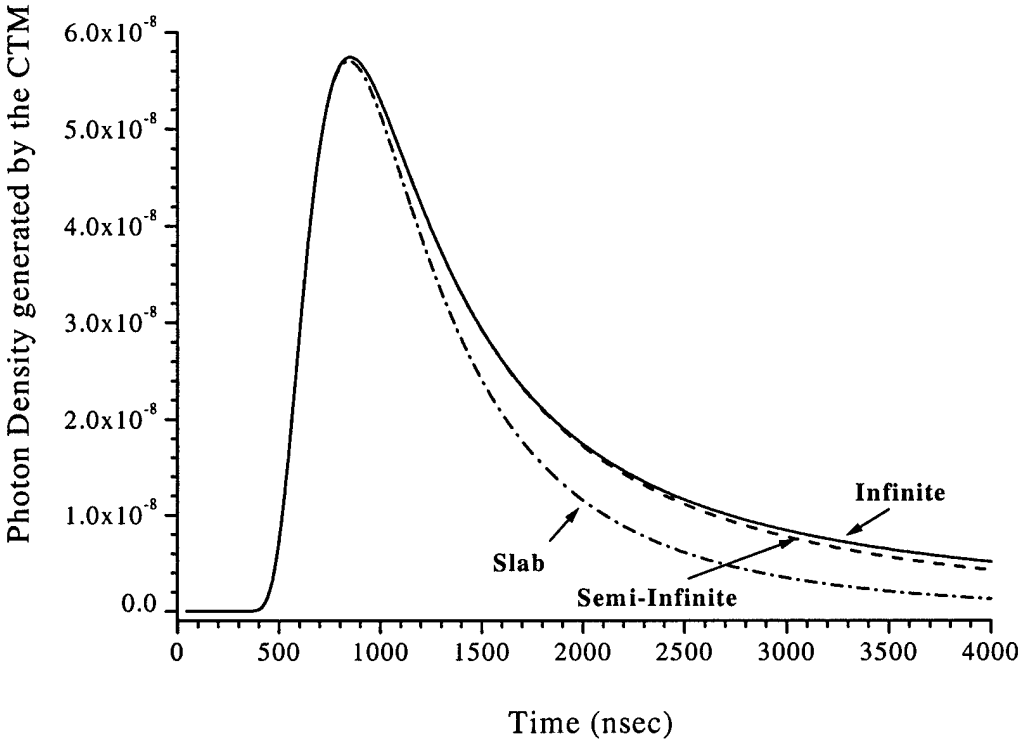
Photon Density generated by the CTM
6.0x10-8
5.0x10-8
4.0x10-8
3.0x10-8
2.0x10-8
1.0x10-8
0.0
0
500
1000
1500
2000
2500
3000
3500
4000
Time (nsec)
Infinite
Slab
Semi-Infinite

(a)

Figure 6

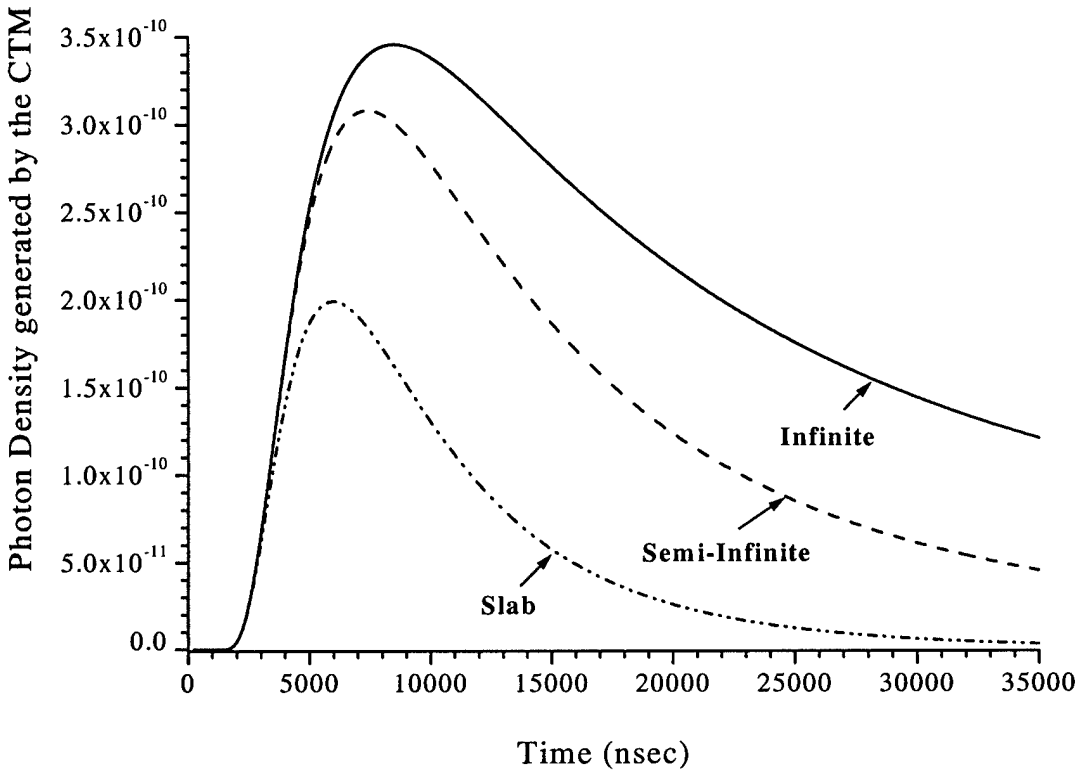
Photon Density generated by the CTM
3.5x10^-10
3.0x10^-10
2.5x10^-10
2.0x10^-10
1.5x10^-10
1.0x10^-10
5.0x10^-11
0.0
0
5000
10000
15000
20000
25000
30000
35000
Time (nsec)
Infinite
Semi-Infinite
Slab

(b)

Figure 6

Xu *et al.* Vol. 18, No. 7/July 2001/J. Opt. Soc. Am. A 1535

Time-resolved Fourier optical diffuse tomography

M. Xu, M. Lax, and R. R. Alfano

Institute for Ultrafast Spectroscopy and Lasers, New York State Center of Advanced Technology for Ultrafast Photonic Materials and Applications, and Department of Physics, The City College and Graduate Center of City University of New York, New York, NY 10031

Received September 5, 2000; revised manuscript received December 11, 2000; accepted December 13, 2000

Time-resolved Fourier optical diffuse tomography is a novel approach for imaging of objects in a highly scattering turbid medium with use of an incident (near) plane wave. The theory of the propagation of spatial Fourier components of the scattered wave field is presented, along with a fast algorithm for three-dimensional reconstruction in a parallel planar geometry. Examples of successful reconstructions of simulated hidden absorptive or scattering objects embedded inside a human-tissue-like semi-infinite turbid medium are provided.
© 2001 Optical Society of America
OCIS codes: 170.6960, 290.7050, 290.1350.

1. INTRODUCTION

Research on the use of near-infrared diffusive light for biomedical imaging and diagnosis has advanced over the past decade because of the potential of the technique to be a safe, noninvasive, affordable, and superior diagnostics tool.[1–3] In the search for a methodology that provides fast data acquisition and reconstruction to perform imaging with high resolution in real time, a variety of techniques have been explored including the use of time-resolved picosecond pulses, continuous waves, and diffuse photon-density waves. Most methods reconstruct three-dimensional (3D) optical property maps (OPMs) by matrix inversion, by iterative techniques, or by 3D rendering of two-dimensional (2D) projection images.[4–8] The degree of difficulty of inverting the whole 3D map at one time is usually time prohibitive when the number of volume elements involved increases, and 3D rendering of two-dimensional projection images requires extra depth information of inhomogeneities inside turbid media to behave well, and it has other limitations.[7,9]

In this paper, we first introduce the theory of propagation of the spatial Fourier component of the scattered wave field inside a turbid medium. We then develop a new optical diffuse imaging methodology based on this theory, using the two-dimensional Fourier transform of photon intensity on a plane to detect inhomogeneities in a highly scattering turbid medium when the medium is illuminated by a picosecond (near-) plane-wave pulse. In such a spatial Fourier space, the picture of photon migration is much simplified in the sense that different spatial frequency components of the OPM (2D Fourier transform on the xy plane) are decoupled from one another and depend only on the corresponding spatial frequency component of the photon intensity on the detector plane. On the basis of this observation, we obtain a super-fast reconstruction of a 3D OPM by matrix inversion of each spatial component independently. The effect of noise is explicitly handled by controlling the set of spatial frequency components and the regularization parameters used in the matrix inversion. After a rigorous account of the theory and a brief description of the algorithm, examples of reconstruction, by using backscattered photons, of absorptive and scattering inhomogeneities located up to 2 cm below the surface of a human-tissue-like semi-infinite turbid medium are presented.

2. THEORY

The propagation of photon density $\phi(\mathbf{r}, t)$ at position $\mathbf{r}$ and time t in a highly scattering turbid medium can be described by the diffusion equation

$$\frac{\partial}{\partial t}\phi(\mathbf{r}, t) - c\nabla \cdot D(\mathbf{r})\nabla\phi(\mathbf{r}, t) + c\mu_a(\mathbf{r})\phi(\mathbf{r}, t) = S(\mathbf{r}, t). \quad (1)$$

The absorption coefficient μ_a (per unit length), and the diffusion coefficient $D = 1/(3\mu_s')$, where μ_s' is the reduced scattering coefficient, may depend on the position in the medium; c is the speed of light inside the medium, and S is the source term describing the density of photons generated per second.

For the case of a uniform medium and an incident source $S(\mathbf{r}, t)$ ($S = 0$ when $t < 0$), the incident wave field is $\phi_i(\mathbf{r}, t) = \int d^3\mathbf{r}' \int_0^t dt' S(\mathbf{r}', t')G(\mathbf{r}, \mathbf{r}', t - t')$ where $G(\mathbf{r}, \mathbf{r}', t)$ is the Green's function for the diffusion equation in a uniform turbid medium. When some weak inhomogeneities (objects such as tumors) are embedded in the medium, we write

$$\mu_{a,\mathrm{obj}}(\mathbf{r}) = \mu_a + \delta\mu_a(\mathbf{r}),$$
$$\mu_{s,\mathrm{obj}}'(\mathbf{r}) = \mu_s' + \delta\mu_s'(\mathbf{r}), \quad (2)$$

where μ_a and μ_s' are the constant absorption and reduced scattering coefficients of the otherwise homogeneous medium and $\mu_{a,\mathrm{obj}}(\mathbf{r})$ and $\mu_{s,\mathrm{obj}}'(\mathbf{r})$ are the absorption and reduced scattering coefficients of the embedded inhomogeneity that are spatially dependent. Plugging Eq. (2) into

0740-3232/2001/071535-08$15.00 © 2001 Optical Society of America

Eq. (1) and noting the diffusion parameter of the inhomogeneity $D_{\text{obj}}(\mathbf{r}) = D + \delta D(\mathbf{r}) = 1/(3\mu_s') - \delta\mu_s'(\mathbf{r})/(3\mu_s'^2)$, we have

$$\frac{\partial}{\partial t}\phi(\mathbf{r},t) - Dc\nabla^2\phi(\mathbf{r},t) + \mu_a c\,\phi(\mathbf{r},t) = S(\mathbf{r},t) + c\nabla\cdot\delta D(\mathbf{r})\nabla\phi(\mathbf{r},t) - c\,\delta\mu_a(\mathbf{r})\phi(\mathbf{r},t). \quad (3)$$

The complete right-hand side of Eq. (3) now acts as the source term, of which $S(\mathbf{r},t)$ contributes to the unperturbed wave field $\phi_0 = \phi_i(\mathbf{r},t)$ and the rest of the terms contribute to the scattered wave field,

$$\begin{aligned}\phi_s(\mathbf{r},t) &= \phi(\mathbf{r},t) - \phi_0(\mathbf{r},t)\\ &= \int \mathrm{d}^3\mathbf{r}'\int_0^t \mathrm{d}t' G(\mathbf{r},\mathbf{r}',t-t')\\ &\quad\times[c\nabla_{\mathbf{r}'}\cdot\delta D(\mathbf{r}')\nabla_{\mathbf{r}'}\phi(\mathbf{r}',t')\\ &\quad - c\,\delta\mu_a(\mathbf{r}')\phi(\mathbf{r}',t')]\\ &= -\int \mathrm{d}^3\mathbf{r}'\int_0^t \mathrm{d}t' G(\mathbf{r},\mathbf{r}',t-t')\delta\mu_a(\mathbf{r}')c\,\phi(\mathbf{r}',t')\\ &\quad + \int \mathrm{d}^3\mathbf{r}'\int_0^t \mathrm{d}t'\frac{\delta\mu_s'(\mathbf{r}')c}{3\mu_s'^2}\nabla_{\mathbf{r}'}G(\mathbf{r},\mathbf{r}',t-t')\\ &\quad\cdot\nabla_{\mathbf{r}'}\phi(\mathbf{r}',t'), \end{aligned} \quad (4)$$

after integration by parts.

To first order in the variation of optical absorption and reduced scattering coefficients, we can just replace $\phi(\mathbf{r}',t')$ in Eq. (4) with ϕ_i, i.e., the total wave field is a superposition of the incident wave field ϕ_i and the singly scattered wave field ϕ_s. This is the well-known Born approximation.

Now consider the configuration of the frequently studied parallel planar geometry (slab or semi-infinite) with its boundaries at $z = 0$ and $z = d$ ($d = +\infty$ for semi-infinite geometry). The exact Green's function is[10]

$$G(\mathbf{r},\mathbf{r}',t) = \frac{1}{4\pi Dct}\exp\left(-\frac{|\rho-\rho'|^2}{4Dct} - \mu_a ct\right)\times G_z(z,z',t), \qquad (t>0), \quad (5)$$

where $\rho = (x,y)$, $\rho' = (x',y')$. $G_z(z,z',t)$ is chosen according to the boundary condition of the parallel planar geometry and depends only on time t and the z coordinates of the source position $\mathbf{r}$ and the target position $\mathbf{r}'$. Its two-dimensional Fourier transform on ρ is

$$\begin{aligned}\hat{G}(\mathbf{q},z,\rho',z',t) &= \int \mathrm{d}^2\rho G(\rho,z,\rho',z',t)\exp(-i\mathbf{q}\cdot\rho)\\ &= \exp(-i\mathbf{q}\cdot\rho' - Dctq^2\\ &\quad - \mu_a ct)G_z(z,z',t)\\ &= \hat{G}(\mathbf{q},z,z',t')\exp(-i\mathbf{q}\cdot\rho'). \end{aligned} \quad (6)$$

For simplicity, we restrict ourselves first to the case of a pure absorptive perturbation ($\delta\mu_a \neq 0$ and $\delta\mu_s' = 0$) and of an incident pulse $S(\mathbf{r},t) = S(\rho)\delta(z - z_s)\delta(t)$. The scattered wave field on a plane $0 < z < d$ is thus

$$\phi_s(\rho,z,t) = -\int \mathrm{d}^3\mathbf{r}'\int \mathrm{d}^2\rho''\int_0^t \mathrm{d}t' G(\mathbf{r},\mathbf{r}',t-t')\delta\mu_a(\mathbf{r}')\times cS(\rho'')G(\mathbf{r}',\rho'',z_s,t') \quad (7)$$

from Eq. (4) after ϕ is replaced by ϕ_i. Inside Eq. (7), expand the source term $S(\rho'')$ and the Green's functions $G(\mathbf{r},\mathbf{r}',t-t')$ and $G(\mathbf{r}',\rho'',z_s,t')$ into integrals of their Fourier components; thus we find

$$\begin{aligned}\phi_s(\rho,z,t) &= -\frac{1}{(4\pi^2)^3}\int \mathrm{d}^2\rho'\int \mathrm{d}z'\int \mathrm{d}^2\rho''\int_0^t \mathrm{d}t'\\ &\quad\times\int \mathrm{d}^2\mathbf{q}\hat{G}(\mathbf{q},z,z',t-t')\\ &\quad\times\exp[i\mathbf{q}\cdot(\rho-\rho')]\\ &\quad\times\delta\mu_a(\rho',z')c\int \mathrm{d}^2\mathbf{q}''\hat{S}(\mathbf{q}'')\exp(i\mathbf{q}''\cdot\rho'')\\ &\quad\times\int \mathrm{d}^2\mathbf{q}'\hat{G}(\mathbf{q}',z',z_s,t')\\ &\quad\times\exp[i\mathbf{q}'\cdot(\rho'-\rho'')]\\ &= -\frac{c}{(4\pi^2)^3}\int \mathrm{d}^2\mathbf{q}\int \mathrm{d}^2\mathbf{q}'\int \mathrm{d}^2\mathbf{q}''\int_0^t \mathrm{d}t'\int \mathrm{d}z'\\ &\quad\times\exp(i\mathbf{q}\cdot\rho)\hat{G}(\mathbf{q},z,z',t-t')\\ &\quad\times\hat{S}(\mathbf{q}'')\hat{G}(\mathbf{q}',z',z_s,t')\\ &\quad\times\int \mathrm{d}^2\rho'\,\delta\mu_a(\rho',z')\exp[-i\rho'\\ &\quad\cdot(\mathbf{q}-\mathbf{q}')]\int \mathrm{d}^2\rho''\exp[i\rho''\cdot(\mathbf{q}''-\mathbf{q}')]\\ &= -\frac{c}{(4\pi^2)^2}\int \mathrm{d}^2\mathbf{q}\int \mathrm{d}^2\mathbf{q}'\int_0^t \mathrm{d}t'\int \mathrm{d}z'\\ &\quad\times\exp(i\mathbf{q}\cdot\rho)\hat{G}(\mathbf{q},z,z',t-t')\\ &\quad\times\delta\hat{\mu}_a(\mathbf{q}-\mathbf{q}',z')\hat{S}(\mathbf{q}')\hat{G}(\mathbf{q}',z',z_s,t'), \end{aligned} \quad (8)$$

where

$$\hat{S}(\mathbf{q}) = \hat{S}(\mathbf{q},z_s) = \int \mathrm{d}^2\rho S(\rho,z_s)\exp(-i\mathbf{q}\cdot\rho),$$

$$\delta\hat{\mu}_a(\mathbf{q},z) = \int \mathrm{d}^2\rho\,\delta\mu_a(\rho,z)\exp(-i\mathbf{q}\cdot\rho)$$

are 2D Fourier transforms of the source on the $z = z_s$ plane and of the perturbation of the absorption coefficient over the $z = z$ plane, respectively. Finally, we recognize the 2D Fourier transform of the scattered wave field $\phi_s(\rho,z,t)$ on a plane z for the case of a pure absorptive perturbation:

$$\hat{\phi}(\mathbf{q},z,t) = -\frac{c}{4\pi^2}\int \mathrm{d}^2\mathbf{q}'\mathrm{d}z'\,\delta\hat{\mu}_a(\mathbf{q}-\mathbf{q}',z')\hat{S}(\mathbf{q}',z_s) \times \int_0^t \mathrm{d}t'\hat{G}(\mathbf{q},z,z',t-t')\hat{G}(\mathbf{q}',z',z_s,t'). \tag{9}$$

In a similar fashion, for the case of a pure scattering perturbation ($\delta\mu_a = 0$ and $\delta\mu_s' \neq 0$), the 2D Fourier transform of the scattered wave field is

$$\hat{\phi}_s(\mathbf{q},z,t) = \frac{c}{12\pi^2\mu_s'^2}\int \mathrm{d}^2\mathbf{q}'dz'\,\delta\hat{\mu}_s'(\mathbf{q}-\mathbf{q}',z')\hat{S}(\mathbf{q}',z_s) \times \int_0^t \mathrm{d}t'\left[\mathbf{q}\cdot\mathbf{q}'\hat{G}(\mathbf{q},z,z',t-t')\hat{G}(\mathbf{q}',z',z_s,t') + \frac{\partial\hat{G}(\mathbf{q},z,z',t-t')}{\partial z'}\frac{\partial\hat{G}(\mathbf{q}',z',z_s,t')}{\partial z'}\right]. \tag{10}$$

The general Fourier scattered wave field is the sum of Eq. (9) and Eq. (10). Denoting the convolutions

$$w_a(\mathbf{q},\mathbf{q}',z,t;z') = \int_0^t \mathrm{d}t'\hat{G}(\mathbf{q},z,z',t-t')\hat{G}(\mathbf{q}',z',z_s,t'),$$

$$w_s(\mathbf{q},\mathbf{q}',z,t;z') = \int_0^t \mathrm{d}t'\frac{\partial\hat{G}(\mathbf{q},z,z',t-t')}{\partial z'}\times\frac{\partial\hat{G}(\mathbf{q}',z',z_s,t')}{\partial z'}, \tag{11}$$

which are the weight functions involved in the propagation of spatial Fourier components of the scattered wave field, we have

$$\hat{\phi}_s(\mathbf{q},z,t) = -\frac{c}{4\pi^2}\int \mathrm{d}^2\mathbf{q}'dz'\,\delta\hat{\mu}_a(\mathbf{q}-\mathbf{q}',z') \times \hat{S}(\mathbf{q}',z_s)w_a(\mathbf{q},\mathbf{q}',z,t;z') + \frac{c}{12\pi^2\mu_s'^2} \times \int \mathrm{d}^2\mathbf{q}'dz'\,\delta\hat{\mu}_s'(\mathbf{q}-\mathbf{q}',z')\hat{S}(\mathbf{q}',z_s) \times [\mathbf{q}\cdot\mathbf{q}'w_a(\mathbf{q},\mathbf{q}',z,t;z') + w_s(\mathbf{q},\mathbf{q}',z,t;z')]. \tag{12}$$

For the simple case in which the incident wave is a plane-wave pulse (see Appendix A for justification), i.e., $S(\mathbf{r},t) = S\delta(z-z_s)\delta(t)$ where S is a constant, such that $\hat{S}(\mathbf{q},z_s) = 4\pi^2 S\delta(\mathbf{q})$, Eq. (12) simplifies to

$$\hat{\phi}_s(\mathbf{q},z,t) = -Sc\int \mathrm{d}z'\left[\delta\hat{\mu}_a(\mathbf{q},z')w_a(\mathbf{q},0,z,t;z') - \frac{\delta\hat{\mu}_s'(\mathbf{q},z')}{3\mu_s'^2}w_s(\mathbf{q},0,z,t;z')\right]. \tag{13}$$

The most salient feature of the above result [Eq. (13)] is that different spatial frequency components of $\delta\hat{\mu}_a$ and $\delta\hat{\mu}_s'$ are decoupled from one another, and the $\mathbf{q}$ component of the optical parameters depends only on the corresponding spatial frequency component of the scattered wave field $\hat{\phi}_s(\mathbf{q},z,t)$. Thus the dimension of the inverse problem to be solved below is greatly reduced, as is the computation time.

If we approximate the integration over z' by a summation and fix $z = z_d$ at the detection plane (omitting z hereafter), the Fourier scattered wave field on the detection plane is

$$\hat{\phi}_s(\mathbf{q},t) = Sc\Delta z\sum_{j=1}^{N_z}\left[-\delta\hat{\mu}_a(\mathbf{q},z_j)w_a(\mathbf{q},0,t;z_j) + \frac{\delta\hat{\mu}_s'(\mathbf{q},z_j)}{3\mu_s'^2}w_s(\mathbf{q},0,t;z_j)\right], \tag{14}$$

where Δz is the discretized step size, N_z is the total number of slices (layers) in the z direction between the source plane and the detection plane, and z_j is the z coordinate of the central position of layer j.

If we set $\mathbf{q} = 0$ in Eq. (14),

$$\hat{\phi}_s(0,t) = Sc\Delta z\sum_{j=1}^{N_z}\left[-\delta\hat{\mu}_a(0,z_j)w_a(0,0,t;z_j) + \frac{\delta\hat{\mu}_s'(0,z_j)}{3\mu_s'^2}w_s(0,0,t;z_j)\right], \tag{15}$$

the zero spatial frequency components $\delta\hat{\mu}_a(0,z_j)$ and $\delta\hat{\mu}_s'(0,z_j)$ can be readily solved without the need for a complete reconstruction. Owing to the nature of Fourier transform, they just provide the profile of the amount of total perturbation of absorption and reduced scattering coefficients per slice, i.e., the depth profile of the inhomogeneities.

The whole 3D map of absorption and reduced scattering coefficients is thus constructed through an inverse Fourier transform from all the $\mathbf{q}$ components of $\delta\hat{\mu}_a$ and $\delta\hat{\mu}_s'$ at different depths, each of which is solved independently from a series of time-resolved scattered wave field $\hat{\phi}_s$ by Eq. (14).

A schematic diagram of the procedure of image reconstruction is shown in Fig. 1. The maximum spatial frequency (cutoff frequency) of the components used in the inversion is determined through a signal-to-noise-ratio analysis in which the Fourier components whose magnitudes fall below a threshold (comparable to the noise level) are discarded. The regularization parameter in the matrix inversion is obtained by the robust L-curve method.[11] The L-corner finder, which locates the corner by maximum curvature,[12] is implemented and is used to obtain the regularization parameter. Neither visual es-

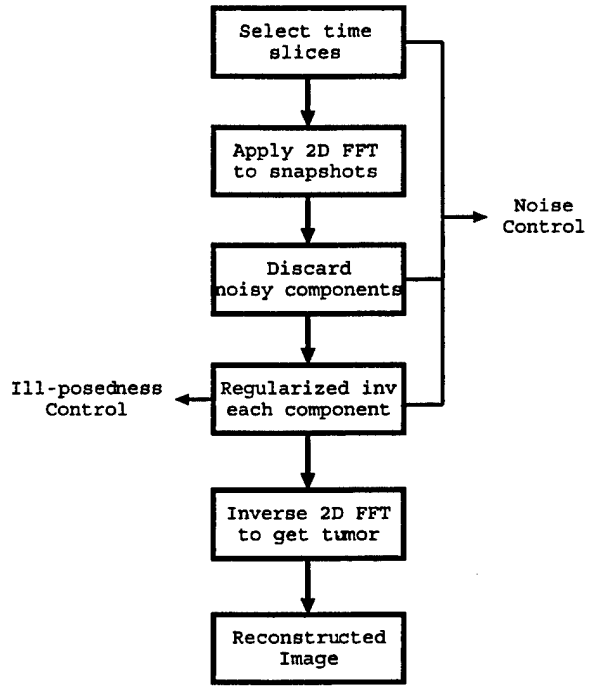

Fig. 1. Schematic diagram of image reconstruction.

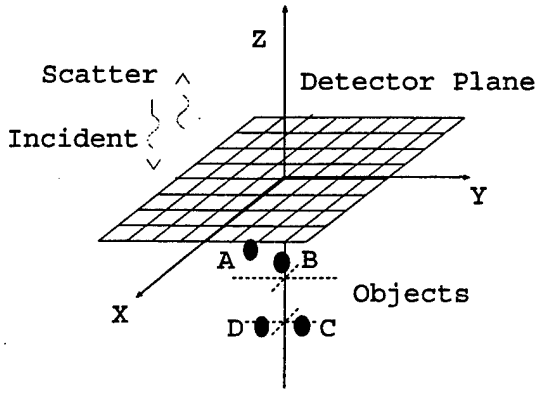

Fig. 2. Geometry for time-resolved Fourier optical diffuse tomography with use of backscattered photons. The source is a picosecond (near-) plane-wave pulse and a series of snapshots of a $10 \times 10\,\mathrm{cm}^2$ area on the surface are computed as the input to image reconstruction. Absorptive objects A (−2.5, −1.875, −0.75) cm, B (−1.25, −0.31, −0.75) cm, C (0.94, 1.56, −1.95) cm, and D (0.94, −0.625, −1.95) cm or scattering objects E (−2.5, −1.875, −0.75) cm, F (−1.25, −0.31, −0.75) cm, G (0.94, 1.56, −1.35) cm, and H (0.94, −0.625, −1.35) cm are used in the simulation.

timate nor prior information is required for this procedure. L curves are different for each spatial frequency $\mathbf{q}$. The regularization parameter is determined from the reconstruction of depth profile (where an inversion for $\mathbf{q} = 0$ is performed). The same value is then used in the full 3D reconstruction (layer reconstructions, where inversion includes $\mathbf{q} \neq 0$).

Both transmission and backscattering image reconstruction configurations can easily be made by using Eqs. (13) and (14).

3. SIMULATION

For demonstration purposes, consider a semi-infinite turbid medium ($z < 0$) with its surface at $z = 0$ (Fig. 2), whose absorption coefficient $\mu_a = 0.0033\,\mathrm{mm}^{-1}$ and reduced scattering coefficient $\mu_s' = 1.0\,\mathrm{mm}^{-1}$.

A. Absorptive Inhomogeneity

Four absorbing objects A, B, C, and D, each 6.25 mm × 6.25 mm × 3 mm and with absorption coefficient $\mu_{a,\mathrm{obj}} = 0.02\,\mathrm{mm}^{-1}$ and reduced scattering coefficient equal to that of the background, are placed at depth 7.5, 7.5, 19.5, and 19.5 mm below the surface, and their xy coordinates are (−25, −18.75), (−12.5, −3.1), (9.4, 15.6), and (9.4, 6.25) mm, respectively. The medium is illuminated by an incident pulse of a Gaussian shape of $\exp(-\rho^2/2\sigma^2)$ with $\sigma = 50$ mm inside an aperture of radius 50 mm, propagating along the negative z axis at time $t = 0$.

These parameters are potentially applicable to optical mammography of the compressed-breast-toward-chest setup with use of backscattered photons. A series of simulated measurements (total $N_t = 15$ snapshots from 300 to 2400 ps) of an area 100 mm × 100 mm on the surface plane $z = 0$ are generated by using a direct calculation for the Gaussian pulse in $\mathbf{r}$ space. The simulated data are used as input for inversion after adding a 1%, 5%, or 10% Gaussian noise.

In the reconstruction part, the near-surface region of the turbid medium of depth up to 3 cm is sliced into $N_z = 10$ layers, i.e., $\Delta z = 0.3$ cm, and objects A and B are then located on layer 3, and C and D are located on layer 7. The detection plane of an area of $10 \times 10\,\mathrm{cm}^2$ is divided uniformly into a $N_x N_y = 32 \times 32$ grid. Objects A, B, C, and D all take 2 × 2 elements by this grid. The results of reconstruction are shown below.

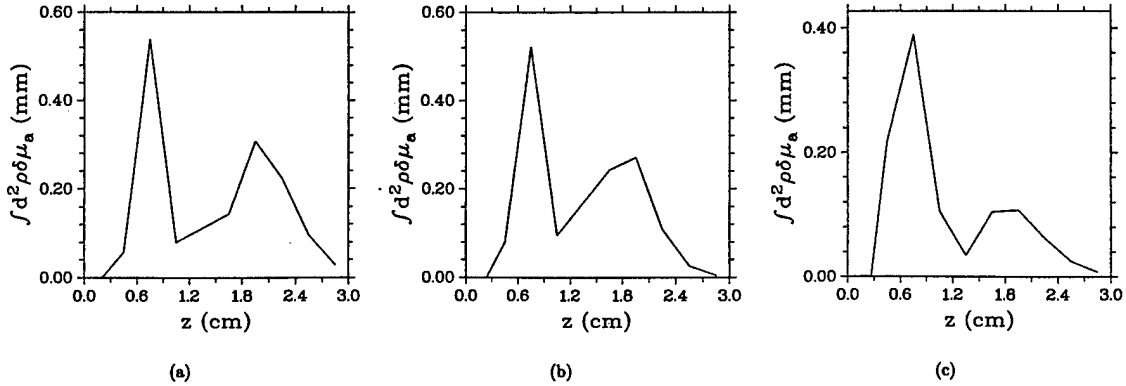

Fig. 3. Absorption depth profile for (a) with 1% noise, (b) 5% noise, and (c) 10% noise.

1. Depth Profile

The absorption depth profile, i.e., the total absorption perturbation per layer $\int d^2\rho\,\delta\mu_a(\rho, z)$ versus depth z is shown in Fig. 3 with different noise levels for cases (a) 1% noise, (b) 5% noise, and (c) 10% noise. In Fig. 3(a) there is one peak at depth $z = 0.75$ cm (layer 3) where objects A and B are embedded, and another peak at $z = 1.95$ cm (layer 7) where objects C and D are embedded. The width of the first peak at half-height is 0.34 cm, approximately the thickness of one layer (0.3 cm), which means that the depth of objects A and B is resolved very well. The second peak of objects C and D spans two and a half layers with its width of peak at half-height 0.74 cm, but its peak position is still correct.

When the level of noise increases, the peak values of both peaks decrease, and the half-widths increase. The effect on the second peak at $z = 1.95$ cm is much more significant than that on the first one at $z = 0.75$ cm.

2. Layer Reconstruction

The full 3D OPM is reconstructed. The reconstructed absorption coefficients of the layers at the two peak positions are shown in Figs. 4–6 for the three noise levels. Figure 4 shows that objects A and B are clearly resolved as two objects centered at their original positions with negligible expansion; and objects C and D at depth $z = 1.95$ cm are also detected at the correct central positions, but the resolved images are expanded on the xy plane. With an increase in noise level, the shape of objects A and B blurs from Figs. 4(a) to 5(a) and 6(a), and the blur is even worse for objects C and D under the same condition [from Figs. 4(b) to 5(b) and 6(b)].

At noise level of 1%, the reconstructed absorption parameter for objects A and B is 0.0071 mm^{-1} approximately 36% of the original value 0.02 mm^{-1} of the absorptive inhomogeneity. In other words, the object appears larger in space with a weakened absorption parameter. As the noise level increases, the effect is accentuated with a further reduction in the resolved absorption parameter.

B. Scattering Inhomogeneity

For another example, four scattering objects E, F, G, and H, each 6.25 mm × 6.25 mm × 3 mm and with reduced scattering coefficient $\mu'_{s,\mathrm{obj}} = 0.5\ mm^{-1}$ and absorption coefficient equal to that of the background, are placed at depth 7.5, 7.5, 13.5, and 13.5 mm below the surface, and

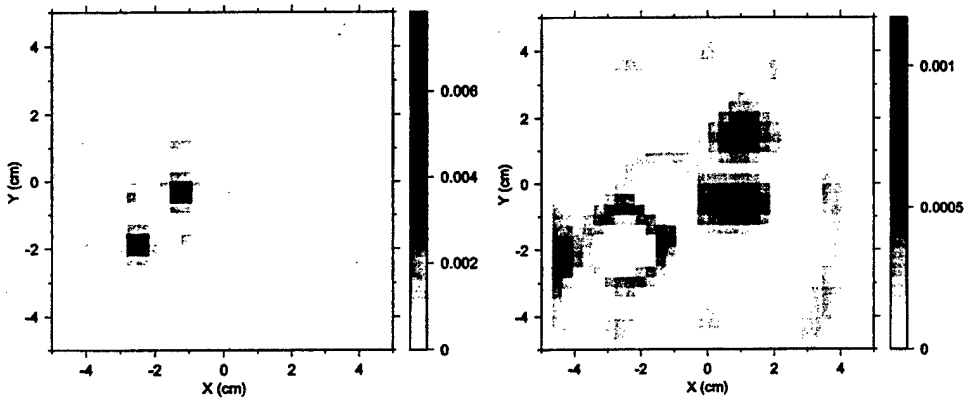

Fig. 4. Layer reconstruction at a noise level of 1%: (a) resolved objects A (left) and B (right) at $z = 0.75$ cm (layer 3); (b) resolved objects C (upper) and D (lower) at $z = 1.95$ cm (layer 7). The darkness of the pixel represents the resolved absorption coefficient in units of inverse millimeters.

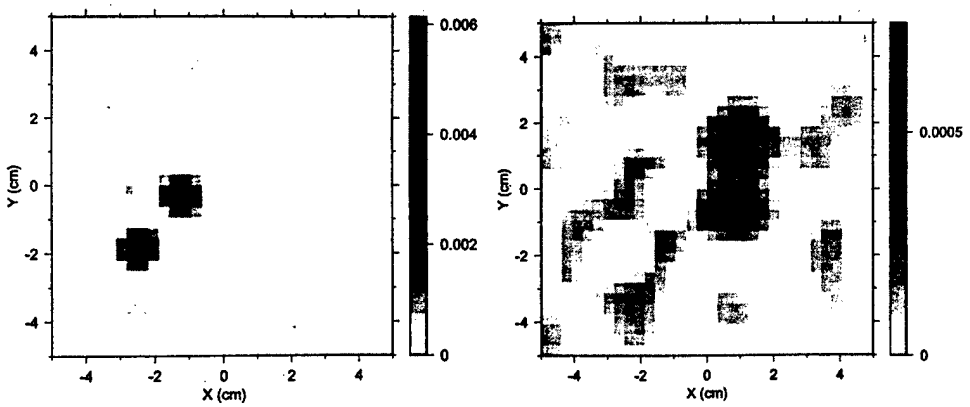

Fig. 5. Layer reconstruction at a noise level of 5%: (a) resolved objects A (left) and B (right) at $z = 0.75$ cm (layer 3); (b) resolved objects C (upper) and D (lower) at $z = 1.95$ cm (layer 7). The darkness of the pixel represents the resolved absorption coefficient in units of inverse millimeters.

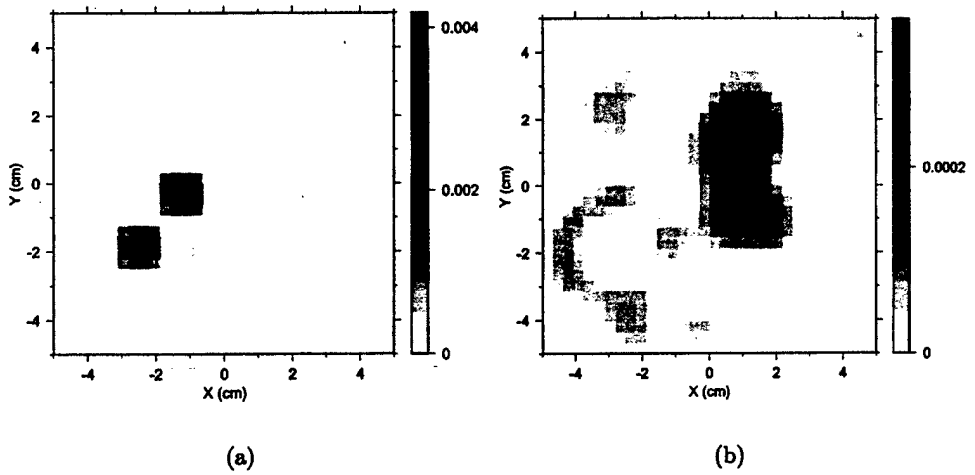

Fig. 6. Layer reconstruction at a noise level of 10%: (a) resolved objects A (left) and B (right) at $z = 0.75$ cm (layer 3); (b) resolved objects C (upper) and D (lower) at $z = 1.95$ cm (layer 7). The darkness of the pixel represents the resolved absorption coefficient in units of inverse millimeters.

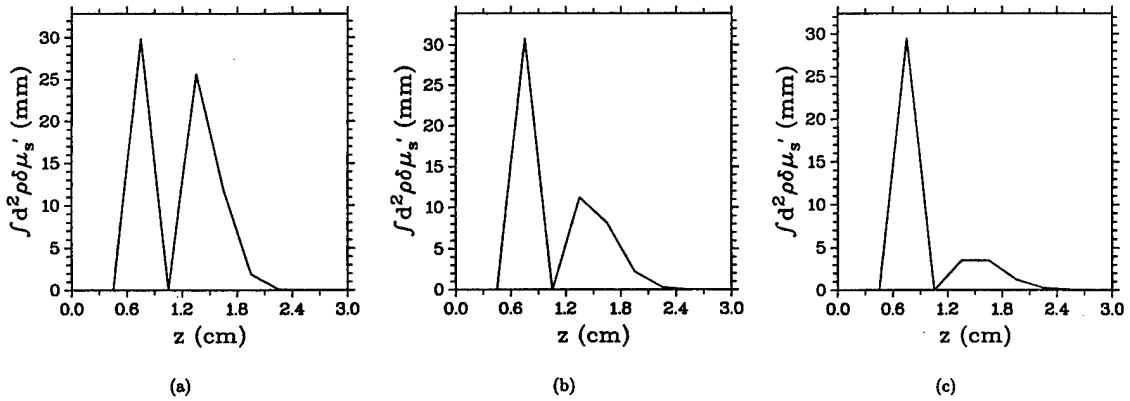

Fig. 7. Scattering depth profiles for (a) with 1% noise, (b) 5% noise, and (c) 10% noise.

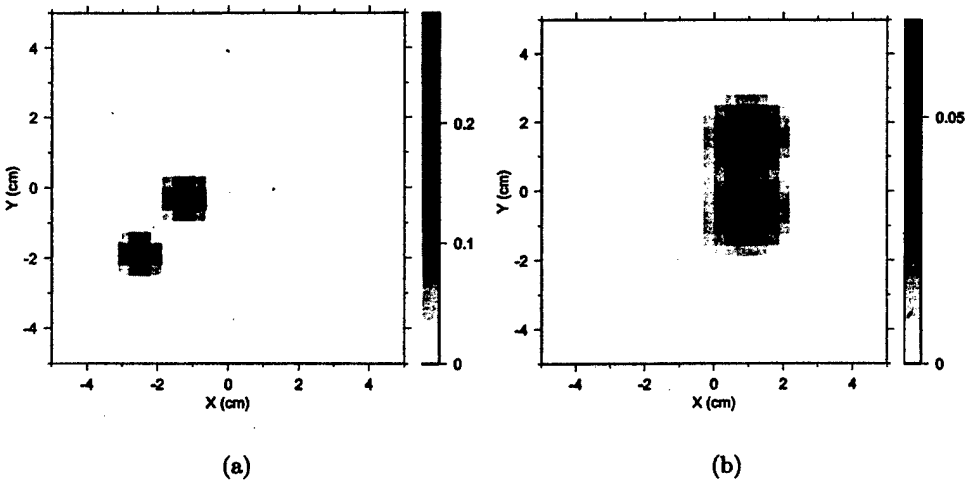

Fig. 8. Layer reconstruction at a noise level of 1%: (a) resolved objects E (left) and F (right) at $z = 0.75$ cm (layer 3); (b) resolved objects G (upper) and H (lower) at $z = 1.35$ cm (layer 5). The darkness of the pixel represents the resolved reduced scattering coefficient in units of inverse millimeters.

their xy coordinates are $(-25, -18.75)$, $(-12.5, -3.1)$, (9.4, 15.6), and (9.4, 6.25) mm, respectively. Objects E and F are now located on layer 3, and G and H are located on layer 5. The same source and inversion procedure used in the previous example are used here. The results of reconstruction are shown below.

1. Depth Profile

The scattering depth profile is shown in Fig. 7 with different noise levels for cases (a) 1% noise, (b) 5% noise, and (c) 10% noise. Two peaks are correctly revealed with the first at depth $z = 0.75$ cm (layer 3) and another at $z = 1.35$ cm (layer 5), where objects E and F, G and H are

embedded, respectively. In Fig. 7(a), the width of the first peak at half-height is 0.3 cm and that of the second peak is 0.42 cm. This means that the depth of these objects is resolved quite well.

With an increase in noise level, we observe the same behavior of decreasing quality of depth resolution as in the absorptive case.

2. Layer Reconstruction

The reconstructed scattering coefficients of the layers at the two peak positions (layer 3 and layer 5) are shown in Figs. 8–10 for the three noise levels.

We observe a result similar to that for the absorptive case. Objects E and F are better resolved than objects G and H, which are deeper into the turbid medium, and the noise has a more adverse effect on objects G and H than on objects E and F. The reconstructed reduced scattering coefficient of objects E and F is 0.27 mm^{-1}, approximately 54% of the original value of the embedded scattering inhomogeneity, at a noise level of 1%.

4. DISCUSSION

A fast time-resolved Fourier optical diffuse tomography based on decoupled propagation of spatial Fourier components of the scattered wave field when the medium is illuminated by a plane wave is presented. For a wave not strictly plane but whose zero-frequency component dominates, this approximation is still valid as long as the radial dimensions of the volume where inhomogeneities exist are much smaller than the effective width of the Gaussian beam (see Appendix A).

The image-reconstruction method provided is efficient. The optical parameters at $N_xN_yN_z$ different voxels are reconstructed from a set of N_t measurements by N_k^2 times of inversions of $N_z \times N_z$ matrices, where $N_k^2 < N_xN_y$ is the total number of Fourier components with the noisy ones discarded. Our procedure is much more efficient than a direct reconstruction, where an inversion of $N_xN_yN_z \times N_xN_yN_z$ matrix is involved. The speedup is approximately $O(N_xN_y)$ times faster. The time this algorithm takes to perform a complete 3D reconstruction in the

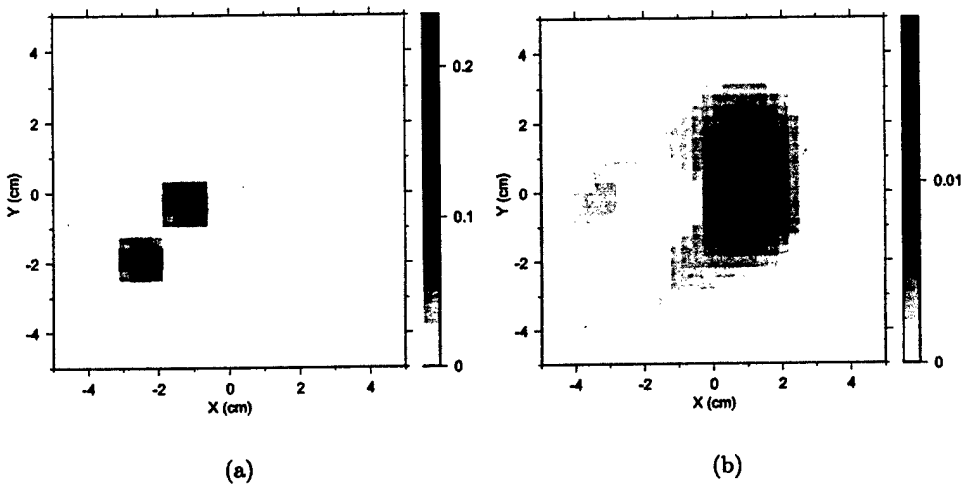

Fig. 9. Layer reconstruction at a noise level of 5%: (a) resolved objects E (left) and F (right) at $z = 0.75$ cm (layer 3); (b) resolved objects G (upper) and H (lower) at $z = 1.35$ cm (layer 5). The darkness of the pixel represents the resolved reduced scattering coefficient in units of inverse millimeters.

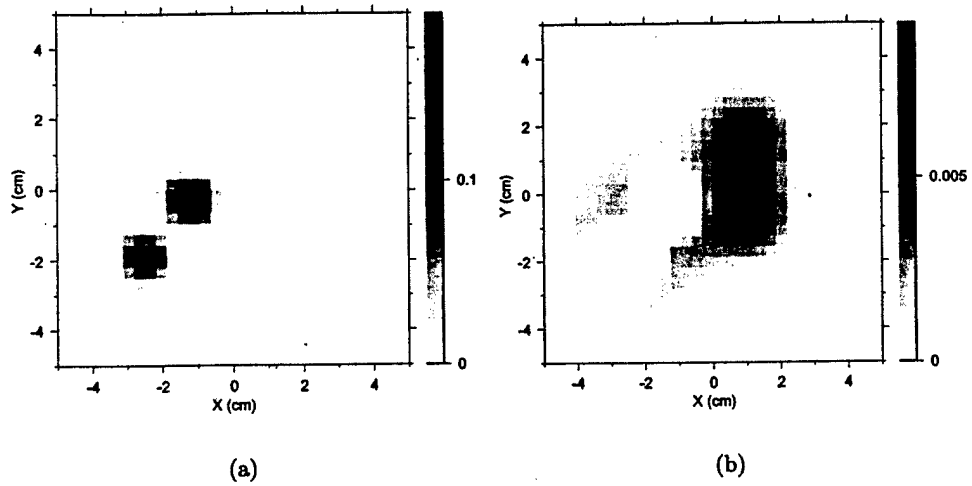

Fig. 10. Layer reconstruction at a noise level of 10%: (a) resolved objects E (left) and F (right) at $z = 0.75$ cm (layer 3); (b) resolved objects G (upper) and H (lower) at $z = 1.35$ cm (layer 5). The darkness of the pixel represents the resolved reduced scattering coefficient in units of inverse millimeters.

above examples (of $32 \times 32 \times 10$ volume elements) is less than half a minute with use of the scripting language Python on one 180-Mhz CPU of an Origin 200 computer from Silicon Graphic Inc. This algorithm scales only linearly with the number of elements in the xy grid, so it can be used to handle much larger data sets in real time with little difficulty.

This approach does not limit the number or the thickness of the inhomogeneities. It allows multiple inhomogeneities, and one inhomogeneity may span several layers.

With little effort, a depth profile (the sum of the perturbation of the optical parameter versus depth) of the inhomogeneities inside a highly scattering turbid medium can be obtained. This information itself may be very useful in some cases. When the inhomogeneity is found to exist only in one layer from the depth profile, the summation in Eq. (14) no longer exists. A direct inverse Fourier transform can thus be used to resolve the inhomogeneity when it is a solely absorptive or scattering perturbation.

APPENDIX A

Equation (12) is the exact formula for calculating the scattered wave field. For a pulse $S(\mathbf{r}, t) = S(\rho)\delta(z - z_s)\delta(t)$ with Gaussian shape $S(\rho) = S_0 \exp(-\rho^2/2\sigma^2)$, we have $\hat{S}(\mathbf{q}) = 2\pi\sigma^2 S_0 \times \exp(-\sigma^2 q^2/2)$ and the first term of Eq. (12),

$$
\begin{aligned}
A &= -\frac{\sigma^2 S_0 c}{2\pi} \int \mathrm{d}^2\mathbf{q}'\mathrm{d}z'\,\delta\hat{\mu}_a(\mathbf{q} - \mathbf{q}', z') \\
&\quad \times \exp(-\sigma^2 q'^2/2) w_a(\mathbf{q}, \mathbf{q}', z, t; z') \\
&= -\frac{\sigma^2 S_0 c}{2\pi} \int \mathrm{d}^2\mathbf{q}'\mathrm{d}z'\mathrm{d}^2\rho'\,\delta\mu_a(\rho', z') \\
&\quad \times \exp[-i(\mathbf{q} - \mathbf{q}') \cdot \rho' - \sigma^2 q'^2/2] \\
&\quad \times w_a(\mathbf{q}, \mathbf{q}', z, t; z') \\
&= -\frac{\sigma^2 S_0 c}{2\pi} \int \mathrm{d}^2\rho'\mathrm{d}z'\,\delta\mu_a(\rho', z')\exp(-i\mathbf{q} \cdot \rho') \\
&\quad \times \int_0^t \mathrm{d}t'\hat{G}(\mathbf{q}, z, z', t - t') \\
&\quad \times G_z(z', z_s, t')\exp(-\mu_a c t') \\
&\quad \times \int \mathrm{d}^2\mathbf{q}' \exp(-\sigma^2 q'^2/2 - Dct' + i\mathbf{q}' \cdot \rho')
\end{aligned}
\tag{16}
$$

after plugging in Eq. (11) and Eq. (6).

The last integral of Eq. (16) can be performed exactly and turns out to be $\pi R^{-2}\exp(-4\rho'^2/R^2)$, where the effective width $R^2 = \sigma^2/2 + Dct' > \sigma^2/2$. When the inhomogeneities exist inside a region of radial dimension L around the origin of the xy coordinate system that satisfies $L \ll R$, we can approximate $\exp(-4\rho'^2/R^2)$ by 1, which is equivalent to letting $\mathbf{q}' \to 0$, the case of an incident plane wave. The error made by such an approximation is of second order in L/R.

The same analysis can be applied to the second term of Eq. (12).

ACKNOWLEDGMENTS

We thank W. Cai and S. Gayen for useful discussions and comments on this work. We also acknowledge the U.S. Department of Energy and the U.S. Army Medical Research and Materiel Command for support of this work.

Corresponding author Min Xu can be reached by e-mail at minxu@sci.ccny.cuny.edu.

REFERENCES

1. B. Chance and R. R. Alfano, eds., *Optical Tomography, Photon Migration, and Spectroscopy of Tissue and Model Media: Theory, Human Studies, and Instrumentation*, Proc. SPIE **2389** (1995).
2. R. R. Alfano, S. G. Demos, and S. K. Gayen, "Advances in optical imaging of biomedical media," Ann. N.Y. Acad. Sci. **820**, 248–271 (1997).
3. J. C. Hebden, S. R. Arridge, and D. T. Delpy, "Optical imaging in medicine: I. Experimental techniques," Phys. Med. Biol. **42**, 825–840 (1997).
4. S. R. Arridge and J. C. Hebden, "Optical imaging in medicine: II. Modelling and reconstruction," Phys. Med. Biol. **42**, 841–853 (1997).
5. W. Cai, B. B. Das, F. Liu, M. Zevallos, M. Lax, and R. R. Alfano, "Time-resolved optical diffusion tomographic image reconstruction in highly scattering turbid media," Proc. Natl. Acad. Sci. U.S.A. **93**, 13561–13564 (1996).
6. X. D. Li, T. Durduran, and A. G. Yodh, "Diffraction tomography for biomedical imaging with diffuse-photon density waves," Opt. Lett. **22**, 573–575 (1997).
7. X. Cheng and D. A. Boas, "Diffuse optical reflection tomography with continuous-wave illumination," Opt. Express **4**, 118–123 (1998), http://www.opticsexpress.org.
8. W. Cai, S. K. Gayen, M. Xu, M. Zevallos, M. Alrubaiee, M. Lax, and R. R. Alfano, "Optical tomographic image reconstruction from ultrafast time-sliced transmission measurements," Appl. Opt. **38**, 1–10 (1999).
9. T. Durduran, J. P. Culver, M. J. Holboke, X. D. Li, and L. Zubkov, "Algorithms for 3D localization and imaging using near-field diffraction tomography with diffuse light," Opt. Express **4**, 247–262 (1999), http://www.opticsexpress.org.
10. S. R. Arridge, "Photon-measurement density functions. Part I. Analytic forms," Appl. Opt. **34**, 7395–7409 (1995).
11. P. C. Hansen, "Analysis of discrete ill-posed problems by means of the L-curve," SIAM Rev. **34**, 561–580 (1992).
12. P. C. Hansen and D. P. O'Leary, "The use of the L-curve in the regularization of discrete ill-posed problems," SIAM J. Sci. Comput. **14**, 1487–1053 (1993).